Late Quaternary Extension Rates Across the Northern Half of the Yadong-Gulu Rift: Implication for East-West Extension in Southern Tibet

M.-l. Chevalier, P. Tapponnier, Jérôme van Der Woerd, Philippe Hervé Leloup, S. Wang, J. Pan, M. Bai, E. Kali, X. Liu, H. Li

Late Quaternary Extension Rates Across the Northern Half of the Yadong-Gulu Rift – Implication for East-West Extension in Southern Tibet

M.-L. Chevalier[1], P. Tapponnier[2], J. van der Woerd[3], P. H. Leloup[4] , S. Wang[1], J. Pan[1], M. Bai[1], E. Kali[3], X. Liu[5] and H. Li[1]

[1] Key Laboratory of Deep-Earth Dynamics of Ministry of Natural Resources, Institute of Geology, Chinese Academy of Geological Sciences, 26 Baiwanzhuang Rd, Beijing 100037, People's Republic of China

[2] Institute of Crustal Dynamics, China Earthquake Administration, Beijing, People's Republic of China

[3] Institut de Physique du Globe de Strasbourg, UMR 7516 CNRS, Universite de Strasbourg, 5 rue René Descartes, 67084 Strasbourg cedex, France

[4] Laboratoire de géologie de Lyon, CNRS UMR 5570, Université de Lyon, Villeurbanne, France

[5] Institute of Tibetan Plateau Research, Chinese Academy of Sciences, Beijing, China

Corresponding author: Marie-Luce Chevalier (mlchevalier@hotmail.com)

Key points:

- Extension rates along Yadong-Gulu rift decrease from north (3-6 mm/yr) to south (~1.3 mm/yr) due to Beng Co dextral faulting
- The post-250 ka extension rate across the ~1000 km stretch of S Tibet north of Nepal is 9±2 mm/yr, consistent with geodetic rates
- The causes and mechanisms of eastward extension south and north of the Bangong-Nujiang suture

25 are different

Abstract

The presence of ~NS-trending rifts within the Tibetan Plateau attests that it is undergoing ~EW extension. In southern Tibet, the total extension rate, distributed across seven main rifts over a distance of ~1000 km, has been inferred to amount to about half of the shortening rate across the Himalayas. Quantifying the late Quaternary extension rates across the largest rift (Yadong-Gulu rift: YGR) is important to understand Tibetan deformation and to discuss the high plateau evolution during the later stages of continental collision. We performed ^{10}Be surface-exposure cosmogenic nuclide dating of 57 samples from three fluvial surfaces and two moraines that are vertically offset by the normal faults bounding the northern YGR. After carefully assessing individual ages at each site, to elucidate scatter in the age distributions, we obtained ~EW extension rates of up to 3-6 mm/yr near the northern end of the rift (Gulu) and of only 1.3±0.3 mm/yr in the south (Yangbajing). The fast rates in the north may be influenced by dextral slip along the Beng Co fault, whose rate ought to be at least 6.0±1.8 mm/yr. The total late Quaternary extension rate of 9±2 mm/yr we infer across southern Tibet between ~81 and 92°E, assuming similar rates across each rift, is similar to earlier, qualitative inferences, and consistent with recent geodetic results. Distinct deformation rates north and south of the Bangong-Nujiang suture may reflect significant differences between the extensional kinematics and mechanisms across the Qiangtang and Lhasa blocks.

1 Introduction

Several deformation mechanisms have been co-involved in accommodating the ongoing convergence of India into Asia: large-scale thrusting along the Himalayas, strike-slip faulting along the edges of, and within the Tibetan Plateau, additional thrusting and crustal thickening yet farther north (Tian Shan, Altai), large and small scale block rotation, and, as long recognized, ~EW extension across much of the Tibetan Plateau (e.g., Molnar & Tapponnier, 1978; Armijo et al.,

1986; Tapponnier et al., 1986; Avouac & Tapponnier, 1993; Avouac et al., 1993; Peltzer & Saucier, 1996). However, how much of the >2000 km (e.g., Achache et al., 1984; Patriat & Achache, 1984) of northward penetration of India into Asia has been accommodated by each of these different processes is still debated. Here we try to better quantify the recent ~EW extension observed across the series of prominent ~NS-trending rifts that cut the southern plateau south of the Bangong-Nujiang suture (BNS). Due to remoteness at high elevation and lack of infrastructures, field investigations of the late Quaternary deformation in central Tibet have been few and far apart (e.g., Armijo et al., 1986, 1989; Yin et al., 1999; Blisniuk et al., 2001; Taylor et al., 2003; Ratschbacher et al., 2011; Han et al., 2019; Li et al., 2018). While pioneering studies using satellite imagery and fault plane solutions helped clarify Tibetan faulting patterns on a broad scale (e.g., Molnar & Tapponnier, 1978; Ni & York, 1978; Tapponnier et al., 1981; Molnar & Lyon-Caen, 1989), attempts to quantitatively determine late Quaternary rates along the numerous active normal faults still remain punctual (Blisniuk & Sharp, 2003; Wu et al., 2004, 2015; Kali, 2010; Chevalier et al., 2012; Ha et al., 2019; Li et al., 2019; Wang et al., 2020).

Early on, Baranowski et al. (1984) and Armijo et al. (1986, 1989) proposed that the dominant ~EW extension along normal faults bounding ~NS-trending rifts across southern Tibet was primarily related to divergent, orthogonal thrusting along the curved Himalayan main frontal thrust (MFT), and to the fact that several such rifts branch southwards off active right-lateral strike-slip faults (Figure 1a). These NW-striking, right-lateral strike-slip faults form a dextral, en-echelon array (the Karakorum-Jiali Fault Zone: KJFZ) located along and just south of the BNS, where they all stop. Father north, less prominent, shorter normal faults appear to reflect more widely distributed stretching (e.g., Molnar & Tapponnier, 1978; Taylor et al., 2003). This suggests that the mechanisms of crustal extension in southernmost Tibet are different from those in west-central Tibet (e.g., Tapponnier et al., 1986). The ~400 km wide and ~1500–1800 km long zone of central

Tibet centered along the BNS has also been interpreted to accommodate coeval EW extension and NS contraction (on order of 10-30 km, hence a small fraction of Indo-Asian convergence) across a series of "conjugate" strike-slip faults with opposite senses (e.g., Wang et al., 2001; Taylor et al., 2003; Yin & Taylor, 2011). At the whole Plateau scale, the largest "conjugate" strike-slip fault system is that of the Altyn Tagh and Karakorum faults (Figure 1a, inset). The two easternmost, ~200-300 km-long faults south of the BNS (Gyaring Co [GCF], Beng Co [BCF] faults, Figure 1a) are the longest of the left-stepping, en-echelon faults within the Karakorum-Jiali fault zone (Armijo et al., 1986). The left-stepping, right-lateral faulting along the KJFZ/BNS shear zone has been suggested to link the Karakorum fault to the west to the Red River and Sagaing faults to the SE (Tapponnier et al., 1986), and to facilitate the eastward extrusion of central Tibet's Qiangtang block (Armijo et al., 1989) (Figure 1a). The Triassic, lithospheric BNS would thus have guided the activation of a younger, neotectonic strike-slip shear zone (Armijo et al., 1986, 1989).

Even though most of the south Tibetan rifts cross the Yarlung Zangbo River and suture (YZS) (as attested for instance by knickpoints where the river crosses the Tangra Yum Co, Yadong-Gulu and Cona-Oiga rifts, Figure 1a, Y. Wang et al., 2019), they are morphologically different to the north and south. To the south, they tend to be less developed, with single, en-echelon master faults in most places (Figure 1a). By contrast, between the YZS and the BNS, the rifts include, or are bounded by, conjugate master faults with larger cumulative throws (e.g., Armijo et al., 1986). This difference north and south of the YZS has been inferred to be related to the presence of strong and cold Indian lithosphere plunging beneath the Tethyan Himalayas. India, however, might not extend far north of the YZS (e.g., Roger et al, 2000; Tapponnier et al., 2001; Liu-Zeng et al., 2008) as sometimes advocated (e.g., Owens & Zandt, 1997; Tilmann et al., 2003; Copley, 2011).

The presence of normal faulting and EW extension in Tibet have long been correlated with the particularly high elevation of the plateau (e.g., Molnar & Tapponnier, 1978), which may have

been attained before the Oligocene in south central Tibet (e.g., Tapponnier et al., 2001; Rowley & Curie, 2006; DeCelles et al., 2007; Liu-Zeng et al., 2008), and in the middle Miocene in southernmost Tibet (Tethys Himalayas) (e.g., Spicer et al., 2003; Currie et al., 2005; Liu-Zeng et al., 2008; Ding et al., 2017). Divergent orthogonal thrusting (with little or no oblique component) along the curved MFT adequately predicts the average ~N100°E extension direction across southern Tibet (e.g., Baranowski et al., 1984; Armijo et al., 1986, Tapponnier et al., 1986), which is essentially perpendicular to the ~N6-10°-trending axis of symmetry of the rifts, located between 85 and 88°E (e.g., Tapponnier et al, 1981; Armijo et al., 1986; Molnar & Lyon Caen, 1989; Kapp & Guynn, 2004). Strain partitioning due to oblique convergence between India and Asia, based on Nuvel-1A plate velocities, has also been invoked to account for southern Tibet extension (e.g., Molnar & Lyon-Caen, 1989; McCaffrey & Nabelek, 1998; Kapp et al., 2008; Styron et al., 2011; Murphy et al., 2014). Finally, other models argue for convective removal of the Tibetan mantle lithosphere and, following plateau uplift, gravitational collapse and spreading due to maximum sustainable elevation (e.g., England & Houseman, 1989; Elliott et al., 2010), lithospheric delamination (e.g., Harrison et al., 1992), or even rollback of the east Pacific subduction margin (Yin, 2000).

Constraining the onset and rates of normal faulting along the Tibetan rifts is essential to better understand how Tibet (and other continental plateaus) formed and evolved, as the age of rift initiation may mark a change from compressional thickening to extensional thinning of the crust. The onset of normal faulting may be thought to reflect the time when the Tibetan Plateau was uplifted to its maximum elevation (e.g., Armijo et al., 1986; Garzione et al., 2000). It was initially suggested that rifting, at least in southern Tibet, was very young, starting around 2.0±0.5 Ma, based on the stratigraphic age of late Pliocene/early Quaternary deposits in ~EW-trending basins north of the Himalayan Range (Armijo et al., 1986). Later chronological studies, however, suggested

significantly older ages for the onset of extension (up to ~10-14 Ma) with a rate acceleration in the late Miocene to early Pliocene (4-5 to 8 Ma) (e.g., Mahéo et al., 2007; Lee et al., 2011; Sundell et al., 2013; Styron et al., 2013, 2015). North of the BNS, along the Shuanghu graben, Yin et al. (1999) also inferred an onset age of extension of <4 Ma (Figure 1a), later re-assessed to have been much older (13.5 Ma, Blisniuk et al., 2001).

In the south, between the Himalayas and the KJFZ/BNS, southern Tibet is characterized by seven long, ~NS-trending active rifts (e.g., Molnar & Tapponnier, 1978; Molnar & Chen, 1983; Armijo et al., 1986; Molnar & Lyon-Caen, 1989) that are roughly equally spaced, from ~200 km in the east to ~150 km in the west. North of the BNS, the more numerous, smaller grabens lie only ~100 km apart (Armijo et al., 1986). The apparent decrease in rift spacing across the BNS has been suggested to reflect the different mechanical properties of the Lhasa and Qiangtang blocks, a consequence of the different geological histories, thicknesses and ages of their crust (e.g., Hirn et al., 1984; Yin, 2000), which has been shown to vary significantly in different parts of the Tibetan Plateau (e.g., Vergne et al., 2002; Wittlinger et al., 2004). Three of the southern rifts (Thakkhola, Dinggye/Ama Drime and YGR, Figure 1a) radically cross the Himalayan Range. The direction of extension along most rifts and their bounding normal faults (N96°E±7° on average, N102°E for the YGR) is perpendicular to the average trend of the rifts N5.9±7.5°E (Armijo et al., 1986). The longest rift, which is the subject of our study here, the YGR, stretches ~500 km from the India-Bhutan border to the BNS north of Gulu, south of Nagqu (Figure 1a).

In this paper, using ^{10}Be surface-exposure cosmogenic isotope dating of vertically offset geomorphic surfaces (two moraines and three alluvial fans and terraces) at five locations along the northern half of the YGR, between the YZS and BNS, we significantly augment the handful of quantitative late Quaternary throw rates that exist in both southern Tibet (three rifts: YGR: Wu et al., 2004; Ha et al., 2019; Wang et al., 2020; Dinggye/Ama Drime rift: Kali, 2010; Gurla

Mandhata/Pulan rift: Chevalier et al., 2012) and northern Tibet (two rifts: Shuanghu: Blisniuk & Sharp, 2003; Dong Co: Li et al., 2019). Our data support what Armijo et al. (1986) inferred on a broad scale, i.e., an extension rate of 1.3±0.3 mm/yr along the YGR, consistent with a total of ~9±2 mm/yr across all seven south Tibetan rifts assuming similar rates across each. This rate is comparable to that predicted by divergent thrusting along the Himalayan arc (Baranowski et al., 1984; Armijo et al., 1986). At a more detailed level, rifting along the Gulu half-graben, northernmost segment of the YGR, may be significantly faster, which may result from interaction with the dextral Beng Co strike-slip fault, part of the KJFZ.

2 Geological setting of the Yadong-Gulu rift

Due to its exceptional length (~500 km) and easy access from Lhasa (Figure 1), the N10°-35°E-trending Yadong-Gulu rift (YGR), largest of the south Tibetan grabens has been the focus of significant research (e.g., Armijo et al., 1986, 1989; Harrison et al., 1995; Wu et al., 2004). It is one of the few rifts that cuts across the Himalayan Range, historically allowing trade with India. Between the China-India (Sikkim) border in the south and Nagqu in the north, the rift crosses major geological structures including the south Tibetan detachment system (STDS, e.g., Burchfiel et al., 1992; Leloup et al., 2010), the Yarlung Zangbo suture (YZS) and river, and terminates just south of the Bangong-Nujiang suture (BNS). From north to south, it can be divided into four parts: 1) the Gulu half-graben, 2) the Damxung corridor north of Yangbajing (Figure 2a), 3) the Yangbajing and Angang grabens between the Nyainqentanghla (NQTL) Range and the Yarlung Zangbo River (Figure 3), and 4) the Yadong grabens south of the Yarlung Zangbo River (Armijo et al., 1986).

Roughly 100 km NW of Lhasa, the NQTL, at 7162 m one of the highest mountain ranges inside the Tibetan Plateau, extends for about 200 km in an oblique, northeastern direction (Figure 1b). It follows the west side of the northern YGR, which is bounded by NE to EW-striking normal

and left-lateral strike-slip faults (Figure 2). While all other active rifts in southern Tibet trend ~NS and are bounded by predominantly normal faults (e.g., Armijo et al., 1986), the co-existence of active normal and sinistral strike-slip kinematics is unique to the YGR, and is most likely related to inheritance from older, Tertiary tectonic features that now guide the peculiar, oblique, en-echelon geometry of the normal faults (Tapponnier et al., 1981, 1986). Along most of the eastern side of the NQTL Range, slip at the surface is partitioned between two roughly parallel strands having distinct components of motion (strike-slip *vs* normal), implying shallow bifurcation of oblique slip on the master fault at depth (Armijo et al., 1986).

2.1 Northern Yadong-Gulu rift: the Damxung corridor - Gulu half-graben

The northern part of the YGR includes the Damxung corridor and the Gulu half-graben (Figure 2). The ~120 km-long Damxung corridor follows the NE-striking normal-sinistral fault system along the base of the SE slope of the NQTL Range. Numerous Quaternary scarps trending N12°E±7° form a left-lateral array of east-dipping faults while a few west-dipping faults control the formation of pull-aparts and sag ponds (Armijo et al., 1986). At the Gulu bend, between the Damxung corridor and the Gulu half-graben, the active faults veer ~90° from an ~EW to a ~NS direction, in an abrupt transition from dominant left-slip to dominant normal throw (Figure 2a). The western side of the Gulu half-graben is bounded by an east-dipping active normal fault with particularly sharp, steep and high scarps at the base of deeply eroded and gently sloping triangular facets (Figure S1). In most places, the rupture of the 1952, Mw7.4 Gulu earthquake is strikingly clear, with a continuous free-face, up to ~1.5 m-high between the footwall and hanging wall (Tapponnier et al., 1981; Armijo et al., 1986). The normal faults along the northern end of the YGR then connect with the ~NW-striking, dextral, Beng Co fault rupture (1951 Mw7.7 earthquake, average 8±2 m right-lateral coseismic displacement and 90 km-long surface break, Armijo et al.,

194 1989) (Figures 1b and 2).

195

196 2.2 Central Yadong-Gulu rift: the Angang and Yangbajing grabens

197 The central part of the YGR is composed of two major NS-trending grabens (Figure 3). To
198 the south, the Angang graben is bounded on its western side by an east-dipping master fault that
199 cuts and offsets a large Quaternary landslide, and along which slickensides attest to normal-sinistral
200 motion (Armijo et al., 1986). The fault bounding the eastern side of the graben is morphologically
201 less prominent, but its stepping segments offset early Holocene terraces (section 5.2, page 19 in
202 Armijo et al., 1986). To the north, the Yangbajing graben, broadest extensional basin along the
203 entire YGR, is filled with up to 1000 m of Quaternary sediments (Cogan et al., 1998). It is limited
204 to the east and west by normal faults dipping steeply in opposite directions (Figure 3). As clearly
205 visible on satellite imagery and in the field, the main, east-dipping normal fault (to the west)
206 exhibits fresh scarps along much of the range-front. Such scarps, along which there are hot springs,
207 follow the base of ~500 m-high triangular facets between hanging glacial valleys (Figure 3)
208 (Armijo et al., 1986; Mercier et al., 1987). An array of closely spaced, sub-parallel, west-dipping
209 normal faults follows the central part of the graben, in rough alignment with both the Damxung
210 corridor to the north and the Angang graben to the south (Armijo et al., 1986; Kapp et al., 2005).
211 Such faults appear to absorb much of the late Quaternary extension. The west-facing normal
212 escarpments closest to the graben floor are smaller and steeper than those located farther eastwards,
213 which are higher and more eroded, hence likely older. That fault system ruptured during the
214 destructive (due to poorly built adobe houses) 2008 Mw6.3 “Damxung” earthquake, whose
215 hypocenter was 8-12 km deep, on a 47°-53° west-dipping focal plane (Elliott et al., 2010). At the
216 surface, this event reportedly generated only small landslides and a few cracks (Wu et al., 2011).
217 Towards the north, the dense normal fault array appears to be transversally cut by a sinistral, ENE-

striking fault that also offsets, by ~4 km, the main, western, range-front fault (Armijo et al., 1986) (Figure 3).

3 Methods

To quantitatively determine late Quaternary throw rates along the Yadong-Gulu rift (YGR), we mapped active fault strands and geomorphic surfaces such as alluvial fans, river terraces and glacial moraines, using a combination of field work, high-resolution satellite images, unmanned aerial vehicle (UAV aka drones), as well as high-resolution topographic data from a Riegl VZ1000 terrestrial LiDAR (Light Detection and Ranging) scanner (angular resolution of 0.02° for raw data, set to <0.5 m horizontally and <0.2 m vertically between two data points after filtering). We targeted five particularly clear sites along the northern half of the YGR where active faults orthogonally cut and offset geomorphic surfaces, in order to reconstruct the space-time evolution of the faults. Some of these sites (Damxung T, Yangbajing M and Gyekar T) were initially discovered by and discussed in Armijo et al. (1986) and we conducted fieldwork for tectonic (this study) and paleoclimatic (Chevalier et al., 2011a) purposes to complement the earlier, 1986 observations. Precise vertical (and horizontal) offsets were measured from the Digital Elevation Model (DEM) created by our LiDAR surveys, and the ages of the offset surfaces were deduced from ^{10}Be and ^{26}Al cosmogenic surface-exposure dating (e.g., Lal, 1991; Gosse & Phillips, 2001). Combining the abandonment age of the surfaces with their offsets yields median throw or horizontal rates on timescales corresponding to the surface ages (calculated using Zechar & Frankel, 2009). The results are presented in Tables 1 (for moraines) and 2 (for fans/terraces).

Using hammer and chisel, we collected a total of 57 samples from the top few centimeters of large granite boulders (>1 m in diameter) on moraine crests (n=15 at Gulu M and n=22 at Ybj M) and quartzite cobbles (~20-30 cm in diameter) on alluvial fans or terraces (n=5 at Gulu T, n= 10 at

242 Damxung T and n=5 at Gyekar T). The mineral separation and quartz cleaning procedure was
243 modified from Kohl and Nishiizumi (1992). To limit the influence of processes that might have
244 affected the ^{10}Be and ^{26}Al concentration in the samples, with ages appearing younger (due to
245 rolling, erosion or shielding) or older (due to inheritance / prior exposure) than the actual surface
246 ages, we applied corrections for topographic shielding and sampled the largest possible boulders on
247 the moraines and cobbles that were well-embedded in the terrace surfaces. We did not correct for
248 snow (due the lack of regional data) or vegetation (mostly short grass) cover, and we assumed zero
249 erosion when calculating the ages due to the lack of surface incision on the flat terrace surfaces we
250 sampled.

251 The two moraines studied here (Gulu and Ybj) have been dated by Chevalier et al. (2011a)
252 for paleoclimatic purposes using ^{10}Be. We recalculated the corresponding ages using the CRONUS
253 calculator version 2.3 (Balco et al., 2008) with the time-dependent production rate model of Lal
254 (1991)/Stone (2000) for these data as well as for data from the moraines cited here (Owen et al.,
255 2005). We apply Peirce criterion to reject possible outliers then assign a class (A, B or C) according
256 to how well the ages cluster on each moraine using the reduced Chi-squared analysis (e.g., Heyman,
257 2014; Blomdin et al., 2016; Batbaatar et al., 2018; Chevalier & Replumaz, 2019). The minimum
258 moraine abandonment age is given by the average age of the samples for class A moraines and by
259 the oldest age for classes B and C moraines (Heyman, 2014; Blomdin et al., 2016).

260 The quartzite cobbles from the alluvial surfaces were analyzed by Kali (2010) using both
261 ^{10}Be and ^{26}Al cosmogenic isotopes. The ages were recalculated in a way similar to that described
262 above for the moraines. Samples with simple exposure history should have similar ^{10}Be and ^{26}Al
263 ages and a ^{26}Al/^{10}Be concentration ratio of 6.1 (Table 2). Departure from this ratio implies that the
264 samples have had a complex exposure history: analytical problems for ratios >6.1 and episode(s) of
265 shielding (burial by snow, ice, sediment, or water) and/or erosion for ratios <6.1 (Gosse and

Phillips, 2001). We applied Peirce criterion to alluvial surfaces with more than two samples (which excludes the Gyekar T1 surface) and discuss potential additional outliers following stratigraphic and other observations at each site. Due to the small number of dated samples on each terrace surface, assigning an abandonment age was not straightforward since the Be and Al ages often vary significantly, with ^{26}Al ages being systematically younger than the ^{10}Be ages (due to the shorter half-life of ^{26}Al) and since such disparity increases with age (Gosse and Phillips, 2001). Therefore, we present, discuss and interpret each site individually in the following sections.

4 Site description, results and age interpretation

4.1 Gulu moraine

The Gulu moraine site is located at the outlet of a 8 km-long, U-shaped, glacially incised valley coming from the 6532 m high Samdain Kangsang peak. The present-day glacier terminus is located ~4 km upstream from the normal faulted range-front (Figure S1). The normal fault zone crossing this moraine is marked by multiple parallel west- and east-dipping scarps (Figures 4-6 and S2), some of which freshly ruptured by the Mw7.4 1952 Gulu earthquake. That particularly wide (~400 m) extensional zone forms a smooth graben with a total, cumulative vertical throw depth of 40±4 m (Figure 6). The large number of normal fault scarps (up to ~20, Figures 4-6 and S2), including several with opposite dips, implies distributed extension at shallow depths, in keeping with the fact that most of the cumulative offsets along the faults are comparable and on order of only a few meters (Figure S2). That such active faults do not extend to great depths is clearly visible on both sides of the steep, ~100 m-deep, glacially-incised valley (Figure 4b). On either side of that valley, the normal faults that dip ~50±10° on average (Figures 5 and 6c) appear to root into a much shallower-dipping detachment, whose intersection with surface topography is visible on both the northern and southern valley flanks (black lines with white polygonal tips in Figure 4). The

measured, average dip of the detachment surface ranges between ~10° and 20° (Figure 4b), roughly parallel to the average dip of the shallow-dipping triangular facets on the bedrock footwall farther upstream in the valley (black lines with green polygonal tips in Figures 4). We thus interpret the widely distributed normal faulting to root at shallow depth on an 18±5° east-dipping detachment (green dashed lines in Figure 6c), possibly reactivating an older basement detachment fault exposed on the similarly shallow-dipping facets (Figure S1). Although we did not explore and sample that structure, it may be analogous to the shallow-dipping detachment fault studied in greater details along the southern part of the NQTL Range (e.g., Cogan et al., 1998; Kapp et al., 2005). However, because the epicentral depth of the 1952 Gulu earthquake was most likely on order of ~10-15 km, as is the case for all normal faulting earthquakes in Tibet (e.g., Elliott et al., 2010; Ryder et al., 2014), and because its fault plane and surface rupture had dips between 45-70° (Armijo et al., 1986), the shallow-dipping detachment fault cannot extend far eastwards past the range-front and must be vertically offset by the more steeply-dipping, seismic normal fault (Figure 6c).

The Gulu moraine surface is covered with short grass and large embedded boulders (Figures 5 and S3). Chevalier et al. (2011a) collected seven samples upstream (T5C-58 to 64) and eight samples downstream (T5C-66 to 73) from the fault along the southern lateral moraine crest (Figure 4b). The ^{10}Be ages range from 16.8±1.6 to 22.0±2.0 ka (Figure 7 and Table 1). That age distribution contains no outlier and the moraine is class B (moderately clustered) so that the oldest age is taken to represent the minimum moraine abandonment age. This age closely corresponds to a Last Glacial Maximum age (or Marine Isotope Stage MIS-2) (Clark et al., 2009) and is in agreement with regional studies (e.g., Dong et al., 2014, 2017, Figures 2 and 3). Hence, considering that the 40±4 m vertical offset accumulated since that deglaciation time, an average subsidence rate of 1.8±0.3 mm/yr is obtained. In view of the inferred shallow dip of the basement detachment fault (18±5°), such a vertical rate would imply an ~EW extension rate of 6.0±1.8 mm/yr.

314

315 4.2 Gulu terrace

316 The Gulu terrace site, 15 km south of the Gulu moraine site (Figure 2), is located at the
317 outlet of a <2 km-long, V-shaped valley that was only partially glaciated upstream (Figure 8).
318 Hence, no glacier crossed the normal fault in the recent past, and a sharp and steep cumulative scarp
319 vertically offsets, by 25±2 m, a large, flat, fluvial fan at the outlet of that valley (Figure 9). Medium
320 size cobbles rest on top of that fan/terrace surface, which is sparsely covered with short grass
321 (Figures 8 and S4). Just north of the fan, the multiple scarps of the 1952 surface rupture are clearly
322 visible (Figure 8). Southwards, they extend partly along the steepest, free-faced part of the
323 escarpment that limits the fan/terrace to the east. Rockfalls, likely of seismic origin, cover part of
324 the uplifted terrace surface (Figure 8e), while a small village lies on the down-faulted fan surface at
325 the base of the scarp (Figure 8a,f). In order to avoid possible mixing and contamination of fluvial
326 terrace cobbles with colluvium or rockfall debris, we sampled both surfaces as close as possible to
327 the fluvial risers (Figure 8b). We dated three samples upstream and two samples downstream from
328 the fault. The ^{10}Be age distribution from the upper surface are 3.3±0.3, 4.4±0.5 and 15.3±1.5 ka,
329 similar to the ^{26}Al age distribution (2.7±0.3, 3.2±0.6 and 12.9±1.3 ka, Figure 10 and Table 2). The
330 two samples on the lower surface yield ^{10}Be ages of 55.1±5.6 and 403.1±42.7 ka, and ^{26}Al ages of
331 43.3±4.4 and 359.7±41.2 ka. The ^{26}Al/^{10}Be concentration ratios vary from 4.5 to 5.5 (instead of the
332 ideal 6.1), implying a rather poor agreement between the Be and Al measurements, indicative of a
333 complex exposure history (see methods section).

334 While it is not trivial to reconstruct the deposition history at this site, it is clearly improbable
335 that the upper surface be younger than the lower one. It thus seems likely that the two old ages on
336 the lower surface come from flash flooding of exposed, old bedrock in the upper reaches of the
337 stream catchment (inherited samples/ages). By contrast, the uplifted terrace ages may be interpreted

to reflect abandonment at 3.4±0.7 ka (average of the four consistent Be and Al ages of the two youngest samples), assuming that the much older (~5 times) age of 15.3/12.9 ka (Be/Al) is an outlier, most likely issued from rock collapse. Using only the more consistent Be ages would yield an age of 3.9±0.8 ka. We note that such an age (~4 ka), as well as the corresponding terrace heights above the present drainage, are consistent with strong river incision following the end of the early Holocene Climatic Optimum (HCO), as frequently observed in and around the Tibetan Plateau (e.g., Gasse et al., 1991; Van der Woerd et al., 2002; Mériaux et al., 2005; Li et al., 2005; Chevalier et al., 2011b, 2012). Combining the 25±2 m vertical offset with the 3.9±0.8 ka age yields a particularly fast throw rate of 6.4(+1.7/-1.1) mm/yr, in tune with the steep, partly free-faced (60-70°), normal fault scarp that bounds the uplifted terrace to the east (Figures 8f and 9c). Given that steep dip, the rate of horizontal extension at this Gulu terrace site would be 3.1±0.6 mm/yr. The significant difference with the Gulu moraine site rate, located only 15 km northwards, would largely be due to the contrasting influence of older tectonic structures. Similar along-strike transitions from high to low-angle normal faulting has been documented elsewhere in Tibet, notably along the Lunggar rift normal faults, to the west (e.g., Kapp et al., 2008; Styron et al., 2013). Here, the difference may be simply interpreted to imply that the deep Gulu master normal fault has breached across the shallow east-dipping detachment and reached the surface.

4.3 Damxung Terraces

Farther south near Damxung, in the mid-Damxung corridor, near the gateway of the road to Lake Nam Co, alluvial terraces are offset both horizontally and vertically by combined sinistral and normal faulting. That location was first discovered and described by Armijo et al. (1986; site 18) (Figures 1b, 2, 11 and 12). At this Damxung Terraces site, an active normal fault branch bounds the NQTL range-front (Figure 11b) while the main fault located farther to the SE splits into two strands

362 that vertically offset two large fluvial terrace surfaces by 10±2 m (T1) and 184±3 m (T2/T1 riser)
363 (Figures 13 and S5), amounts roughly comparable to those (6-8 m and ~200 m, respectively)
364 proposed by Armijo et al. (1986). On T1, the scarp height along the oblique, strike-slip/normal fault
365 F2 is larger (7±1 m) than that (3±1 m) on the mostly normal fault F1 upstream (Figures 12 and 13).
366 Along the downstream strand F2 on T1, a ~5 m-deep, ~270 m-long asymmetric pull-apart basin has
367 formed, a result of perhaps multiple paleo-earthquakes (Figure 12c,d). Similar pull-aparts, some of
368 them larger, exist along both F1 and F2 farther SW (Figure 11b), attesting to left-lateral strike-slip
369 components of motion, in addition to normal faulting. The fact that F1's dip shifts from southward
370 to northward across the western pull-apart over a distance of only a few hundreds of meters
371 confirms its predominantly sub-vertical strike-slip kinematics (Figure 11b), as befits its orientation
372 parallel to all the ENE to EW-striking faults along the Damxung corridor (Figure 2). Finally, the
373 SW edge of T1 is horizontally offset ~17±5 m by F2 (Figures 2e and 11d).

374 Six embedded cobbles were collected on the surface of T1, which is partly covered with
375 short grass (Figures 11b, 12 and S6). The corresponding ^{10}Be ages cluster well, ranging from
376 17.8±1.9 to 21.0±2.1 ka, with an average of 18.4±1.4 ka. The ^{26}Al ages are in excellent agreement,
377 ranging from 16.6±1.7 to 20.8±2.0 ka (Figure 10 and Table 2), with an identical average age of
378 18.4±1.4 ka, which we interpret to fix precisely the abandonment age of T1. This age correlates
379 well with the end of the Last Glacial Maximum, in agreement with warming climate and increased
380 alluvial deposition due to glacial melting. Two of the four samples on the upper T2 terrace yield
381 two ages (^{10}Be ages: 4.4±0.5 and 16.7±1.7 ka; ^{26}Al ages: 4.1±0.4 and 7.1±1.9 ka, Figure 10 and
382 Table 2) that are younger than those on T1, and that can therefore be discarded as outliers,
383 inconsistent with local morphology and stratigraphy. The two other samples have much older ^{10}Be
384 ages of 250.2±26.6 and 325.2±35.2 ka and ^{26}Al ages of 198.8±20.6 and 283.5±30.7 ka. Although
385 the age scatter is large, the ^{26}Al/^{10}Be concentration ratios (5.1-5.5) are reasonable. Hence, we take

386 the average $^{10}Be + ^{26}Al$ age of these two samples (264.4±53.5 ka) to represent the abandonment age
387 of T2. That terrace may have been abandoned during interglacial stages M7 or M9 (Figure 10).
388 Since the 10±2 m total vertical offset of T1 across F1 and F2 could only have started to
389 accumulate after T1 was abandoned at 18.4±1.4 ka, the corresponding throw rate across both faults
390 is 0.5±0.1 mm/yr. Combining the 184±3 m vertical offset of the T2/T1 riser with the age difference
391 (~246 ka) between the two yields a minimum throw rate of >0.75±0.2 mm/yr. A similar rate (~0.76
392 mm/yr) is obtained using the age of T2 and its height above the river. Note that combining the
393 T2/T1 riser offset with the age of T1 would yield an implausibly fast maximum throw rate of ~10
394 mm/yr. The left-lateral slip-rate along F2, deduced from the 17±5 m horizontal offset and the age of
395 T1, is 0.9±0.3 mm/yr. The normal throw rates near Damxung (~0.5 to 0.75 mm/yr) are significantly
396 slower than those found to the north, near Gulu (~1.8 and 6.4 mm/yr). This, however, may be
397 largely due to the fact that slip here is partitioned between normal and sinistral faulting. Using a
398 fault dip of 70° (Armijo et al., 1986) with a rake of 22° on F2 (Figure S7), and adding both the F1
399 and F2 throw rates (4.5 and 6.5 m in 18.4 ka = 0.24 and 0.35 mm/yr, respectively) to the F2 sinistral
400 rate (0.9 mm/yr) yields a combined extension rate of <1.6 mm/yr in the N80°E direction (Figure
401 S7). Note also that movement on the range-front fault (Figure 11b), which appears to still be active,
402 would further increase the total extension rate.
403
404 4.4 Yangbajing (Ybj) moraines
405 The Ybj moraines (site 12 in Armijo et al., 1986) are located at the outlet of a small hanging
406 glacial valley along the west side of the Yangbajing graben, whose spectacularly normal faulted
407 edge is bounded by prominent triangular facets (Figures 1, 3, and 14). The glacial valley is about 5
408 km-long, and the modern glacial terminus is located about 3 km west of the fault. Along the normal
409 fault, the lateral moraines are cut by a fresh, 5-6 m-high scarp (37° slope, Figure 14e,g) that may

have been the result of a single large earthquake that produced a continuous surface rupture of at least ~10 km-long (Armijo et al., 1986). That earthquake might have been temporarily related to the great M8.0 (?), 1411 Damxung earthquake surface break (Figure 1b), whose surface rupture has been interpreted to extend fart northwards along much of the Damxung corridor, over a total length of ~136 km (Wu et al., 1992). On both sides of the glacial valley, the lateral moraine surfaces are covered with short grass and with large, embedded granite boulders (Figure S8). Our LiDAR measurements show that the normal fault sharply cuts and vertically offsets the moraines by 44±1 m (Figure 15), a value much less than that of the cumulative offset of the valley floor (≥150 m) estimated by Armijo et al. (1986).

Chevalier et al. (2011a) collected 10 samples on both the upstream (T5C-25 to 34) and downstream (T5C-35 to 44) crests of the southern moraine, and two samples on the upstream northern moraine crest (T5C-44bis and 45) (Figure 14b). These sample ages range from 18.8±1.8 to 56.1±5.4 ka (Figure 7 and Table 1). That age distribution contains no outliers and the moraine is class C (poorly-clustered). Such a scattered but continuous age distribution is typical of moraines older than the Last Glacial Maximum (LGM ~20 ka), due to progressive exhumation of buried boulders by erosion of the moraine matrix, which yields ages younger than the actual moraine age (Chevalier & Replumaz, 2019). Thus, the oldest age suggests a Marine Isotope Stage MIS-3 age for the moraine abandonment, in agreement with the age of other outer moraines from southern and western Tibet (e.g., Chevalier et al., 2011a). Chevalier et al. (2011a) also collected five samples (T5C-19 to 23) on an inner moraine crest located upstream from the fault (Figure 14b) whose recalculated oldest age after rejecting one outlier (22.3±2.1 ka) using Peirce criteria is 15.8±1.5 ka (n=4, 12-15.8 ka, Table 1). However, this rejection of the oldest outlier would mean an absence of LGM moraine in this valley while it is clearly present at Gulu and elsewhere along the NQTL Range (Dong et al., 2014, 2017, Figures 2 and 3) and must therefore be taken with caution. In any

434 case, a LGM (or younger) age is in agreement with that crest's position within the outer MIS-3
435 moraine. Combining the 44±1 m vertical offset with the outer moraine's oldest age yields a vertical
436 throw rate of 0.8±0.1 mm/yr. Given the steepest dip of the normal fault escarpment (~41 °, Figure
437 15b), this would be consistent with a maximum extension rate of 0.9±0.1 mm/yr.
438
439 ### 4.5 Gyekar site
440 On the SE side of the Yangbajing graben, alluvial fans and terraces at the Gyekar site (site
441 11 in Armijo et al., 1986) are vertically offset by numerous N12°±16°E-trending, west-dipping
442 normal faults, resulting in a peculiar staircase morphology (Figures 1, 3, 16 and 17). These terraces
443 and faults are transversally cut by partly glacier-fed rivers, with incision deep enough to expose
444 normal fault planes with slickensides in cross-sections (Tapponnier et al., 1981). In contrast with
445 drainage in the northern Yangbajing basin, all the rivers flowing into the southern part of the basin
446 feed a central endoreic marshy wetland (Figure 3). Numerous small gullies, incising deeper across
447 the higher fault scarps, sometimes reach the terrace surfaces (Figure 17b,d). These surfaces are
448 covered with short grass and medium-size cobbles (Figures 17 and S9). The T1/T0 escarpment
449 attests to a cumulative vertical offset of 15±3 m by normal fault F1, while that of T2/T1, due to
450 movement on F2, is as much as ~6 times larger (87±5 m) (Figure 18b).
451 We dated two samples on T1 and four on T2 (Figure 16b). The two cobbles on T1 yield ^{10}Be
452 ages of 68.1±6.8 and 178.0±18.5 ka and ^{26}Al ages of 64.3±6.9 and 154.8±16.6 ka (Figure 10 and
453 Table 2), that are unfortunately insufficient to ascertain a precise abandonment age. The four
454 cobbles on T2 yield three similar ^{10}Be ages (218, 252 and 277 ka) and two similar ^{26}Al ages (193
455 and 196 ka), an average of 227.2±36.4 ka, with the remaining three ages being much younger (98,
456 39 and 14 ka) (Figure 10 and Table 2). We interpret the much younger ages as outliers since T2,
457 which is uplifted six times higher than T1, must necessarily be much older. For the same reason, the

458 younger, ^{10}Be and ^{26}Al ages on T1 (68 and 64 ka, average of 66.2±2.7 ka) may be taken to represent
459 the most plausible abandonment age of T1. Within uncertainties, such ages (~66 and 227 ka) are
460 consistent with interstadials (MIS-4 and 7) during which a warmer, wetter climate would have
461 favored river incision whereas by contrast, colder and drier glacial periods limit river flow and thus
462 restrict incision and terrace abandonment.

463 Combining the 15±3 m vertical offset of T1 with its inferred abandonment age (66.2±2.7 ka)
464 would yield a vertical throw rate of ~0.2±0.1 mm/yr on F1. Similarly, combining the 102±5 m total
465 vertical offset of T2 with its abandonment age (227.2±36.4 ka) would yield a throw rate of 0.4±0.1
466 mm/yr on F2. The cumulative throw rate on both active normal faults would thus be on order of
467 0.6±0.2 mm/yr, which might still be a minimum since there are numerous other small, likely active
468 fault strands east and west of the Gyekar site along the east side of the southern Yangbajing basin.
469 Note, however, that older faults (away from the basin) might tend to become inactive as younger
470 ones (towards the basin) develop (e.g., Sanchez et al., 2010), which would make the contribution of
471 T1 and T2 to regional extension the dominant ones.

472 We did not collect quantitative data along the active, east-dipping normal fault that bounds
473 the western side of the southern Yangbajing graben, along which hot springs are aligned at the base
474 of large triangular facets (Figures 3 and 17c,i). However, we infer that its throw rate may be similar
475 to that on the Ybj moraine fault (0.8±0.1 mm/yr) along the west side of the northern Yangbajing
476 graben, consistent with the similar height (~1600 m) of the mountain range it bounds above the
477 graben floor. The 55±1° dip of F1 between T1 and T0 and the 65±1° dip of F2 between T2 and T1,
478 both of which precisely measured in the field (Figures 16 and 17f,g), and similar to that derived
479 from the 2008 Mw6.3 "Damxung" earthquake co-seismic InSAR data (54.4°W, Liu et al., 2012),
480 yield a minimum extension rate on the eastern side of the Yangbajing graben of 0.3±0.1 mm/yr.
481 This results in a total minimum extension rate of 1.2±0.2 mm/yr (0.9 of extension at Ybj M + 0.3

mm/yr) across the southern Yangbajing graben.

5 Discussion

5.1 Review of previous late Quaternary throw rates determination along the south Tibetan grabens

Prior to the widespread use of cosmogenic dating, Armijo et al. (1986) had inferred an onset age of extension across the south Tibetan graben normal faults of ~2.0±0.5 Ma, based on paleontological, stratigraphic and geomorphic observations. Combining such ages with cumulative throws (3-5 km for the YGR, 2.0±0.6 km for other rifts) implied a minimum long-term geological throw rate of 1.0±0.6 mm/yr on most graben's master faults, and of 1.9±0.6 mm/yr (#6b in Figure 19a and Table 3) along the YGR where tectonic relief is the largest. Along the western side of the Yangbajing graben, Armijo et al. (1986) also suggested late Quaternary throw rates of ~1.6 mm/yr (#6a in Figure 19a and Table 3), based on the inference that the offset glacial moraines formed after the last interstadial at 60 ka (inferred 100 m vertical offset in 60 ka, site Ybj moraines). However, taking the Ybj moraines offset to be only 44 m would be consistent with a throw rate of only 0.8 mm/yr.

Overall, the late Quaternary throw rates we obtain and discuss here vary from north to south between 1.8±0.3 mm/yr (Gulu moraines 'GM'), 6.4(+1.7/-1.1) mm/yr (Gulu terraces 'GuT'), 0.5±0.1 - 0.75±0.2 mm/yr (Damxung terraces 'DT'), 0.8±0.1 mm/yr (Ybj moraines 'YM') and 0.6±0.2 mm/yr (Gyekar terraces 'GyT') (Figure 19a and Table 3). Our results are particularly robust at the Gulu moraine and Damxung terraces sites due to precise offset measurements and tightly clustered ages. This is corroborated by the fact that our Gulu moraine ^{10}Be age (recalculated at 22.0±2.0 ka, n=15, Chevalier et al., 2011a) is identical, within error, to that (recalculated at 21.7±2.2 ka, n=8, Owen et al., 2005, class B) of another moraine in the next valley to the south after the oldest sample age

506 (42.6±4.2 ka) was discarded using Peirce criterion.

507 At the late Quaternary timescale, relatively few recent studies have specifically targeted
508 quantitative measurements of throw rates along south Tibetan normal faults. In the Pulan graben, on
509 the west side of the Gurla Mandhata (Figure 1a), Chevalier et al. (2012) determined a minimum
510 throw rate of 1.6±0.4 mm/yr using ^{10}Be cosmogenic dating (34±7 ka) of vertically offset (53±5 m)
511 alluvial surfaces. A maximum rate of 1.9(+0.8/0.5) mm/yr was obtained with a lower terrace offset
512 by 15±1 m in 8.0±2.5 ka. Using the same technique, Kali (2010) measured vertical throw rates of
513 ~1.2 and ~1.7 mm/yr along the western (Kharta) and eastern (Dinggye) normal faults bounding the
514 Ama Drime horst along the Dinggye/Ama Drime graben (Figure 1a), respectively. Along the
515 northern YGR, Wu et al. (2004, 2015) used electron spin resonance (ESR), optically stimulated
516 luminescence (OSL) and U-series dating of vertically offset alluvial surfaces to constrain normal
517 throw rates. Rates of 1.4±0.6 mm/yr during the Holocene and of 1.1±0.3 mm/yr during the
518 Quaternary (#7a and #7ab in Figure 19 and Table 3, respectively) were obtained in the Yangbajing
519 graben (Wu et al., 2004), and of 0.8-1.3 mm/yr (#8) in the Angang graben (Wu et al., 2015). Most
520 of these values correlate well with those we determine here. Finally, along the southern YGR,
521 vertical throw rates of 0.7±0.1 mm/yr (#9, Ha et al., 2019) and of 0.9±0.3 mm/yr (#10, Wang et al.,
522 2020) have recently been constrained using OSL and ^{10}Be cosmogenic dating, respectively.

523 Overall, the combination of these results suggest that late Quaternary/Holocene throw rates
524 across most grabens south of the Bangong-Nujiang suture (BNS) may be similar and on order of ~1
525 to 2 mm/yr. By contrast, north of the BNS, across the prominent Shuanghu rift, significantly slower
526 late Quaternary throw rates <0.3 mm/yr in the last 233 ka, and of 0.2-0.3 mm/yr in the last 120 ka
527 have been obtained using U-series dating of pedogenic carbonates (Blisniuk & Sharp, 2003) and
528 ^{10}Be surface-exposure cosmogenic dating (Pan et al., 2018), respectively. Although these latter
529 results are of narrow regional extent, they tend to support the geomorphic/topographic-based

530 inference that the kinematics of normal faulting north and south of the BNS is different.

531

532 ## 5.2 Extension rates along the northern Yadong-Gulu rift

533 From north to south, the late Quaternary extension rates we determine here vary between
534 6.0±1.8 mm/yr (Gulu moraines), 3.1±0.6 mm/yr (Gulu terraces), < 1.6 mm/yr (Damxung terraces),
535 and a total of 1.2±0.2 mm/yr across the southern Yangbajing graben (0.9±0.1 mm/yr at Ybj
536 moraines + 0.3±0.1 mm/yr at Gyekar terraces) (Figure 19), i.e., 3-6 mm/yr north of the Gulu bend
537 and 1.3±0.3 mm/yr south of it. While the average rates we obtain between Damxung and Gyekar
538 are in fair agreement with those inferred earlier (Armijo et al., 1986), and with those measured
539 along a few other south Tibetan rifts (Wu et al., 2004, 2015; Kali, 2010; Chevalier et al., 2012; Ha
540 et al., 2019; Wang et al., 2020), the rate we determine closer to Gulu (north of the 90° Gulu bend)
541 are not, in keeping with the particularly spectacular and youthful tectonic morphology initially
542 noted by Armijo et al. (1986, 1989).

543 Taken at face value, such rates appear to increase sharply and rapidly northwards,
544 specifically north of the Gulu bend (Figure 19b). We infer that such faster rates might result from a
545 transfer of slip from the Beng Co dextral fault to the Gulu normal fault, the latter absorbing a
546 significant part of the displacement along the former (Armijo et al., 1986, 1989). If this were the
547 case, the present-day slip-rate on the Beng Co fault would be at least 6.0±1.8 mm/yr. Right-lateral
548 late Quaternary slip-rates as fast as 10-20 mm/yr have been inferred along that fault (Armijo et al.,
549 1989; Peltzer & Saucier, 1996), while geodetic, InSAR-based rates have been shown to be between
550 1±1 and 4±1 mm/yr (Garthwaite et al., 2013), <6 mm/yr (Taylor & Peltzer, 2006), and 7.7 mm/yr
551 (Ryder et al., 2014). Recent, ongoing deformation in this region of the Plateau is quite complex, as
552 it combines movements on large normal faults, on long, conjugate, strike-slip faults, and tectonic
553 uplift of several of Tibet's highest (> 7000 m) mountain ranges (Figure 1b). While the origin of such

554 complexity is still poorly understood, it likely reflects significant changes in deformation
555 kinematics since the early Tertiary (e.g., Tapponnier et al., 1986; Harrison et al., 1995). Along the
556 Gulu half-graben, for instance, shallow extension is taken up either by a single, steep normal fault
557 or by widely distributed extensional faults dipping in opposite directions. Southwards near
558 Damxung, deformation is partitioned between normal and sinistral motion along two roughly
559 parallel faults that likely merge at depth (Armijo et al., 1986). The strike of both faults is at high-
560 angle to that of the Beng Co and Jiali dextral faults (Figures 1b, 2 and S1). Finally, although the
561 particularly high elevation of the Nyainqentanghla (NQTL) Range, the steep slope of its NW, 61°-
562 trending range-front, and the presence, along that front, of strongly deformed and folded Cretaceous
563 red beds, may be taken to imply NW-directed Tertiary overthrusting (e.g., Tapponnier et al., 1986;
564 Armijo et al., 1989), consistent with the steep bathymetric gradient along the SE shore of Lake Nam
565 Co (e.g., Kasper et al., 2012), while the more gentle SE side of the NQTL Range exposes a shallow-
566 dipping detachment (e.g., Cogan et al., 1998; Kapp et al., 2005).

567 By statistically averaging the strikes of active normal faults, Armijo et al. (1986) proposed
568 average extension directions of N102°E across the YGR and of ~N96°E±7° across most of the
569 south Tibetan rifts. Both directions are perpendicular to the average rift trends (N6-10°E) and to
570 their bounding normal faults. They are also comparable to the average T axes of regional
571 earthquake focal mechanisms in central/southern Tibet (e.g., Molnar & Lyon-Caen, 1989; Zhu et
572 al., 2017; Wu et al. 2019). Field morphological measurements, outcrop exposures and slickenside
573 data (Tapponnier et al., 1981; Armijo et al., 1986; Mercier et al., 1987) constrain active normal fault
574 dips to range between 45° and 60° (up to 70° near Damxung, Figure S7). Accordingly, based on the
575 throw rate of 1.9±0.6 mm/yr they estimated, Armijo et al. (1986) determined an ~EW extension rate
576 across the northern half of the YGR of 1.4±0.8 mm/yr. Most of the robust dip angle values recently
577 obtained using InSAR and body-wave data for instrumental earthquakes along the YGR and

578 Pumqu-Xainza rifts (e.g., Elliott et al., 2010; H. Wang et al., 2014) are also consistent with steep
579 (41 to 52°) fault planes. Finally, our own field measurements of the two exposed normal fault
580 planes at Gyekar document steep dips of 55±1 and 65±1° (Figures 16b and 17f,g). In summary,
581 despite the influence of a locally complex tectonic history, our quantitative offset/dip/age
582 measurements along the YGR in the Yangbajing graben constrain ~EW extension rates on fairly
583 steep, 41-70° dipping normal faults to be slightly in excess of 1 mm/yr, with a sharp northwards
584 increase, by a factor of ~5, near the Beng Co-Jiali dextral fault.

585 With the exception of our Gulu results, possibly influenced by strike-slip "drag", along the
586 Beng Co-Jiali fault zone, the 1.3±0.3 mm/yr average extension rate we find is similar to, while
587 more precise than, the rate (1.4±0.8 mm/yr) inferred by Armijo et al. (1986). Assuming, as justified
588 by presently available data across some other rifts and by their similar morphologies and widths,
589 comparable extension rates across each of the six other main south Tibetan rifts (from ~81 to
590 ~92°E) with negligible active normal faulting between them, we obtain a total, active extension rate
591 of 9±2 mm/yr across southern Tibet south of the BNS, while the above authors' broader estimate
592 was 10±5.6 mm/yr. The south Tibetan rifts do show differences in geometry, symmetry, and
593 amounts of total exhumation (e.g., Kapp et al., 2008; C. Wang et al., 2014; Styron et al., 2015;
594 Wolff et al., 2019), but it is clear on high-resolution topographic maps and satellite images that
595 from a morphological standpoint, their present-day widths and depths (a measure of active crustal
596 stretching amounts) are fairly similar. Thus, in the absence of comprehensive, quantitative late
597 Quaternary studies across all other rifts, we take our simple estimate of 9±2 mm/yr to best reflect
598 the present-day, southern Tibet extension rate. This value is significantly smaller than that
599 estimated by Molnar and Lyon-Caen (1989) (18±9 mm/yr in a more southeasterly N115°E
600 direction), using the total seismic moment release due to earthquakes between 1962 and 1986 (24
601 years). By contrast, using InSAR data from normal faulting earthquakes in the last 43 years (1966

602 to 2008), a time interval almost twice as long, Elliott et al. (2010) estimated a much slower rate (3-4
603 mm/yr in the EW direction). Besides potential disparities in the EW length of the region considered,
604 such large differences are most likely due to different observation time spans, unknown earthquake
605 recurrence intervals, and event clustering. The 9±2 mm/yr total extension rate is comparable to that
606 predicted by divergent thrusting along the Himalayan arc (Baranowski et al., 1984; Armijo et al.,
607 1986), which requires that the ~EW extension rate across southern Tibet should be about half that
608 of underthrusting of rigid India beneath the Himalayan Range. All recent estimates of central trans-
609 Himalayan shortening across the whole length (~1000 km) of Nepal (e.g., Holocene average of
610 21±1.5 mm/yr, Lavé & Avouac, 2000; GPS average of 19±2.5 mm/yr in central and eastern Nepal,
611 Bettinelli et al, 2006; or 15.5±2 mm/yr, Lindsey et al., 2018) do support an extension rate across
612 southernmost Tibet on order of ~10±1 mm/yr (i.e., half of ~20 mm/yr). Even the latter, slowest
613 convergence would still be in keeping with ~8±1 mm/yr of extension.
614 As an incentive for future research, note that a ~9 mm/yr total extension rate would be
615 comparable to the maximum right-lateral slip-rate determined along the Karakorum fault (Chevalier
616 et al., 2005, 2012), and might be taken to imply a comparable right-lateral slip-rate along the Jiali
617 fault, which likely connects with the NE Sagaing fault south of the Putao pull-apart basin (Figure
618 27 in Armijo et al., 1989).
619
620 5.3 Comparison with geodetic rates
621 Early GPS studies with a limited number of stations across Tibet (Wang et al., 2001; Zhang
622 et al., 2004) suggested a total extension rate of ~20-22 mm/yr between ~79° and ~93°E. The recent,
623 wholesale East Asia GPS dataset of Zheng et al. (2017) suggests a uniformly distributed extension
624 rate of ~15 mm/yr across all of southern Tibet (~1500 km). Taking the shorter distance (only ~1000
625 km) between the westernmost (Gurla Mandhata) and easternmost (Cona) rifts that limit the area we

626 consider (Figure 1a) would yield a rate of ~10 mm/yr, similar to the 9±2 mm/yr southern Tibet
627 extension rate we propose. The GPS/InSAR joint inversion results of Wang et al. (2019) suggest a
628 total ~15 mm/yr of EW extension across south-central Tibet (between 80 and 92°E). According to
629 these authors, the Lopu Kangri rift (northward extent of the Thakkhola rift), the Tangra Yum Co
630 rift, and the YGR would absorb similar amounts of extension (4-5 mm/yr each, #1 in Figure 19a
631 and Table 3). The Pumqu-Xainza rift (Figure 1a), on the other hand, would absorb only 1-2 mm/yr
632 (Wang et al., 2019).

633 Other GPS studies, such as that of Chen et al. (2004a,b), suggested a total extension rate of
634 9.7±3.0 mm/yr across all rifts, with ~6 mm/yr across the YGR (#2 in Figure 19a and Table 3), and
635 much of the rest (~4 mm/yr) across the Thakkhola graben, even though their GPS estimates
636 encompass a broader area than that constrained by geological studies, a potential source of
637 discrepancies. Note that the YGR and Thakkhola rifts, were singled out by Replumaz and
638 Tapponnier (2003) to be the most active of all south Tibetan rifts, in the last 5 Ma. Compatible GPS
639 values of 5.2±0.4 and 7.8±0.4 mm/yr across the same two rifts were obtained by Wang et al. (2017)
640 (#3). Interestingly, it is also along these two rifts (Lopu Kangri/Thakkhola and YGR) that the
641 greatest number of M>6 earthquakes have occurred north of the Yarlung Zangbo suture (YZS) in
642 the last 40 years (Figure 1a). Later GPS studies (Gan et al., 2007) found a 2.0±0.6 mm/yr extension
643 rate across the YGR (#4), roughly consistent with that inferred by Armijo et al. (1986) (1.4±0.8
644 mm/yr) and with our own rate south of the Gulu bend (1.3±0.3 mm/yr), as well as a left-lateral
645 strike-slip rate of 0.7±1.1 mm/yr, also in keeping with our left-lateral slip-rate near Damxung
646 (0.9±0.3 mm/yr). Finally, in a recent 3D micro-block kinematic model, Tian et al. (2019) used
647 geodetic and seismic observations to infer an extension rate of 5.6±0.8 mm/yr in the northern YGR
648 (#5 in Figure 19a and Table 3), which would be consistent with our faster local result. However,
649 their model also yields a right-lateral slip-rate component of 1.4±0.9 mm/yr in the same area, while

650 the NE-trending active transfer segment between Yangbajing and Gulu unquestionably entails a
651 significant component of left-lateral faulting.
652
653 5.4 Implications for present-day Tibetan deformation
654 Armijo et al. (1986) suggested that the 'chord' between the eastern and western Himalayan
655 syntaxes, which appears to guide localized, en-echelon, right-lateral shear roughly along the older
656 BNS, separates two regions with different deformation regimes (Figure 20). To the north (between
657 the Altyn Tagh fault and the BNS, Figure 1a), dominant strike-slip faulting earthquakes occur
658 within the Qiangtang block (e.g., Molnar & Tapponnier, 1978; Molnar & Chen, 1983; Molnar &
659 Lyon-Caen, 1989; Zhu et al., 2017; Wu et al., 2019), which is free to move eastwards. With the
660 exception of the large strike-slip events close to the Karakorum-Jiali Fault Zone (KJFZ), along the
661 Beng Co (BCF), Gyaring Co (GCF) and Damxung faults (1951, Mw7.7; 1934, M~7; and 1411,
662 M~8, respectively) (Figure 1a), normal faulting earthquakes predominate across the Lhasa block
663 (between the BNS and the Yarlung Zangbo suture), which is restrained to the east and west by the
664 two Himalayan Syntaxes (Armijo et al., 1986). Hence, prevailing sinistral strike-slip faulting in
665 central Tibet north of the BNS likely reflects the eastwards extrusion of the Qiangtang block mostly
666 along the Gyaring Co and Beng Co faults (e.g., Peltzer & Tapponnier, 1988; Wu et al., 2011; Han et
667 al., 2019), while the Lhasa block to the south extends as a result of divergent orthogonal thrusting
668 along the Main Frontal Thrust (e.g., Baranowski et al, 1984; Armijo et al., 1986) (Figure 20). Other
669 models have inferred a significant role of underthrusting of Indian lower crust beneath the plateau
670 (e.g., DeCelles et al., 2002; Styron et al., 2015) and/or of oblique convergence (mostly in the
671 western Himalaya, Styron et al., 2011; Murphy et al., 2014). That faulting north and south of the
672 BNS results from different processes is consistent with the much smaller strike-slip displacements
673 inferred along the NE-striking central Tibet sinistral faults (~10-20 km, Taylor et al., 2003; Yin &

674 Taylor, 2011) than along the dextral Karakorum fault (>120 km offset of the Indus River, e.g.,
675 Gaudemer et al., 1989; Robinson, 2009; and >250 km geological offset, Matte et al., 1996; Lacassin
676 et al., 2004; Valli et al., 2007).
677
678 5.5 Recent seismicity and long-term return times
679 Up to 14 earthquakes with M>6 (EDPDCEA earthquake catalogs, 1999), 12 of which
680 between the Yarlung Zangbo and the Bangong-Nujiang sutures, occurred along or near the Yadong-
681 Gulu rift (YGR) prior to the 2008 Mw6.3 "Damxung" earthquake near Gyekar. The oldest and
682 largest known events are the 1264 Yangyi M6.7, and the 1411 Damxung-Yangbajing M8 (?)
683 earthquakes. The latter is inferred to have produced ~136 km of surface rupture, with maximum
684 vertical and horizontal displacements of 8-9 and 11-13 m, respectively, between Damxung and
685 Yangbaijing (Wu et al., 1992). All the other events postdate the advent of instrumental seismology
686 at the end of the 19th century. They include the 1901 North Nimu (Nyemo?) M6.8 earthquake, the
687 1924 Nimu M6 earthquake, the 1924 Yalin graben (west of Yangbaijing) M6.5 earthquake, the
688 1951-1952 Beng Co/Gulu Mw7.7-7.4 earthquake sequence (with ~90 km of surface ruptures,
689 Armijo et al., 1989), and the 1992 Nyemo Mw6.1 earthquake (Figure 1b). The remaining seismic
690 gap between the Angang and the Yangbaijing grabens was apparently partly filled by the 2008
691 earthquake. Liu et al. (2012) suggested an earthquake recurrence interval along the southern
692 Yangbajing graben (also called Yangyi graben) of 744 years, based on the time elapsed between the
693 1264 and the 2008 events. Assuming that the last event released all the accumulated strain, they
694 inferred a long-term slip-rate of ~1.8 mm/yr, derived from the InSAR-based seismic slip (1.33 m)
695 and the recurrence interval (744 years). Note that this value would imply an extension rate of ~1
696 mm/yr across only the eastern side of the southern Yangbaijing graben. It would thus be roughly
697 consistent with the loosely constrained values estimated across the whole graben by Armijo et al.

(1986) (1.4 ±0.8 mm/yr) and Gan et al. (2007) (2.0±0.6 mm/yr). On the other hand, it would be larger than the minimum value we obtain (0.3±0.1 mm/yr) on just the graben's eastern side.

Only one large earthquake (M8?, 1411) is inferred to have ruptured the entire length of the ~150 km-long Damxung corridor (Wu et al., 1992). Although six M5+ events occurred during the first half of the 19th century near the NE tip of the corridor (Figure 1b), one of which possibly an aftershock of the 1951 sequence, the major part of the fault inferred to have ruptured in 1411 shows no field evidence of a very fresh, modern surface rupture, including on high-resolution satellite images. Using the rates we determined between Damxung and Gulu (~1.6 to 6 mm/yr) and the time elapsed since the last large event (608 years) would yield a slip deficit of 1-4 m, much smaller than the co-seismic horizontal slip values (11-13 m) inferred for the 1411 event. Thus, a return of a comparatively large event in this part of the rift is not expected in the foreseeable future. but it is clear that paleoseismologic and additional detailed geomorphic dating are needed between Damxung and Gulu to assess the return times of very large earthquakes similar to the 1411 and 1951-1952 events.

6 Conclusion

After a careful discussion of the individual ^{10}Be and ^{26}Al cosmogenic surface-exposure ages we obtained on each of the two moraines and three alluvial surfaces, that are vertically offset by active normal faults along the northern Yadong-Gulu rift (YGR), most prominent of the seven ~NS-trending rifts in southern Tibet, we quantitatively determined throw and extension rates along that rift between the Yarlung Zangbo (YZS) and Bangong-Nujiang (BNS) sutures. Extension rates are found to rapidly decrease southwards from 6.0±1.8 and 3.1±0.6 mm/yr north of the 90° Gulu bend, to an average of 1.3±0.3 mm/yr south of it. The fast rates to the north are in fair agreement with regional geodetic (GPS and InSAR) measurements. We interpret the change to reflect partial

722 transfer of slip southwards from the right- lateral Beng Co fault, whose slip-rate should thus not be
723 less than 6 mm/yr. Our late Quaternary average rate south of the Gulu bend is comparable to other
724 quantitatively constrained rates along other south Tibetan rifts south of the BNS (~1 to 2 mm/yr).
725 Such rates appear faster than the few measured rates (<0.3 mm/yr) north of the BNS, consistent
726 with the geomorphic and topographic differences on either side of that suture. Even though
727 additional quantitative data from other south Tibetan rifts remain crucial to better constrain a total,
728 regional extension rate between ~81 an ~92°E, assuming a similar average rate (1.3±0.3 m/yr)
729 across each of the seven south Tibetan grabens between the Gurla Mandhata/Pulan and Cona rifts
730 (~1000 km apart) yields a total ~EW extension rate of 9±2 mm/yr. This value is comparable to,
731 albeit on the lower side of estimates based on the use of geodetic data across the same ~EW stretch
732 of southern Tibet. It amounts to about half of the total convergence rate (between 14 and 21 mm/yr)
733 between India and Asia along Nepal's Himalayan Main Frontal Thrust, and is thus consistent with a
734 simple model of divergent, orthogonal thrusting of southern Tibet atop a rigid Indian plate.
735

736 **Acknowledgements**

737 This project was financially supported by the CNRS-INSU-DyETI 2004-83, the National Key
738 Research and Development Project of China (2016YFC0600310), the 2nd Tibetan Plateau
739 Scientific Expedition of the Ministry of Science and Technology of China (2019QZKK0901), the
740 Natural National Science Foundation of China (NSFC 41672211, 41672210), the China Geological
741 Survey (DD20190057, DD20190059), the Basic Research Funds of the Institute of Geology, CAGS
742 (JYYWF201810, JYYWF201821), and the European Marie Sklodowska-Curie Outgoing
743 International Fellowship FP6 (040070) to MLC. We thank Robin Lacassin and Peiquan Zhang for
744 their help in the field. All data from this paper are presented in Tables 1 and 2. We are grateful to
745 the Associate Editor P. DeCelles and to J.E. Saylor and K. Sundell for their detailed and insightful

746 reviews.

747

748 **References**

749 Achache, J., Courtillot, V., & Zhou, Y. (1984), Paleogeographic and tectonic evolution of southern
750 Tibet since Middle Cretaceous time: New paleomagnetic data and synthesis. *Journal of*
751 *Geophysical Research*, 89, B12, doi:10.1029/JB089iB12p10311.

752 Armijo, R., Tapponnier, P., Mercier, J. L., & Han, T. L. (1986), Quaternary extension in southern
753 Tibet: Field observations and tectonic implications. *Journal of Geophysical Research,* 91,
754 13,803 – 13,872.

755 Armijo, R., Tapponnier, P., & Tonglin, H. (1989), Late Cenozoic right-lateral strike-slip faulting in
756 southern Tibet. *Journal of Geophysical Research,* 94, 2787 – 2838.

757 Avouac, J.P., & Tapponnier, P. (1993), Kinematic model of active deformation in central Asia.
758 *Geophysical Research Letters*, 20, 895–898.

759 Avouac, J.P., Tapponnier, T., Bai, M., You, H., & Wang, G. (1993), Active thrusting and folding
760 along the northern Tien Shan and Late Cenozoic rotation of the Tarim relative to Dzungaria
761 and Kazakhstan. *Journal of Geophysical Research,* 98*,* 6755-6804*,* doi:10.1029/92JB01963.

762 Balco, G., Stone, J. O., Lifton, N. A., & Dunai, T. J. (2008), A complete and easily accessible
763 means of calculating surface exposure ages or erosion rates from ^{10}Be and ^{26}Al
764 measurements. *Quaternary Geochronology,* 3 (3), 174–195.
765 doi:10.1016/j.quageo.2007.12.001.

766 Batbaatar, J., Gillespie, A.R., Fink, D., Matmon, A., & Fujioka, T. (2018),
767 Asynchronous glaciations in arid continental climate. *Quaternary Science Reviews,*
768 182, 1–19.

769 Baranowski, J., Armbruster, J., Seeber, L. & Molnar, P. (1984), Focal depths and fault plane

770 solutions of earthquakes and active tectonics of the Himalaya. *Journal of Geophysical*
771 *Research,* 89, 6918-6928.
772 Bettinelli, P., Avouac, J.P., Flouzat, M., Jouanne, F., Bollinger, L., Willis, P., & Chitrakar, G.R.,
773 (2006), Plate motion of India and interseismic strain in the Nepal Himalayan from GPS and
774 DORIS measurements. *Journal of Geodesy*, 80, 567–589.
775 Blisniuk, P., Hacker, B., Glodny, J., Ratschbacher, L., Bi, S., Wu, Z. et al. (2001), Normal faulting
776 in central Tibet since at least 13.5 Myr ago. *Nature,* 412, 628 – 632.
777 Blisniuk, P.M., & Sharp, W.D. (2003), Rates of late Quaternary normal faulting in central Tibet
778 from U-series dating of pedogenic carbonate in displaced fluvial gravel deposits. *Earth and*
779 *Planetary Science Letters,* 215(1 – 2), 169–186.
780 Blomdin, R., Stroeven, A. P., Harbor, J. M., Lifton, N. A., Heyman, J., Gribenski, N., et al. (2016),
781 Evaluating the timing of former glacier expansions in the Tian Shan: a key step towards
782 robust spatial correlations. *Quaternary Science Reviews,* 153, 78–96,
783 doi:10.1016/j.quascirev.2016.07.029.
784 Burchfiel, B. C., Chen, Z., Hodges, K. V., Liu, Y., Royden, L. H., Deng, C. & Xu, J. (1992), The
785 South Tibetan Detachment System, Himalayan orogen: Extension contemporaneous with
786 and parallel to shortening in a collisional mountain belt. *Special Paper Geological Society of*
787 *America,* 269, 41 pp.
788 Chen, Q., Freymueller, J. T., Yang, Z., Xu, C., Jiang, W., Wang, Q., & Liu, J. (2004a), Spatially
789 variable extension in southern Tibet based on GPS measurements. *Journal of Geophysical*
790 *Research,* 109(B09401). doi:10.1029/2002JB002350.
791 Chen, Q., Freymueller, J. T., Wang, Q., Yang, Z., & Xu, C. (2004b). A deforming block model for
792 the present-day tectonics of Tibet. *Journal of Geophysical Research,* 109(B01403).
793 doi:10.1029/2002JB002.

794 Chevalier, M.-L., Ryerson, F. J., Tapponnier, P., Finkel, R. C., Van Der Woerd, J., Haibing, L.,
795 & Qing, L. (2005), Slip-rate measurements on the Karakorum fault may imply secular
796 variations in fault motion. *Science,* 307, 411–414. doi:10.1126/science.1105466.
797 Chevalier, M.-L., Hilley, G., Tapponnier, P., Van Der Woerd, J., Liu-Zeng, J., Finkel, R. C., et al.
798 (2011a), Constraints on the late Quaternary glaciations in Tibet from cosmogenic exposure
799 ages of moraine surfaces. *Quaternary Science Reviews,* 30 (5–6), 528–554.
800 doi:10.1016/j.quascirev.2010.11.005.
801 Chevalier, M.L., Li, H., Pan, J., Pei, J., Wu, F., Xu, W., Sun, Z., & Liu, D. (2011b), Fast slip-rate
802 along the northern end of the Karakorum fault system, Western Tibet. *Geophysical*
803 *Research Letters*, 38, L22309, doi:10.1029/2011GL049921.
804 Chevalier, M.-L., Tapponnier, P., Van der Woerd, J., Ryerson, F. J., Finkel, R., & Li, H. (2012),
805 Spatially constant slip rate along the southern segment of the Karakorum fault since 200 ka.
806 *Tectonophysics,* 530/531, 152-179. doi:10.1016/j.tecto.2011.12.014.
807 Chevalier, M.-L., & Replumaz, A. (2019), Deciphering old moraine age distributions in SE Tibet
808 showing bimodal climatic signal for glaciations: Marine Isotope Stages 2 and 6. *Earth and*
809 *Planetary Science Letters,* 507, 105-118. doi:10.1016/j.epsl.2018.11.033.
810 Clark, P. U., Dyke, A. S., Shakun, J. D., Carlson, A. E., Clark, J., Wohlfarth, B., et al. (2009), The
811 Last Glacial Maximum. *Science,* 325, 710–714. doi:10.1126/science.1172873.
812 Cogan, M. J., Nelson, K . D., Kidd, W. S. F., Wu, C., & Project INDEPTH Team (1998), Shallow
813 structures of the Yadong- Gulu Rift, southern Tibet, from refraction analysis of Project
814 INDEPTH common midpoint data. *Tectonics,* 17*,* 46 – 61.
815 Copley, A., Avouac, J. P. & Wernicke, B. P. (2011), Evidence for mechanical coupling and strong
816 Indian lower crust beneath southern Tibet. *Nature,* 472(7341), 79–81.
817 Currie, B.S., Rowley, D.B., & Tabor, N.J. (2005), Middle Miocene paleoaltimetry of southern

818 Tibet: implications for the role of mantle thickening and delamination in the Himalayan
819 orogen. *Geology,* 33, 181–84
820 DeCelles, P., Robinson, D., & Zandt, G. (2002), Implications of shortening in the Himalayan fold-
821 thrust belt for uplift of the Tibetan Plateau. *Tectonics* 21, 6, 1062,
822 doi:10.1029/2001TC001322.
823 DeCelles, P., Quade, J., Kapp, P., Fan, M., Dettman, D., & Ding, L. (2007), High and dry in central
824 Tibet during the Late Oligocene. *Earth and Planetary Science Letters*, 253, 389–401.
825 Ding, L., Spicer, R.A., Yang, J., Xu, Q., Cai, F., Li, S., et al. (2017), Quantifying the rise of the
826 Himalaya orogen and implications for the South Asian monsoon. *Geology*, 45, 215-218.
827 Dong G., Yi, C., & Caffee, M. W. (2014), ^{10}Be dating of boulders on moraines from the last glacial
828 period in the Nyainqentanglha mountains, Tibet. *China Earth Sciences,* 57, 221–231.
829 Dong, G., Xu, X., Zhou, W., Fu, Y., Zhang, L., & Li, M. (2017), Cosmogenic ^{10}Be surface
830 exposure dating and glacier reconstruction for the last glacial maximum in the quemuqu
831 valley, western Nyainqentanglha mountains, south Tibet. *Journal of Quaternary Science*,
832 32, 639-652.
833 Earthquake Disaster Prevention Department of China Earthquake Administration (EDPDCEA)
834 (1999), *Catalogue of historical earthquakes in China. Earthquake Press, Beijing, China.* (In
835 Chinese).
836 Elliott, J. R., Walters, R. J., England, P. C., Jackson, J. A., Li, Z., & Parsons, B. (2010), Extension
837 on the Tibetan Plateau: Recent normal faulting measured by InSAR and body wave
838 seismology. *Geophysical Journal International,* 183(2)*,* 503–535.
839 England, P., & Houseman, G. (1989), Extension during continental convergence, with application
840 to the Tibetan plateau. *Journal of Geophysical Research,* 94*,* 17,561 – 17,579.
841 Fielding, E., Isacks, B., Barazangi, M., & Duncan, C. (1994), How flat is Tibet? *Geology*, 22, 163-

842 167. doi:10.1130/0091-7613(1994)022<0163:HFIT>2.3.CO;2.
843 Gan, W., Zhang, P., Shen, Z., Niu, Z., Wang, M., Wan, Y., & Cheng, J. (2007), Present-day
844 crustal motion within the Tibetan Plateau inferred from GPS measurements. *Journal of*
845 *Geophysical Research,* 112(B08416). doi:10.1029/2005JB004120.
846 Garthwaite, M. C.,Wang, H., & Wright, T. J. (2013), Broadscale interseismic deformation and fault
847 slip rates in the central Tibetan Plateau observed using InSAR. *Journal of Geophysical*
848 *Research,* 118*,* 5071–5083. doi:10.1002/jgrb.50348.
849 Garzione, C. N., Dettman, D. L., Quade, J., DeCelles, P. G., & Butler, R. F. (2000), High times on
850 the Tibetan Plateau: Paleoelevation of the Thakkola graben, Nepal. *Geology*, 28, 339–342,
851 doi:10.1130/0091-7613(2000)28¤339:HTOTTP2.0.CO;2.
852 Gasse, F., Arnold, M., Fontes, J. C., Fort, M., Gibert, E., Huc, A., et al. (1991), A 13,000 year
853 climate record from Western Tibet. *Nature,* 353, 742–745.
854 Gaudemer, Y., Tapponnier, P., & Turcotte, D. L. (1989), River offsets across active strike slip
855 faults. *Annales Tectonicae,* 3(2)*,* 55-76.
856 Gosse, J., & Phillips, F. (2001), Terrestrial in situ cosmogenic nuclides: theory and application.
857 *Quaternary Science Reviews,* 20*,* 1475–1560.
858 Ha, G., Wu, Z., & Liu, F. (2019), Late Quaternary vertical slip rates along the Southern Yadong–
859 Gulu Rift, Southern Tibetan Plateau. *Tectonophysics,* 755*,* 75-90.
860 doi:10.1016/j.tecto.2019.02.014.
861 Han, S., Li, H., Pan, J., Lu, H., Zheng, Y., Liu , D., & Ge, C. (2019), Co-seismic surface ruptures in
862 Qiangtang Terrane: Insight into Late Cenozoic deformation of central Tibet.
863 *Tectonophysics,* 750*,* 359-378. doi:10.1016/j.tecto.2018.11.001.
864 Harrison, T. M., Copeland, P., Kidd, W. S. F., & Yin, A., (1992), Raising Tibet. *Science*, 255,
865 1663–1670.

866 Harrison, T. M., Copeland, P., Kidd, W. S., & Lovera, O. M. (1995), Activation of the
867 Nyainqentanghla shear zone: Implications for uplift of the southern Tibetan Plateau.
868 *Tectonics,* 14*,* 658 – 676.
869 Heyman, J. (2014), Paleoglaciation of the Tibetan Plateau and surrounding mountains based on
870 exposure ages and ELA depression estimates. *Quaternary Science Reviews,* 91*,* 30–41.
871 doi:10.1016/j.quascirev.2014.03.018.
872 Hirn, A., Nercessian, A., Sapin, M., Jobert, G., Xu, Z., Gao, E., et al. (1984), Lhasa block and
873 bordering sutures-A continuation of 500 km Moho traverse through Tibet. *Nature*, 307, 25-
874 27, 1984.
875 Kali, E. (2010), De la déformation long-terme à court-terme sur les failles normales du Sud-Tibet:
876 approche géochronologique multi-méthode (10Be, 26Al, (U-Th)/He, 40Ar/39Ar, U/Pb, 0-
877 361., *PhD thesis, EOS Strasbourg, France*.
878 Kapp, P., & Guynn, J.H. (2004), Indian punch rifts Tibet. *Geology,* 32, 993–996.
879 Kapp, J. L., Harrison, T. M., Kapp, P., Grove, M., Lovera, O. M., & Lin, D. (2005),
880 Nyainqentanglha Shan: A window into the tectonic, thermal, and geochemical evolution of
881 the Lhasa block, southern Tibet. *Journal of Geophysical Research,* 110(B08413).
882 doi:10.1029/2004JB003330.
883 Kapp, P., Taylor, M., Stockli, D., & Ding, L. (2008) Development of active low-angle normal fault
884 systems during orogenic collapse: Insight from Tibet. *Geology,* 36, 7–10.
885 Kasper T, Haberzettl T, Doberschutz S. et al. (2012), Indian Ocean Summer Monsoon (IOSM)-
886 dynamics within the past 4 ka recorded in the sediments of Lake Nam Co, central Tibetan
887 Plateau (China). *Quaternary Science Reviews,* 39: 73–85.
888 Kohl, C.P., & Nishiizumi, K. (1992), Chemical isolation of quartz for measurement of in situ
889 produced cosmogenic nuclides. *Geochimica et Cosmochimica Acta,* 56*,* 3583–3587.

890 Lacassin, R., Valli, F., Arnaud, N., Leloup, P. H., Paquette, J. L., Li, H., Tapponnier, P., et al.
891 (2004), Large-scale geometry, offset and kinematic evolution of the Karakorum fault, Tibet.
892 *Earth and Planetary Science Letters,* 219*,* 255–269. doi:10.1016/S0012-821X(04)00006-8.
893 Lal, D. (1991), Cosmic ray labeling of erosion surfaces: in situ nuclide production rates and erosion
894 models. *Earth and Planetary Science Letters, 104,* 429–439.
895 Lavé, J. & Avouac, J. P. (2000), Active folding of fluvial terraces across the Siwaliks Hills,
896 Himalayas of central Nepal. *Journal of Geophysical Research*, 105, 3, 5735–5770,
897 doi:10.1029/1999JB900292.
898 Lee, J., C. Hager, S. R. Wallis, D. F. Stockli, M. J. Whitehouse, M. Aoya, & Y. Wang (2011),
899 Middle to late Miocene extremely rapid exhumation and thermal reequilibration in the Kung
900 Co rift, southern Tibet. *Tectonics*, 30, TC2007, doi:10.1029/2010TC002745.
901 Leloup, P. H., Mahéo, G., Arnaud, N., Kali, E., Boutonnet, E., Liu, D., et al. (2010), The South
902 Tibet detachment shear zone in the Dinggye area Time constraints on extrusion models of
903 the Himalayas. *Earth and Planetary Science Letters,* 292**,** 1-16.
904 Li, H., Van der Woerd, J., Tapponnier, P., Klinger, Y. Qi, X., Yang, J., & Zhu Y., (2005), Slip rate
905 on the Kunlun fault at Hongshui Gou, and recurrence time of great events comparable to
906 the 14/11/2001, Mw~7.9 Kokoxili earthquake. *Earth and Planetary Science Letters,* 237,
907 285-299.
908 Li, K., Wang, D., Shao, Q., & Xu, X., (2018), Holocene sip rate along the NE-trending Qixiang Co
909 fault in the central Tibetan Plateau and its tectonic implications. *Seismology and Geology*,
910 40 (6). doi:10.3969/j.issn.0253-4967.2018.06.002.
911 Li, K., Kirby, E., Xu, X., Chen, G., Ren, J., & Wang, D. (2019), Rates of Holocene normal faulting
912 along the Dong Co fault in central Tibet, based on 14C dating of displaced fluvial terraces.
913 *Journal of Asian Earth Sciences*, doi:10.1016/j.jseaes.2019.103962.

914 Lindsey, E. O., Almeida, R., Mallick, R., Hubbard, J., Bradley, K., Tsang, L. L. H., et al. (2018),
915 Structural control on downdip locking extent of the Himalayan megathrust. *Journal of*
916 *Geophysical Research*, 123, 5265–5278. doi:10.1029/2018JB015868.
917 Lisiecki, L.E., & Raymo, M.E. (2005), A Pliocene–Pleistocene stack of 57 globally dis-tributed
918 benthic δ18O records. *Paleoceanography,* 20 (1). doi:10.1029/2004PA001071.
919 Liu,Y., Xu, C., Wen, Y., He, P., & Jiang, G. (2012), Fault rupture model of the 2008 Dangxiong
920 (Tibet, China) Mw 6.3 earthquake from Envisat and ALOS data. *Advances in Space*
921 *research,* 50*,* 952-962. doi:10.1016/j.asr.2012.06.006.
922 Liu-Zeng, J., Tapponnier, P., Gaudemer, Y., & Ding, L. (2008), Quantifying landscape differences
923 across the Tibetan plateau: Implications for topographic relief evolution. *Journal of*
924 *Geophysical Research,* 113, F04018, doi:10.1029/2007JF000897.
925 Mahéo, G., Leloup, P. H., Valli, F., Lacassin, R., Arnaud, N., Paquette, J.-L., et al. (2007), Post 4
926 Ma initiation of normal faulting in southern Tibet. *Earth and Planetary Science Letters,* 256*,*
927 233–243. doi:10.1016/j.epsl.2007.01.029.
928 Matte, P., Tapponnier, P., Arnaud, N., Bourjot, L., Avouac, J.P., Vidal, P., Liu, Q., Pan, Y., and
929 Wang, Y. (1996), Tectonics of western Tibet, between the Tarim and the Indus. *Earth and*
930 *Planetary Science Letters*, 142, 311–330, doi: 10 .1016 /0012 -821X (96)00086 -6 .
931 McCaffrey, R., & Nabelek, J. (1998), Role of oblique convergence in the active deformation of the
932 Himalayas and southern Tibet plateau. *Geology,* 26*,* 691–694.
933 Mercier, J. L., Armijo, R., Tapponnier, P., Carey-Gailhardis, E. & Han, T. (1987), Change from
934 Tertiary compression to Quaternary extension in southern Tibet during the India-Asia
935 collision. *Tectonics,* 6*,* 275-304.
936 Mériaux, A. S., Tapponnier, P., Ryerson, F. J., Xu, X., King, G., Van der Woerd, J., et al. (2005),
937 The Aksay segment of the northern Altyn Tagh fault: Tectonic geomorphology, landscape

938 evolution, and Holocene slip rate. *Journal of Geophysical Research*, 110, B04404,
939 doi:10.1029/2004JB003210.
940 Molnar, P., & Tapponnier, P. (1978), Active tectonics of Tibet. *Journal of Geophysical Research,*
941 83*,* 5361–5375.
942 Molnar, P., & Chen, W. P. (1983), Focal Depths and Fault Plane Solutions of Earthquakes under
943 the Tibetan Plateau. *Journal of Geophysical Research,* 88*,* 1180-1196.
944 Molnar, P., & Lyon-Caen, H. (1989), Fault plane solutions of earthquakes and active tectonics of
945 the Tibetan Plateau and its margins. *Geophysical Journal International,* 99*,* 123 – 153.
946
947 Murphy, M.A., Taylor, M.H., Gosse, J., Silver, C.R.P., Whipp, D.M., & Beaumont, C. (2014),
948 Limit of strain partitioning in the Himalaya marked by large earthquakes in western Nepal.
949 *Nature Geoscience*, 7, 38-42.
950 Ni, J., & York, J. E. (1978), Late Cenozoic tectonics of the Tibetan Plateau. *Journal of Geophysical*
951 *Research,* 83*,* 5377–5384.
952 Owen, L. A., Finkel, R. C., Barnard, P. L., Haizhou, M., Asahi, K., Caffee, M. W., & Derbyshire, E.
953 (2005), Climatic and topographic controls on the style and timing of Late Quaternary
954 glaciation throughout Tibet and the Himalaya defined by ^{10}Be cosmogenic radionuclide
955 surface exposure dating. *Quaternary Science Reviews,* 24*,* 1391–1411.
956 Owens, T.J., & Zandt, G. (1997), Implications of crustal property variations for models of Tibetan
957 plateau evolution: *Nature*, v. 387, p. 37–43.

958 Pan, J., Li, H., Sun, Z., Liu, D., Lu, H., Zheng, Y., & Chevalier, M.L. (2018), Reassessment of the
959 late Quaternary slip rate of the Shuanghu graben, central Tibet, *AGU Fall Meeting*.

960 Patriat, P., & Achache, J. (1984), India-Eurasia collision chronology has implications for crustal
961 shortening and driving mechanism of plates. *Nature*. 311, 615–621. doi:10.1038/311615a0.

962 Peltzer, G., & Tapponnier, P. (1988), Formation and evolution of strike-slip faults, rifts, and basins
963 during the India-Asia collision: An experimental approach. *Journal of Geophysical*
964 *Research*, 93, 15085-15117.
965 Peltzer, G., & Saucier, F. (1996), Present-day kinematics of Asia derived from geologic fault rates.
966 *Journal of Geophysical Research,* 101, 27,943–27,956.
967 Ratschbacher, L., Krumrei, I., Blumenwitz, M., Staiger, M., Gloaguen, R., Miller, B. V., et al.
968 (2011), Rifting and strike-slip shear in central Tibet and the geometry, age and kinematics of
969 upper crustal extension in Tibet. Geological *Society of London Special Publication,* 353(1),
970 127–163.
971 Replumaz, A. & Tapponnier, P. (2003), Reconstruction of the deformed collision zone between
972 India and Asia by backward motion of lithospheric blocks. *Journal of Geophysical*
973 *Research,* 108. doi:10.1029/2001jb000661.
974 Robinson, A.C. (2009), Geologic offsets across the northern Karakorum fault: implications for its
975 role and terrane correlations in the western Himalayan–Tibetan orogen. *Earth and Planetary*
976 *Science Letters,* 279, 123–130. doi:10.1016/j.epsl.2008.12.039.
977 Roger, F., Tapponnier, P., Arnaud, N., Scharer, U., Brunel, M., Xu., Z., Yang, J. (2000), An Eocene
978 magmatic belt across central Tibet: mantle subduction triggered by the Indian collision?
979 *Terra Nova*, 12, 102-108.
980 Rowley, D.B. & Currie B.S. (2006), Palaeo-altimetry of the late Eocene to Miocene Lunpola basin,
981 central Tibet. *Nature* 439:677–81.
982 Ryder, I., Wang, H., Bie, L., & Rietbrock, A. (2014), Geodetic imaging of late postseismic lower
983 crustal flow in Tibet. *Earth and Planetary Science Letters,* 404, 136–143.
984 Sanchez, V. I., Murphy, M. A., Dupre, M.R., Ding, L., & Zhang, R. (2010), Structural evolution of
985 the Neogene Gar Basin, western Tibet: Implications for releasing bend development and

986 drainage patterns. *Geological Society of America Bulletin*, 122, 5/6, 926–945,
987 doi:10.1130/B26566.1.
988 Spicer, R.A., Harris, N.B.W., Widdowson, M., Herman, A.B., Guo, S., et al. (2003), Constant
989 elevation of southern Tibet over the past 15 million years. *Nature,* 421:622–24
990 Stone, J.O. (2000), Air pressure and cosmogenic isotope production. *Journal of Geophysical*
991 *Research,* 105*,* 23,753-23,759.
992 Styron, R., Taylor, M., & Murphy, M. A. (2011), Oblique convergence, arc-parallel extension, and
993 the role of strike-slip faulting in the High Himalaya. *Geosphere* 7, 582–596.
994 Styron, R., M. Taylor, K.E. Sundell, D. F. Stockli, J. A. G. Oalmann, A.Mšller, A. T. McCallister,
995 D. Liu, & L. Ding (2013), Miocene initiation and acceleration of extension in the South
996 Lunggar rift, western Tibet: Evolution of an active detachment system from structural
997 mapping and (U-Th)/He thermochronology, *Tectonics*, 32, 1–28, doi:10.1002/tect.20053.
998 Styron, R.H., Taylor, M., & Sundell, K. (2015), Accelerated extension of Tibet linked to the
999 northward underthrusting of Indian crust. *Nature Geoscience,* 8, 131–134.
1000 doi:10.1038/NGEO2336.
1001 Sundell, K. E., Taylor, M. H., Styron, R. H., Stockli, D. F., Kapp, P., Hager, C., Liu, D., & Ding, L.
1002 (2013), Evidence for constriction and Pliocene acceleration of east-west extension in the
1003 North Lunggar rift region of west central Tibet. *Tectonics* 32:1454–1479.
1004 Tapponnier, P., Mercier, J. L., Armijo, R., Han, T., & Zhao, T. J. (1981), Field evidence for active
1005 normal faulting in Tibet. *Nature,* 294*,* 410 – 414.
1006 Tapponnier P., Peltzer, G., & Armijo, R. (1986), On the mechanics of the collision between India
1007 and Asia, Collision Tectonics, edited by J.G. Ramsay, M.P. Coward, and A. Ries. *Special*
1008 *Publication of the Geological Society of London,* 19*,* 115-157.
1009 Tapponnier, P., Xu, Z., Roger, F., Meyer, B., Arnaud, N., Wittlinger, G., & Yang, J. (2001),

1010 Oblique stepwise rise and growth of the Tibet Plateau. *Science*, 294, 1671–1677.
1011 Taylor, M., Yin, A., Ryerson, F. J., Kapp, P., & Ding, L. (2003), Conjugate strike-slip faulting
1012 along the Bangong-Nujiang suture zone accommodates coeval east-west extension and
1013 north-south shortening in the interior of the Tibetan Plateau. *Tectonics,* 22(4)*,* 1044,
1014 doi:10.1029/2002TC001361.
1015 Taylor, M., & Peltzer, G. (2006), Current slip rates on conjugate strike-slip faults in central Tibet
1016 using synthetic aperture radar interferometry. *Journal of Geophysical Research,*
1017 111(B12402). doi:10.1029/2005JB004014.
1018 Tian, Z., Yang, Z., Bendick, R., Zhao, J., Wang, S., Wu, X., & Shi, Y. (2019), Present-day
1019 distribution of deformation around the southern Tibetan Plateau revealed by geodetic and
1020 seismic observations. *Journal of Asian Earth Sciences,* 171*,* 321-333,
1021 doi:10.1016/j.jseaes.2018.12.018.
1022 Tilmann, F., Ni, J., & Team, I.I.S., (2003), Seismic imaging of the downwelling Indian lithosphere
1023 beneath central Tibet. *Science*, 300, 1424–1427.
1024 Valli, F., Arnaud, N., Leloup, P. H., Sobel, E. R., Mahéo, G., Lacassin, R., et al. (2007), Twenty
1025 million years of continuous deformation along the Karakorum fault, western Tibet: a
1026 thermochronological analysis. *Tectonics,* 26(TC4004). doi:10.1029/2005TC001913.
1027 Van Der Woerd, J., Tapponnier, P., Ryerson, F. J., Meriaux, A.S., Meyer, B., Gaudemer, Y., et al.
1028 (2002), Uniform postglacial slip-rate along the central 600 km of the Kunlun fault (Tibet),
1029 from ^{26}Al, ^{10}Be, and ^{14}C dating of riser offsets, and climatic origin of the regional
1030 morphology. *Geophysical Journal International*, 148(3), 356–388.
1031 Vergne, J., Wittlinger, G., Hui, Q.A., Tapponnier, P., Poupinet, G., Mei, J., Herquel, G., & A. Paul
1032 (2002), Seismic evidence for stepwise thickening of the crust across the NE Tibetan plateau,
1033 *Earth and Planetary Science Lettres*, 203, 25– 33, doi:10.1016/S0012-821X(02)00853-1.

1034 Wang, Q., Zhang, P. Z., Freymueller, J. T., Bilham, R., Larson, K. M., Lai, X., et al. (2001),
1035 Present-day crustal deformation in China constrained by global positioning system
1036 measurements. *Science,* 294*,* 574 – 577.
1037 Wang, H., Elliott, J. R., Craig, T. J., Wright, T. J., Liu-Zeng, J., & Hooper, A. (2014), Normal
1038 faulting sequence in the Pumqu-Xainza Rift constrained by InSAR and teleseismic body-
1039 wave seismology. *Geochemistry Geophysics Geosystems,* 15*,* doi:10.1002/2014GC005369.
1040 Wang, C., Dai, J., Zhao, X., Li, Y., Graham, S. A., He, D., et al. (2014), Outward-growth of the
1041 Tibetan Plateau during the Cenozoic: A review. *Tectonophysics*, *621*, 1–43.
1042 Wang, W., Qiao, X., Yang, S., & Wang, D. (2017), Present day velocity field and block kinematics
1043 of Tibetan Plateau from GPS measurements. *Geophysical Journal International*, 208, 1088–
1044 1102. doi:10.1093/gji/ggw445.
1045 Wang, H., Wright, T. J., Liu-Zeng, J., & Peng, L. (2019), Strain rate distribution in south-central
1046 Tibet from two decades of InSAR and GPS. *Geophysical Research Letters,* 46*.*
1047 doi:10.1029/2019GL081916.
1048 Wang, S., Chevalier, M.-L., Pan, J., Bai, M., Li, H., Li, K., & Liu, F. (2020), Late Quaternary
1049 activity of the southern Yadong-Gulu rift, southern Tibet. *in revision in Tectonophysics.*
1050 Wang, Y., Wang, P., Ge, W., Zhou, R., Schoenbohm, L. M., Zhang, B., et al. (2019), Differential
1051 crustal deformation across the Cona-Oiga rift, southern Tibetan Plateau. *Journal of Asian*
1052 *Earth Sciences,* 177*,* 177-185. doi:10.1016/j.jseaes.2019.03.023.
1053 Wernicke, B. (1985), Uniform-sense normal simple shear of the continental lithosphere. *Canadian*
1054 *Journal of Earth Sciences*, 22, 108-125.
1055 Wittlinger, G., J. Vergne, P. Tapponnier, V. Farra, G. Poupinet, M. Jiang, H. Su, G. Herquel, & A.
1056 Paul (2004), Teleseismic imaging of subducting lithosphere and Moho offsets beneath
1057 western Tibet, *Earth and Planetary Science Letters*, 221(1– 4), 117– 130.

1058 Wolff, R., Hetzel, R., Dunkl, I., Xu, Q., Bröcker, M., & Anczkiewicz, A.A. (2019), High-Angle
1059 Normal Faulting at the Tangra Yumco Graben (Southern Tibet) since ~15 Ma. *The Journal*
1060 *of Geology*, 127. doi:10.1086/700406.

1061 Wu, Z. M, Cao, Z. Q., Shentu, B. M., & Deng, Q. D. (1992), Active Fault in the Central Tibet.
1062 *Seismological Press, Beijing. pp.* 161–192. (in Chinese with English abstract).

1063 Wu, Z., Zhao, X., Wu, Z., Jiang, W., Hu, D., & Zhou, C. (2004), Quaternary geology and faulting in
1064 the Damxung-Yangbajain basin. *Acta Geologica Sinica,* 78*,* 1*,* 273-282.

1065 Wu, Z., Ye, P., Barosh, P., & Wu, Z. (2011), The October 6, 2008 Mw 6.3 magnitude Damxung
1066 earthquake, Yadong-Gulu rift,Tibet, and implications for present-day crustal deformation.
1067 *Journal of Asian Earth Sciences,* 40*,* 943-957. doi:10.1016/j.jseaes.2010.05.003.

1068 Wu, Z., Ye, P., Wang, C., Zhang, K., Zhao, H., Zheng, Y., et al. (2015), The Relics, Ages and
1069 Significance of Prehistoric Large Earthquakes in the Angang Graben in South Tibet. *Earth*
1070 *Science - Journal of China University of Geosciences*, 40 (10). doi:10.3799/dqkx.2015.147.
1071 (in Chinese with English abstract).

1072 Wu, C., Tian, X., Xu, T., Liang, X., Chen, Y., Zhu, G., et al. (2019), Upper-Crustal Anisotropy of
1073 the Conjugate Strike-Slip Fault Zone in Central Tibet Analyzed Using Local Earthquakes
1074 and Shear-Wave Splitting. *Bulletin of the Seismological Society of America.*
1075 doi:10.1785/0120180333.

1076 Yin, A., Kapp, P. A., Murphy, M. A., Harrison, T. M., Grove, M., Ding, L., et al. (1999),
1077 Significant late Neogene east-west extension in northern Tibet. *Geology,* 27, 787 – 790.

1078 Yin, A. (2000), Mode of Cenozoic east-west extension in Tibet suggests a common origin of rifts in
1079 Asia during the Indo-Asian collision. *Journal of Geophysical Research,* 105, 21,745 –
1080 21,759.

1081 Yin, A., & Taylor, M. H., (2011), Mechanics of V-shaped conjugate strike-slip faults and the

corresponding continuum mode of continental deformation. *Geological Society of America Bulletin*, 123, 9/10, 1798–1821. doi:10.1130/B30159.1.

Zechar, J.D., & Frankel, K. L. (2009), Incorporating and reporting uncertainties in fault slip rates. *Journal of Geophysical Research,* 114(B12407). Doi:10.1029/2009JB006325.

Zhang, P. Z., Shen, Z., Wang, M., Gan, W. J., Burgmann, R., & Molnar, P. (2004), Continuous deformation of the Tibetan Plateau from global positioning system data. *Geology,* 32*,* 809-812.

Zheng, G., Wang, H.,Wright, T. J., Lou, Y., Zhang, R., Zhang,W., et al. (2017), Crustal deformation in the India-Eurasia collision zone from 25-years of GPS measurements. *Journal of Geophysical Research,* 122*,* 9290–9312. doi:10.1002/2017JB014465.

Zhu, G. H., X. F. Liang, X. B. Tian, H. F. Yang, C. L.Wu, Y. H. Duan, et al. (2017), Analysis of the seismicity in central Tibet based on the SANDWICH network and its tectonic implications. *Tectonophysics,* 702, 1–7, doi: 10.1016/j.tecto.2017.02.020.

Figure captions

Figure 1: *Southern Tibet normal faults and Yadong-Gulu rift in the frame of the India – Asia collision zone (modified from Tapponnier et al., 2001). (**a**) Tectonic map of southern Tibet with digital elevation model (DEM) in the background (location shown in inset), with active faults, main cities/towns and lakes, historical and recorded earthquakes of M>6 (from the U.S. Geological Survey), and horizontal GPS velocities relative to stable Eurasia (Zheng et al., 2017). The most prominent rift, that of Yadong-Gulu (YGR) is located in the far right (box **b**). The other main rifts are COR = Cona-Oiga rift, PXR = Pumqu-Xainza rift, ADR = Ama Drime rift (or Dinggye), TYR = Tangra Yum Co rift, KCR = Kung Co rift, LKR = Lopu Kangri rift, TKG= Thakkhola rift, LGR= Lunggar rift, GMR = Gurla Mandhata rift (or Pulan). RPCF = Riganpei Co fault, WNFS = Western Nepal fault system, GCF = Gyaring Co fault, BCF = Beng Co fault, BNS = Bangong-Nujiang suture, YZS=Yarlung Zangbo suture, SF = Sagaing fault, RRF = Red River fault, KJFZ = Karakorum-Jiali fault zone. (**b**) Close-up of the northern half of the YGR, from the YZS to the Beng*

*Co fault, with main cities, earthquakes (from the U.S. Geological Survey) and focal mechanisms of instrumental earthquakes of Mw>5 (CMT catalogue 1976-2016), and study sites (blue stars). The 1411 M8.0? historical earthquake is from Wu et al. (1992). Location of Figures 2 and 3 is indicated. (**c**) Topographic profiles at various locations perpendicular to the rift, with traces of main active faults.*

Figure 2: *Google Earth image of the northernmost Yadong-Gulu rift. (**a**) The Gulu half-graben and Damxung corridor along the Nyainqentanghla Range. Note the left-lateral component of motion on NE to EW-striking faults (black arrows). Yellow polygons represent sites discussed in Armijo et al. (1986) and green stars refer to the sites studied here (T = terrace, M = moraine) with associated figure numbers. (**b-e**) Close-up of areas (locations in **a**) showing clear left-lateral motion, where horizontal offsets of rivers, moraine edges, and other morphologic markers, are highlighted by white/black dashed lines and approximate offset values are indicated. Colored triangles show fault traces. Damxung T site is presented in more details in Figures 11-13. PA = pull-apart.*

Figure 3: *Google Earth image of the central Yadong-Gulu rift: the Damxung corridor, Yangbajing and Angang grabens. Yellow polygons represent sites discussed in Armijo et al. (1986) and green stars refer to the sites studied here (T = terrace, M = moraine) with associated figure numbers. Note the ~4 km horizontal offset of the western edge of the Yangbajing graben and Nyainqentanghla Range, as described in Armijo et al. (1986). Dong et al. (2017)'s study is located 5 km west of the map.*

Figure 4: *The Gulu moraine site. (**a**) Bing satellite image of the Gulu moraine site and (**b**) its interpretation. The ~400 m wide normal fault zone here is made of numerous fault segments in red, dipping in opposite directions. Samples collected upstream (Gulu W) and downstream (Gulu E) from the fault are shown by white circles with corresponding sample numbers. Location of photos from Figure 5 is also indicated. (**c**) Bird's eye view toward the WNW, taken from a drone (Unmanned Aerial Vehicle) of the entire site with cars circled for scale. Black lines with white polygonal tips show the intersection between the shallow-dipping detachment fault and surface topography, while those with green polygonal tips show roughly parallel shallow-dipping triangular facets (~10-20°) on the bedrock footwall farther upstream in the valley. See text for details.*

Figure 5: *Field photos of the Gulu moraine site. (**a**) Numerous normal fault scarps facing opposite directions (forming small depressions) transversally cut the Gulu moraine. (**b**) View from upstream, where the Gulu half-graben floor is visible, as well as the terraces (T) present along the river. Cars circled for scale. Faults highlighted by red arrows. Close-up in **f**. (**c,d**) Fault scarps. (**e**) Numerous fault scarps highlighted by shadow and red arrows. Photo locations shown in Figure 4.*

Figure 6: *LiDAR Digital Elevation Model (DEM) of the Gulu moraine site (**a**) with profiles across the fault zone showing the total subsidence of the moraine at 40±4 m (**b**). (**c**) 1:1 profile with fault geometry at depth, with a measured 18°-dipping detachment fault (green) into which shallow faults root (red) (Wernicke, 1985). See text for details.*

Figure 7: *^{10}Be cosmogenic surface-exposure ages of the Gulu M and Ybj M sites (moraines), using the Lal (1991)/Stone (2000) time-dependent model with 1-σ uncertainty. Oldest age (circled) of each moraine is shown with value displayed in the box, representing the minimum moraine abandonment age. Numbers next to samples refer to sample names in Table 1.*

Figure 8: *The Gulu terrace site. (**a**) Bing satellite image of the Gulu terrace site and (**b**) its interpretation. One main cumulative normal fault scarp cuts and vertically offsets the Gulu terrace/fan. Ruptures from the 1952 Gulu earthquake are visible in the footwall. Samples collected upstream (Tup) and downstream (Tdown) from the fault are shown by white circles with corresponding sample names. (**c,d**) Field photos of the main cumulative fault scarp. (**e**) View from Tup with people circled for scale. Note the rockfall on Tup, forcing us to sample near the terrace riser above the river to avoid possible contamination. (**f**) Bird's eye view of the entire site taken from a drone. This photo was taken >10 years after photos in c-e, hence differences such as the larger extent of the village in the hanging wall as well as the presence of prayer flags where we sampled on Tup. Thin red lines show the surface ruptures from the 1952 earthquake.*

Figure 9: *LiDAR DEM of the Gulu terrace site (**a**) with profiles across the fault zone showing the total vertical offset, averaging at 25±2 m (**b,c**).*

Figure 10: *^{10}Be and ^{26}Al cosmogenic surface-exposure ages of the Gulu T, Damxung T, and Gyekar T sites (terraces), using the Lal (1991)/Stone (2000) time-dependent model with 1-σ uncertainty. Outliers in white are discarded (using Peirce criterion) when calculating the average age of the*

*surface (indicated under the site names and shown by grey boxes). Some outliers (marked with a * symbol) require specific discussion, see text for details. Numbers next to samples refer to sample names in Table 2. Note the zoom in ages at Damxung T1 and T2 with the change of scale. To the right, the global climatic proxy curve of Lisiecki and Raymo (2005) shows the Marine oxygen Isotope Stages (MIS) 1 to 11.*

***Figure 11:** The Damxung terrace site. (**a**) Google Earth image of the Damxung terraces site and (**b**) its interpretation. Here, two parallel normal-sinistral faults F1 and F2 cut the terraces. Collected samples are shown by white circles with corresponding sample names on T1 (lower terrace) and T2 (upper terrace). Location of Figure 11d and photos from Figure 12 are also indicated. (**c**) Cartoon modified from Armijo et al. (1986) showing how slip is partitioned between normal and left-lateral motion along both parallel faults at this site. (**d**) Horizontal offset by F2 of the western edge of T1 (17±5 m), as measured by back-slipping the LiDAR DEM and the contour lines. Location of **d** shown in **b**.*

***Figure 12:** Field photos of the Damxung terrace site. (**a**) View from T2 (upper terrace) looking at T1 (lower terrace) and the two parallel faults F1 and F2. (**b**) View of F2 and its fault scarp on T1 (highlighted by red arrows), along which two large pull-aparts developed. (**c,d**) Pull-apart on T1 along F2. Cars and people circled for scale. Photo locations shown in Figure 11.*

***Figure 13:** LiDAR DEM of the Damxung terrace site (**a**). (**b**) Profiles P6 and P7 across the faults (note the two different scales) showing the total vertical offset of T2, averaging at 184±3 m. (**c**) Profiles P3-P5 and (**d**) P1-P2 across T1, averaging at 10±2 m. Faults F1 and F2 highlighted by red arrows in **a**.*

***Figure 14:** The Yangbajing moraine site. (**a**) Bing satellite image of the Yangbajing moraine site and (**b**) its interpretation. One main fault cuts and vertically offsets the moraine crest. Samples collected upstream (Ybj W and N) and downstream (Ybj E) from the fault are shown by white circles with corresponding sample names. (**c-e**) Field photos showing the fault scarp and offset moraine crest (forming triangular facets). (**f**) View from upstream of the moraine crest and its large granite boulders. (**g**) View looking south, where the fault scarp and rupture is visible for ~10 km, possibly a relict of the nearby 1411 M8 (?) earthquake.*

Figure 15: *LiDAR DEM of the Yangbajing moraine site (**a**) with profiles across the fault showing the total vertical offset of 44±1 m (**b**). Faults F1 and F2 highlighted by red arrows in **a**.*

Figure 16: *The Gyekar terraces site. (**a**) Google Earth image of the Gyekar terraces site and (**b**) its interpretation. Numerous parallel faults cut and vertically offset the fans/terraces. Faults in black may not be active at present. Collected samples from T1 and T2 are shown by white circles with corresponding sample names. Location of photos from Figure 17 is indicated. (**c**) LiDAR DEM with contour lines (location in **b**).*

Figure 17: *Field photos of Gyekar terraces site. (**a,b**) Panoramic views of the flight of terraces with fault trace at mid-slope on the scarps. (**c,i**) Hot springs from the western side of the southern Yangbajing graben located across from the Gyekar terraces (location in Figure 3). (**d,e**) Photos showing the difference between the fault scarp at the base of T2, which is more diffused, covered with short grass, and with deeply entrenched gullies (**d**), and that at the base of T1, which is steeper, covered by less vegetation, and shallower gullies (**e**). Red arrows show fault trace. (**f,g**) Fault planes clearly exposed in gullies across T1/T0 and T2/T1 scarps, on which we precisely measured the fault dips. (**h**) Photo of the strath terrace below T2 and T3. Photo locations shown in Figure 16.*

Figure 18: *LiDAR DEM of the Gyekar terraces site (**a**). (**b**) Profiles across the faults show the 87±5 m vertical offset across the T2/T1 scarp and that of 15±3 m across the T1/T0 scarp. Note the scale differences between the three sets of profiles. Faults F1 and F2 highlighted by red arrows in **a**.*

Figure 19: *Summary of throw/extension rates along the Yadong-Gulu rift (YGR). See Table 3 for references to numbers. (**a**) Throw – vertical (black) / Extension - horizontal (green) rates at various timescales. (**b**) Extension rates along strike, rather constant south of the Gulu bend at 1.3±0.3 mm/yr, and rapidly increasing north of it, most likely do to the transfer of slip from the dextral Beng Co fault.*

Figure 20: *Slopes map (from Fielding et al., 1994) highlighting different topographic and geomorphic regions on the Tibetan Plateau (Liu-Zeng et al., 2008). Pink and blue patches*

correspond to distinct normal faulting areas north and south of the Bangong-Nujiang suture (BNS). Oblique white dashed line is the "chord" joining Nanga Parbat (NP) and Namche Barwa (NB) at both Himalayan syntaxes (after Armijo et al., 1986).

Table 1: ^{10}Be surface-exposure dating of the moraine samples.

Table 2: ^{10}Be and ^{26}Al surface-exposure dating of the alluvial samples.

Table 3 : Rates summary along the Yadong-Gulu rift.

Table 1: ^{10}Be surface-exposure dating of the moraine samples.

	Sample name	Lat (°N)	Long (°E)	Elev.	Shielding	10Be (at/g)	err	Published age †	Recalculated age ††
Gulu W	T5C-58	30.81139	91.55621	5003	0.9916	1227679	24480	15486±1346	16982±1618
	T5C-59	30.81126	91.55642	5003	0.9916	1252031	24832	15768±1371	17292±1647
	T5C-60	30.81102	91.55689	4995	0.9951	1297396	23586	16292±1410	17870±1696
	T5C-61	30.81096	91.55738	4988	0.9951	1210116	25074	15328±1335	16809±1604
	T5C-62	30.81083	91.55754	4991	0.9951	1298660	37725	16333±1462	17916±1749
	T5C-63	30.81083	91.55754	4991	0.9951	1358947	34231	17026±1504	18689±1804
	T5C-64	30.81062	91.55782	4987	0.9947	1393854	35889	17464±1546	19176±1854
Gulu E	T5C-66	30.80783	91.56484	4932	0.9971	1584591	40335	20590±1822	22044±2132
	T5C-67	30.80783	91.56484	4932	0.9971	1364351	34705	17910±1584	19195±1855
	T5C-68	30.80751	91.56579	4958	0.9971	1320837	35843	17499±1556	18421±1788
	T5C-69	30.80732	91.56593	4916	0.9971	1294481	32762	17308±153	18401±1777
	T5C-70	30.80798	91.56578	4914	0.9971	1300262	40576	17233±1556	18493±1818
	T5C-71	30.80849	91.56405	4876	0.9962	1512634	47528	19717±1782	21643±2131
	T5C-72	30.80851	91.56379	4869	0.9962	1219567	30955	16203±1432	17774±1716
	T5C-73	30.8077	91.56486	4855	0.9962	1273776	31228	16960±1495	18618±1794
Ybj W	T5C-25	30.02181	90.24252	5276	0.9826	2881748	52627	31104±2703	34012±3242
	T5C-26	30.02171	90.24297	5258	0.9826	2344650	42993	26094±2265	28509±2714
	T5C-27**	30.0214	90.24315	5248	0.9826	1912313	37191	21797±1896	23827±2271
	T5C-28	30.02133	90.24332	5227	0.9868	2711638	70371	29907±2657	32714±3176
	T5C-29	30.02113	90.24345	5221	0.99	3202175	74603	3466±3057	37563±3625
	T5C-30#	30.02091	90.24372	5206	0.99	4812903	103646	49757±4383	56086±5415
	T5C-31	30.02077	90.24406	5200	0.99	1587965	30984	18585±1615	20405±1943
	T5C-32	30.02077	90.24406	5200	0.99	1457076	26595	17165±1487	18838±1789
	T5C-33	30.02065	90.24432	5184	0.99	2289852	41982	26123±2268	28540±2717
	T5C-34	30.02053	90.24472	5177	0.99	2987774	53120	33168±2881	36135±3443
Ybj E	T5C-35	30.0185	90.24805	5034	0.99	1485256	26941	18698±1620	20532±1950
	T5C-36	30.01823	90.24807	5033	0.99	3903265	83862	43556±3830	47998±4624
	T5C-37	30.01804	90.24783	5066	0.9926	3624150	64791	40331±3510	43889±4191
	T5C-38	30.01801	90.24822	5026	0.9926	4350087	75134	48461±4220	54501±5212
	T5C-39 §	30.01802	90.24849	5021	0.9926	3081077	54984	36056±3134	38991±3718
	T5C-40**	30.01801	90.24865	5014	0.9926	3504063	66012	39996±3489	43459±4157
	T5C-41	30.0181	90.24931	5010	0.9926	3719922	65182	42047±3658	46053±4397
	T5C-42 §	30.01796	90.24933	4999	0.9926	4321103	80325	48748±4259	54862±5260
	T5C-43 §	30.01784	90.24949	4991	0.99	2163193	31645	26808±2309	29272±2768
	T5C-44	30.01782	90.2495	4982	0.9868	4112110	108452	46921±4193	52539±5132
Ybj N	T5C-44bis	30.02351	90.24524	5239	0.9868	2105096	113008	23740±2386	26013±2805
	T5C-45	30.02402	90.24464	5261	0.9868	1073159	32747	12597±1133	13899±1362
Ybj inner	T5C-19**	30.02319	90.24192	5305	0.99	947690	26149	10874±967	12028±1167
	T5C-20	30.02313	90.24197	5302	0.99	1135106	23814	13044±1137	14368±1371
	T5C-21	30.02313	90.24197	5302	0.99	904934	18644	10401±905	11492±1095
	T5C-22*	30.02308	90.24198	5295	0.99	1821423	32544	20316±1759	22256±2114
	T5C-23	30.02298	90.24185	5287	0.99	1248601	25589	14384±1252	15786±1505

† Ages published in Chevalier et al. (2011).

†† Ages recalculated with the CRONUS 2.3 calculator using the Lal (1991)/Stone (2000) time-dependent production rate model.

^{10}Be production rate is 4.1 at/g/a. All samples were processed at Stanford University's cosmogenic facility.

§ The ^{10}Be/^{9}Be ratios were measured at the Lawrence Livermore National Laboratory: 07KNSTD with ^{10}Be isotope ratios=2.79x1e-11.

For all other samples, the ^{10}Be/^{9}Be ratios were measured at CEREGE: NIST SRM4325 (=NIST_27900), equivalent to 07KNSTD.

* Outlier rejected using Peirce's criterion (following Blomdin et al., 2016).

**Sample was quartzite, all others were granite.

No erosion rate was applied. Thickness is 4 cm. Density is 2.7 g/cm3 for granite and 2.65 g/cm3 for quartzite.

Table 2: ^{10}Be and ^{26}Al surface-exposure dating of the alluvial samples.

	Sample name	Lat (°N)	Long (°E)	Elev.	Shielding	^{10}Be (at/g)	err	^{26}Al (at/g)	err	^{10}Be age (yrs) †	err	^{26}Al age (yrs) †	err	^{26}Al/^{10}Be conc.
Gulu T up	T5C-75	30.67214	91.52428	4651	1	182971	6962	985830	67901	3286	330	2708	313	5.38
	T5C-78	30.67229	91.52379	4645	1	928065	32828	5121162	186501	15318	1526	12915	1295	5.51
	T5C-82	30.67217	91.52429	4651	1	254688	12780	1156740	189886	4434	468	3152	595	4.54
Gulu T down	T5C-85	30.67107	91.52791	4593	1	3663368	133994	19139157	715710	55054	5564	43256	4418	5.22
	T5C-91	30.67091	91.52925	4580	1	24917297	588827	137802787	3098854	403083	42733	359743	41179	5.53
Damxung T1	T5C-102	30.52696	91.09392	4396	0.995952	969086	33817	5867556	204247	17919	1783	16563	1654	6.05
	T5C-107	30.52551	91.09152	4393	0.995952	1033288	32425	6930002	230822	19050	1874	19360	1926	6.7
	T5C-108	30.52447	91.09214	4393	0.995952	1010218	34178	6752400	199795	18653	1850	18896	1856	6.68
	T5C-109b	30.52353	91.09292	4382	0.995952	952869	44289	6361787	190541	17755	1850	17960	1766	6.67
	T5C-110	30.52114	91.09366	4362	0.998147	1131165	34136	7373984	213983	20975	2056	20768	2039	6.51
	T5C-114	30.5209	91.09295	4370	0.998147	976630	35198	6203038	197268	18227	1822	17605	1741	6.35
Damxung T2	T5C-92	30.53208	91.09345	4556	0.998722	241631	12548	1488708	67609	4427	471	4148	429	6.16
	T5C-93b	30.53286	91.09393	4562	0.998722	971983	33116	2718304	681725	16656	1652	7121	1911	2.79
	T5C-97	30.53232	91.09521	4558	0.998722	15986946	583503	81966276	1226356	250186	26558	198780	20621	5.12
	T5C-101	30.53143	91.0972	4544	0.998722	20312794	738851	110748873	1720803	325189	35173	283536	30745	5.45
Gyekar T1	T5C-6	29.87901	90.37154	4435	1	10680049	379397	60015261	2143509	177988	18485	154808	16616	5.61
	T5C-9	29.87833	90.37074	4432	1	4085222	136379	25052419	1171782	68080	6825	64254	6889	6.13
Gyekar T2	T5C-14	29.8542	90.37619	4541	1	17211893	395395	77981065	3037209	277099	28393	193360	21419	4.53
	T5C-17	29.85402	90.3761	4543	1	13825128	464127	16233863	879683	217521	22662	39118	4283	1.17
	T5C-50	29.86142	90.37923	4541	1	15711102	349727	79143796	2784025	251826	25592	196184	21460	5.03
	T5C-56	29.86166	90.37934	4540	1	6175938	191963	4992451	407129	97734	9796	13552	1685	0.8

† Ages from Kali (2010) recalculated with the CRONUS v2.3 calculator using the Lal (1991)/Stone (2000) time-dependent production rate model. ^{10}Be production rate is 4.1 at/g/a.
Samples were processed at the Institut de Physique du Globe de Strasbourg, France and ratios were measured at CEREGE: NIST SRM4325 (=NIST_27900), equivalent to 07KNSTD with ^{10}Be isotope ratios=2.79x1e-11; SMAL11 for 26Al isotope ratios = 7.401x1e-12.
No erosion rate was applied. Density is 2.65 g/cm3 (all samples are quartzite cobbles). Thickness is 5 cm.

Table 3 : Rates summary along the Yadong-Gulu rift

	Fault dip (°)	Rate (mm/yr)		Reference	Method	Ref.
		Throw	Extension			in Fig. 19
Geodetic						
Yadong-Gulu rift			4.5±0.5	Wang et al., 2019	InSAR and GPS data	1
			~6	Chen et al., 2004a,b	GPS, block model	2
			5.2±0.4	Wang et al., 2017	GPS, block model	3
			2.0±0.6	Gan et al., 2007	GPS, dislocation model	4
Northern half			5.6±0.8	Tian et al., 2019	GPS, microplate model	5
Late Quaternary						
Gulu Moraine	18±5	1.8±0.3	6.0±1.8	**This study**	^{10}Be	GM
Gulu Terrace	60-70	6.4(+1.7/-1.1)	3.1±0.6	**This study**	^{10}Be	GuT
Damxung Terrace	70	0.5 – 0.75±0.2	<1.6	**This study**	^{10}Be + dip 70°(two faults)	DT
Yangbajing Moraines	41	0.8±0.1	0.9±0.1	**This study**	^{10}Be	YM
Gyekar Terraces	55-65	0.6±0.2	0.3±0.1	**This study**	^{10}Be	GyT
Yangbajing graben			1.2±0.2	**This study, YM + GyT**	^{10}Be	YM+GyT
		~1.6		Armijo et al., 1986	100 m since 60 ka (inferred ages)	6a
		1.4±0.6	1.3±0.7*	Wu et al., 2004 (Holocene)	OSL, ESR and U-series	7a
		1.1±0.3	0.9±0.5*	Wu et al., 2004 (Quaternary)	OSL, ESR and U-series	7b
Angang graben		0.8-1.3	0.9±0.4*	Wu et al., 2015	OSL and ^{14}C	8
Yadong rift		0.7±0.1	0.6±0.1#	Ha et al., 2019	OSL	9
	50	0.9±0.3	0.8±0.3	Wang et al., 2020	^{10}Be	10
Geologic						
Yadong-Gulu rift	45-60	1.9±0.6	1.4±0.8	Armijo et al., 1986	3-5 km since 2.0±0.5 Ma	6b

*We calculated an EW extension rate using a 45° - 60° dip angle

#We calculated an EW extension rate using a 50° dip angle

OSL = Optically Stimulated Luminescence

ESR = Electron Spin Resonance

Figure 1.

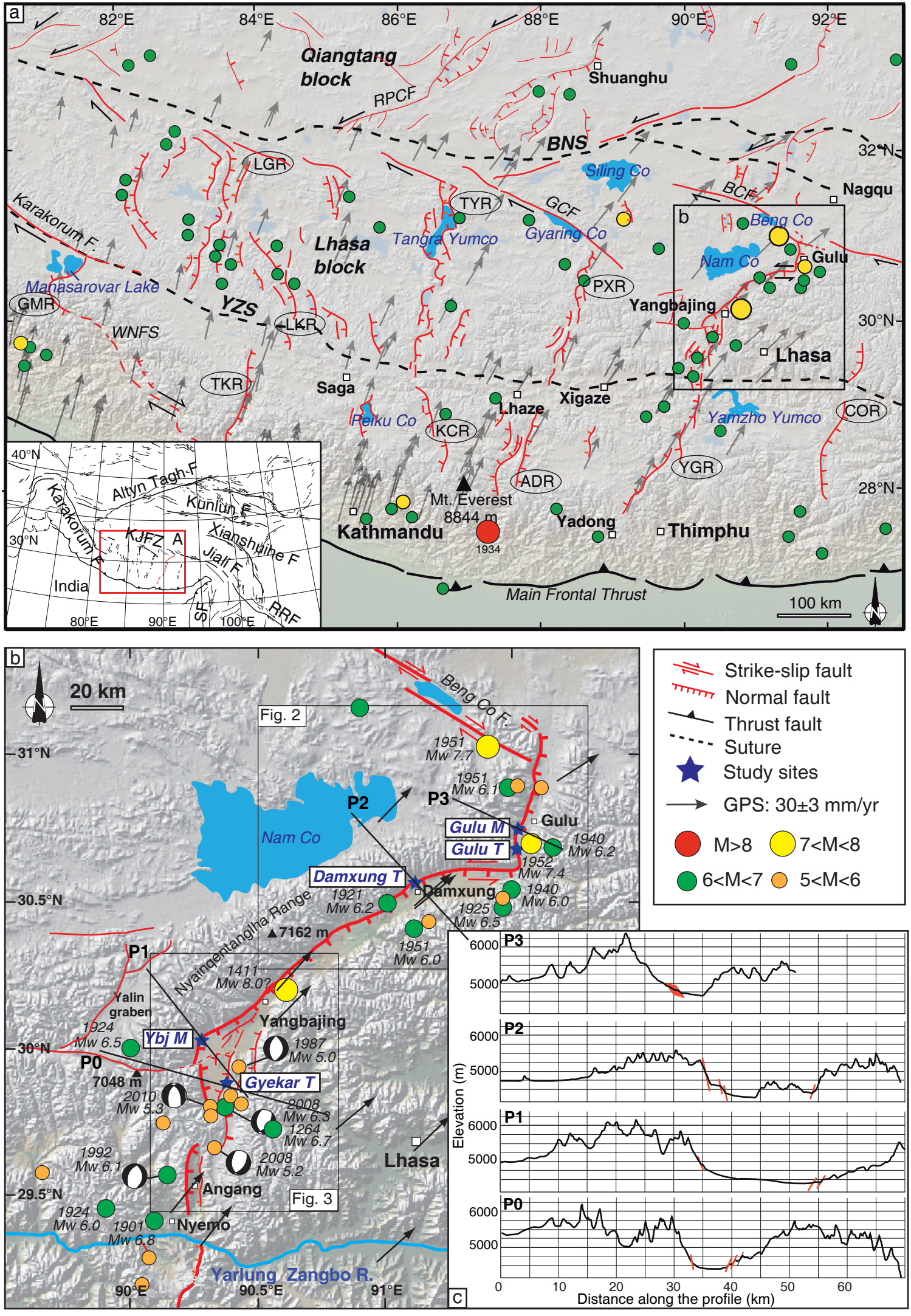
a
82°E
84°E
86°E
88°E
90°E
92°E
Qiangtang block
RPCF
Shuanghu
BNS
32°N
LGR
Siling Co
BCF
Nagqu
TYR
GCF
b
Beng Co
Tangra Yumco
Gyaring Co
Karakorum F.
Lhasa block
Nam Co
Gulu
Manasarovar Lake
GMR
YZS
PXR
Yangbajing
30°N
WNFS
LKR
Lhasa
TKR
Saga
Xigaze
Lhaze
Peiku Co
KCR
Yamzho Yumco
COR
YGR
ADR
28°N
Mt. Everest
8844 m
1934
Kathmandu
Yadong
Thimphu
Main Frontal Thrust
100 km
40°N
Altyn Tagh F
Kunlun F
Karakorum F
30°N
KJFZ
A
Xianshuihe F
Jiali F
India
80°E
90°E
100°E
RRF
b
20 km
Fig. 2
Beng Co F.
1951 Mw 7.7
1951 Mw 6.1
31°N
P2
P3
Nam Co
Gulu M
Gulu T
Gulu
1940 Mw 6.2
1952 Mw 7.4
Damxung T
1921 Mw 6.2
Damxung
1940 Mw 6.0
1925 Mw 6.5
30.5°N
Nyainqentanglha Range
▲7162 m
1951 Mw 6.0
P1
1411 Mw 8.0?
Yalin graben
1924 Mw 6.5
Yangbajing
Ybj M
1987 Mw 5.0
30°N
P0
7048 m
Gyekar T
2010 Mw 5.3
2008 Mw 6.3
1264 Mw 6.7
1992 Mw 6.1
2008 Mw 5.2
Lhasa
Angang
29.5°N
Fig. 3
1924 Mw 6.0
1901 Mw 6.8
Nyemo
Yarlung Zangbo R.
90°E
90.5°E
91°E
Strike-slip fault
Normal fault
Thrust fault
Suture
Study sites
GPS: 30±3 mm/yr
M>8
7<M<8
6<M<7
5<M<6
P3
P2
P1
P0
6000
5000
Elevation (m)
0
10
20
30
40
50
60
Distance along the profile (km)
c

Figure 2.

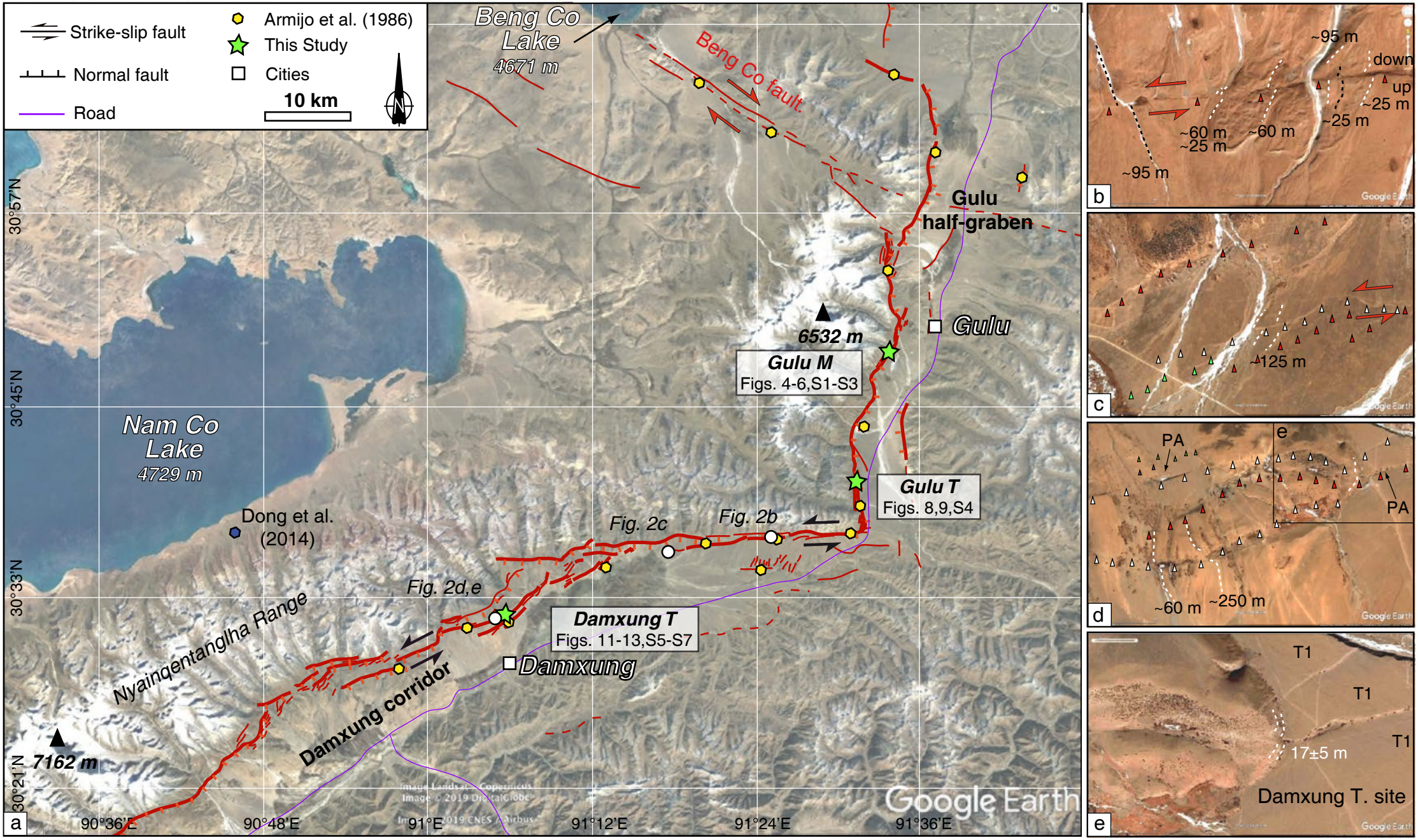
Strike-slip fault
Normal fault
Road
Armijo et al. (1986)
This Study
Cities
10 km
Beng Co Lake
4671 m
Beng Co fault
Gulu half-graben
Gulu
6532 m
Gulu M
Figs. 4-6,S1-S3
Gulu T
Figs. 8,9,S4
Nam Co Lake
4729 m
Dong et al. (2014)
Fig. 2c
Fig. 2b
Fig. 2d,e
Damxung T
Figs. 11-13,S5-S7
Damxung
Nyainqentanglha Range
Damxung corridor
7162 m
30°57'N
30°45'N
30°33'N
30°21'N
90°36'E
90°48'E
91°E
91°12'E
91°24'E
91°36'E
Google Earth
a
~95 m
down
up
~25 m
~60 m
~60 m
~25 m
~25 m
~95 m
b
~125 m
c
PA
e
PA
~60 m
~250 m
d
T1
T1
T1
17±5 m
Damxung T. site
e

Figure 3.

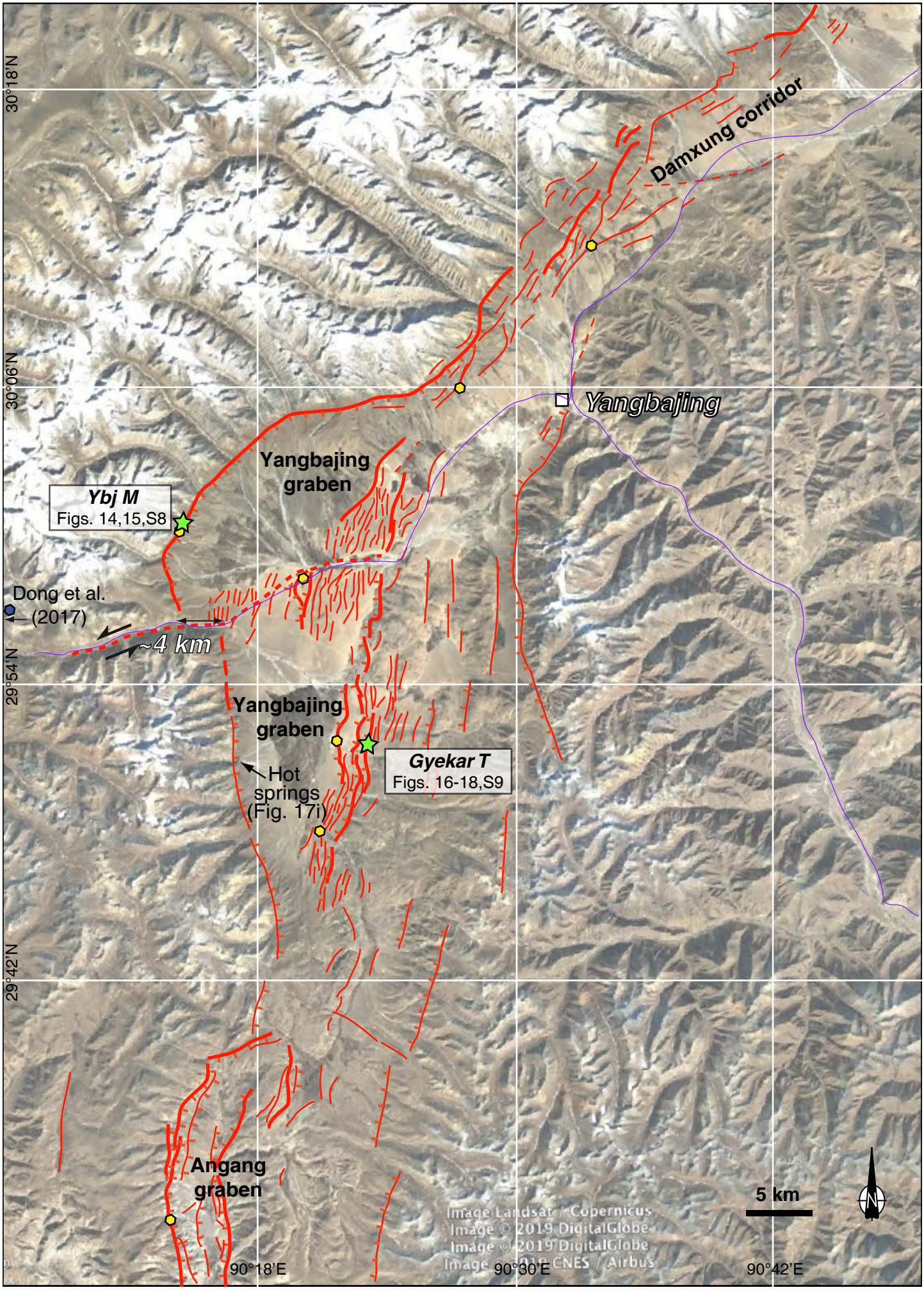
30°18'N
30°06'N
29°54'N
29°42'N
90°18'E
90°30'E
90°42'E
Damxung corridor
Yangbajing
Yangbajing graben
Ybj M
Figs. 14,15,S8
Dong et al. (2017)
~4 km
Yangbajing graben
Gyekar T
Figs. 16-18,S9
Hot springs (Fig. 17i)
Angang graben
5 km
N
Image Landsat / Copernicus
Image © 2019 DigitalGlobe
Image © 2019 DigitalGlobe
Image © 2019 CNES / Airbus

Figure 4.

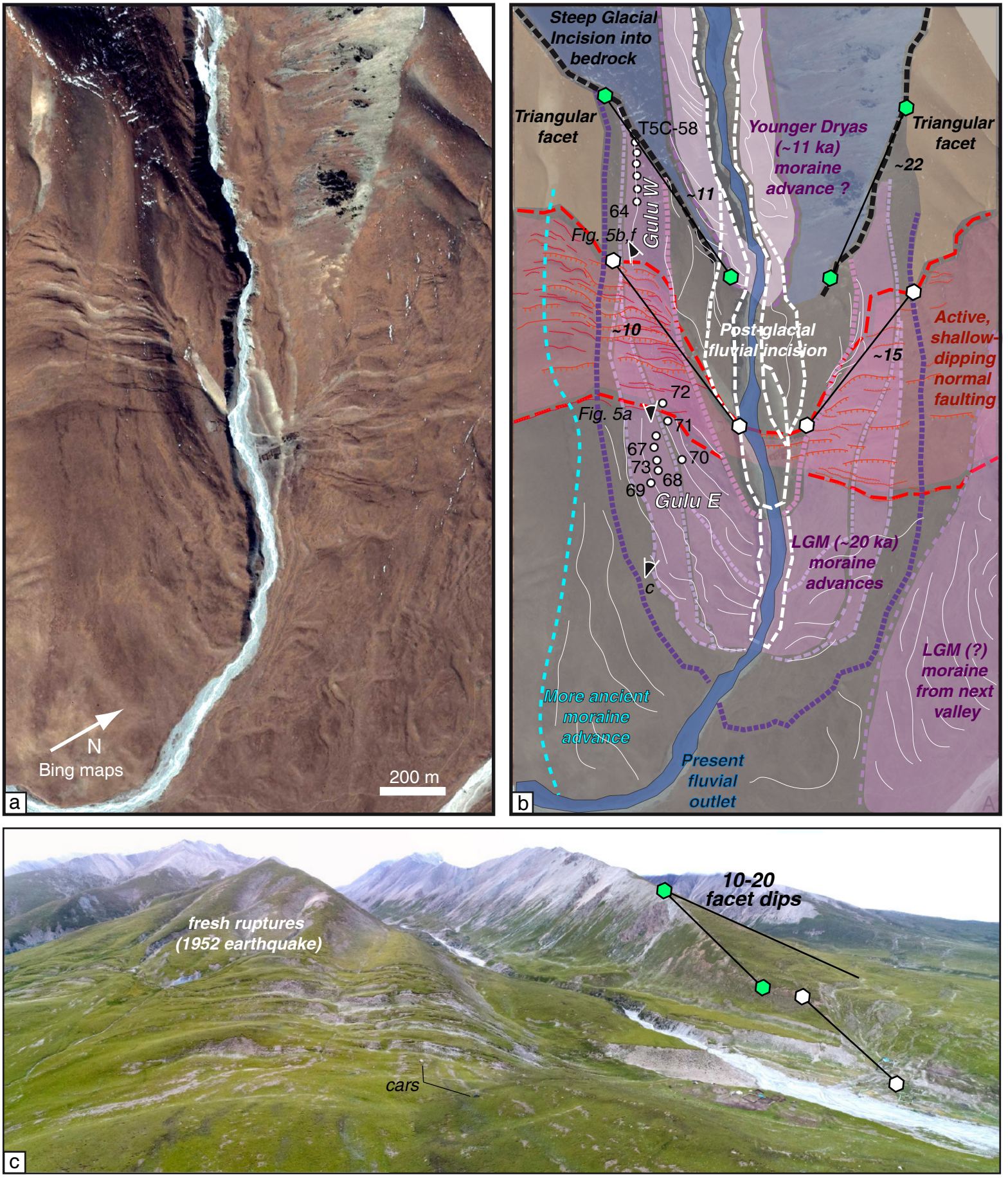
a
N
Bing maps
200 m
b
Steep Glacial Incision into bedrock
Triangular facet
T5C-58
Younger Dryas (~11 ka) moraine advance ?
Triangular facet
~22
~11
64
Gulu W
Fig. 5b,f
~10
Post-glacial fluvial incision
~15
Active, shallow-dipping normal faulting
72
Fig. 5a
71
67
70
73
68
69
Gulu E
c
LGM (~20 ka) moraine advances
LGM (?) moraine from next valley
More ancient moraine advance
Present fluvial outlet
c
fresh ruptures (1952 earthquake)
10-20 facet dips
cars

Figure 5.

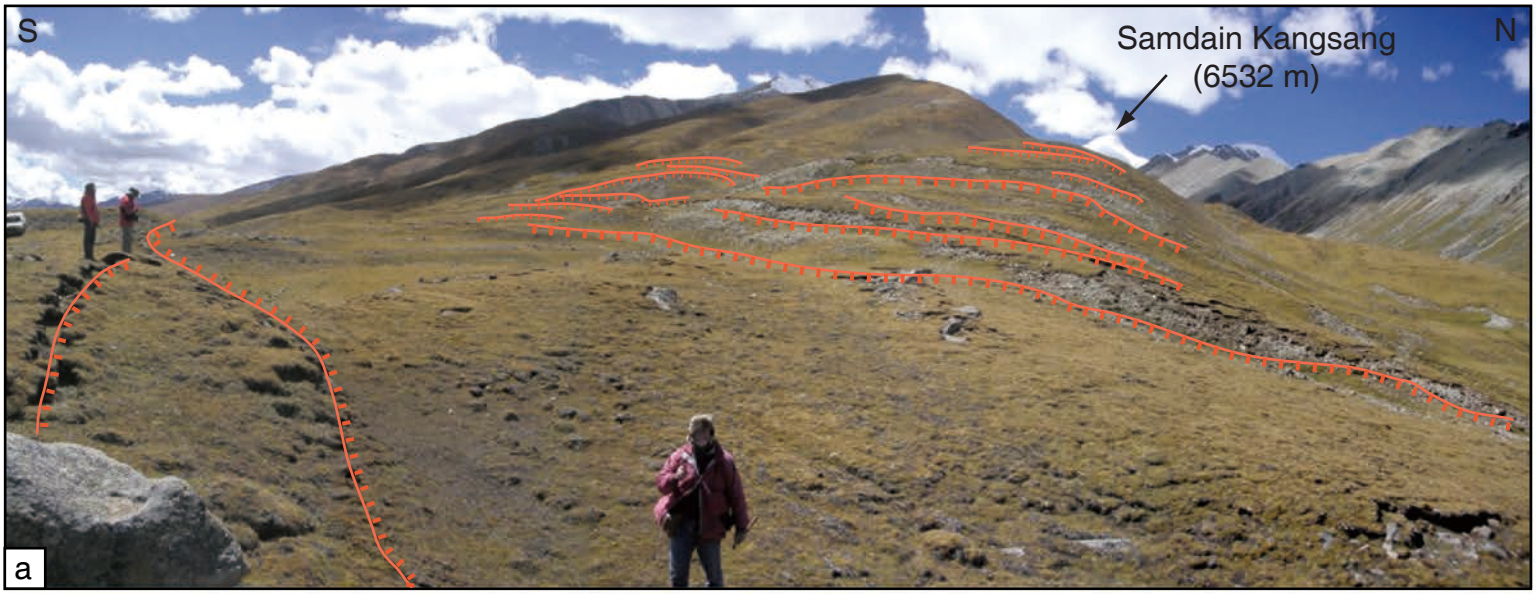
S
Samdain Kangsang
(6532 m)
N
a

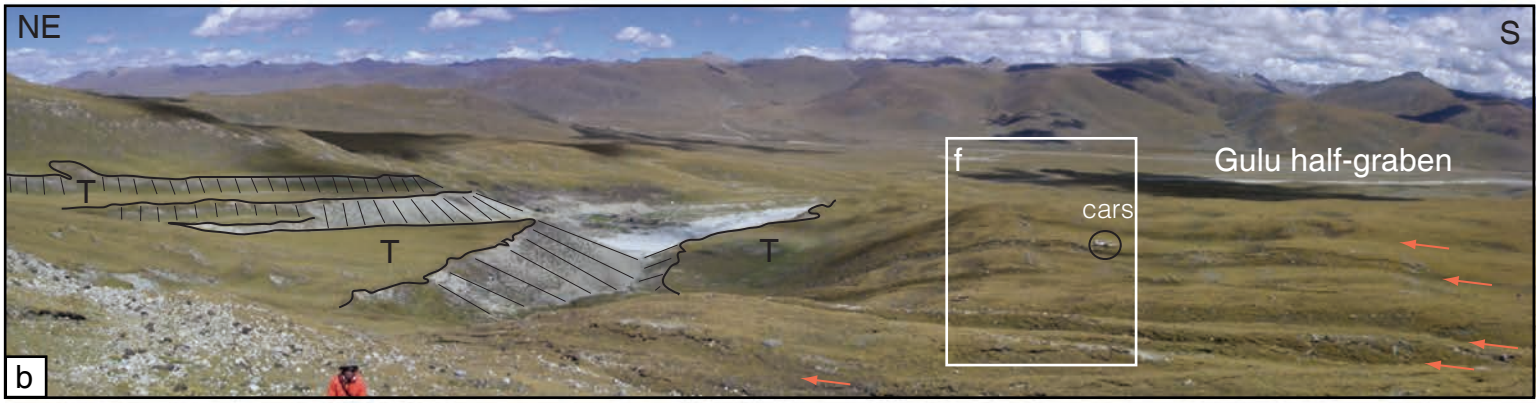
NE
S
T
T
T
f
cars
Gulu half-graben
b

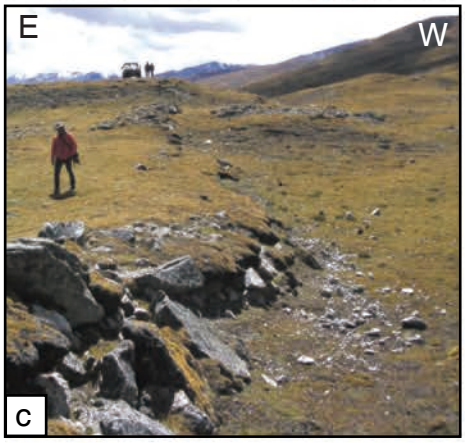
E
W
c

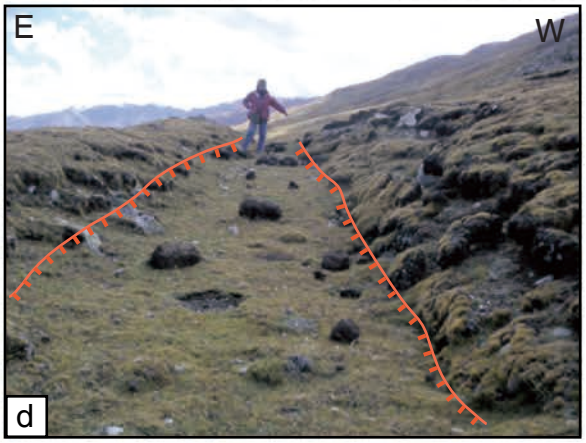
E
W
d

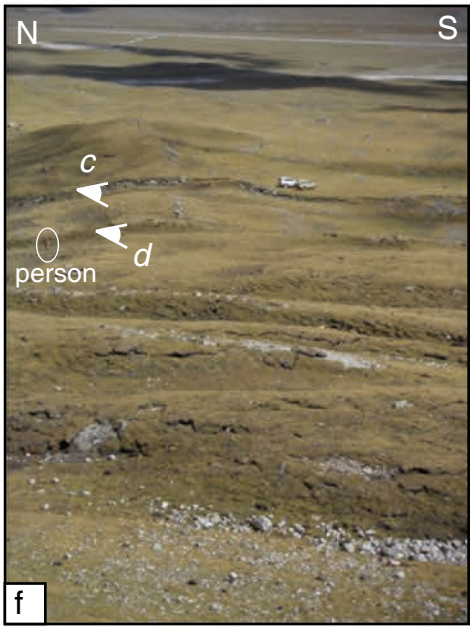
N
S
c
d
person
f

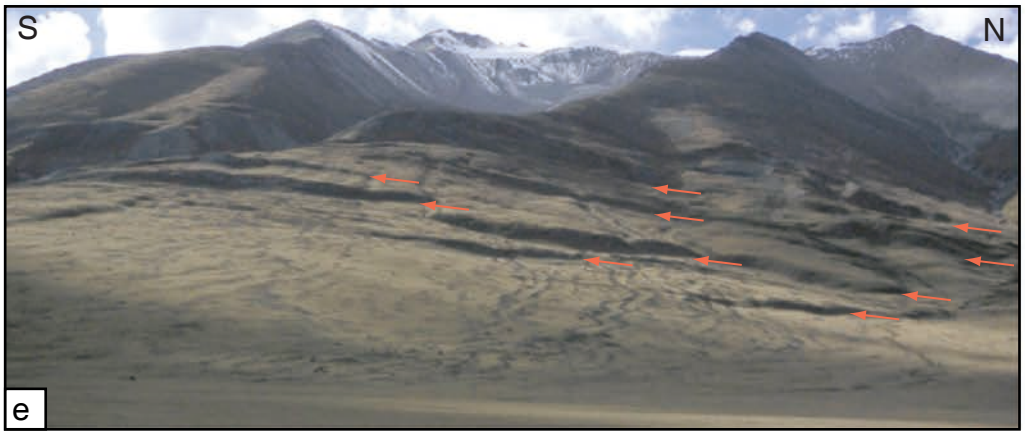
S
N
e

Figure 6.

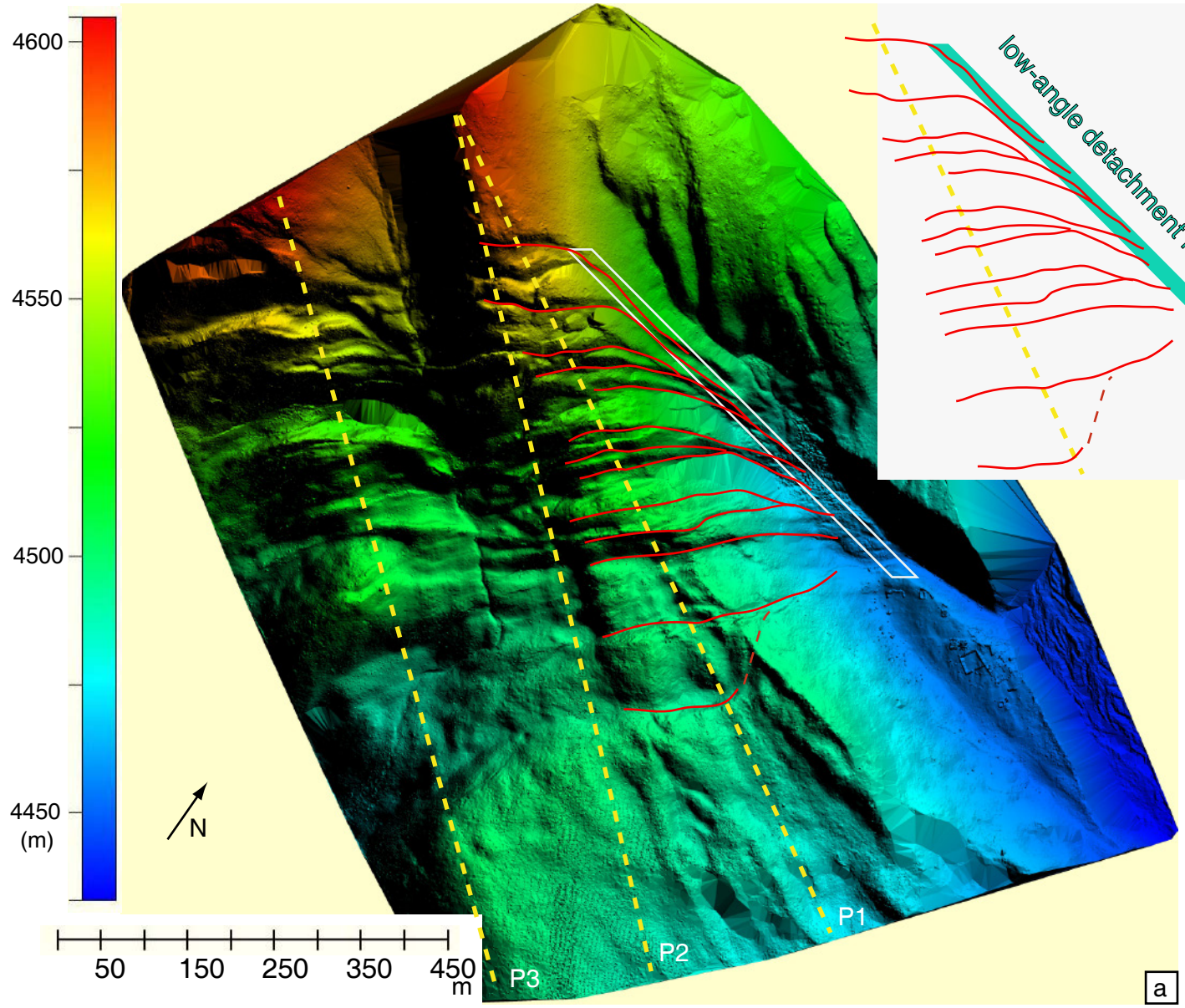
4600
4550
4500
4450
(m)
N
50
150
250
350
450
m
P1
P2
P3
low-angle detachment fault
a

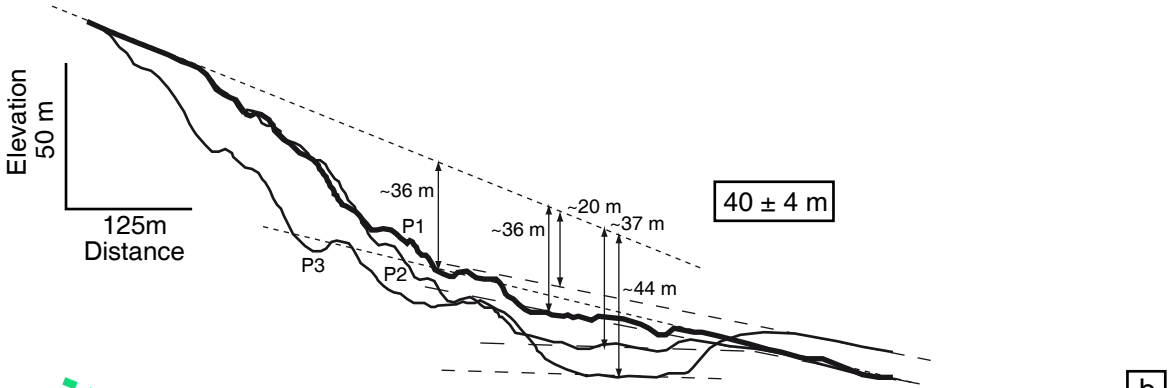
Elevation
50 m
125m
Distance
~36 m
P1
P3
P2
~36 m
~20 m
~37 m
~44 m
40 ± 4 m
b

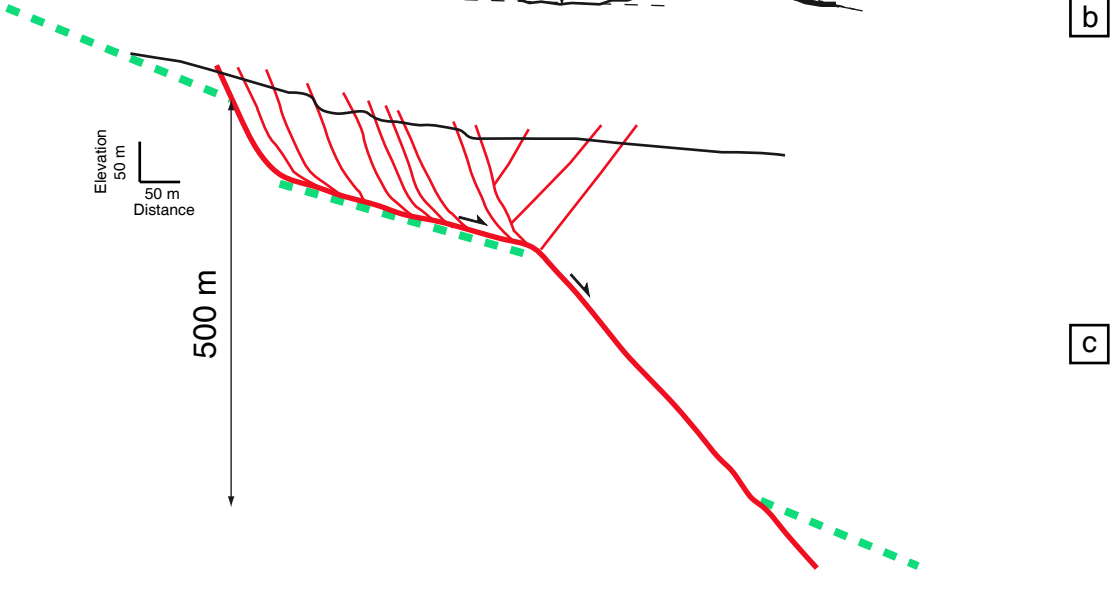
Elevation
50 m
50 m
Distance
500 m
c

Figure 7.

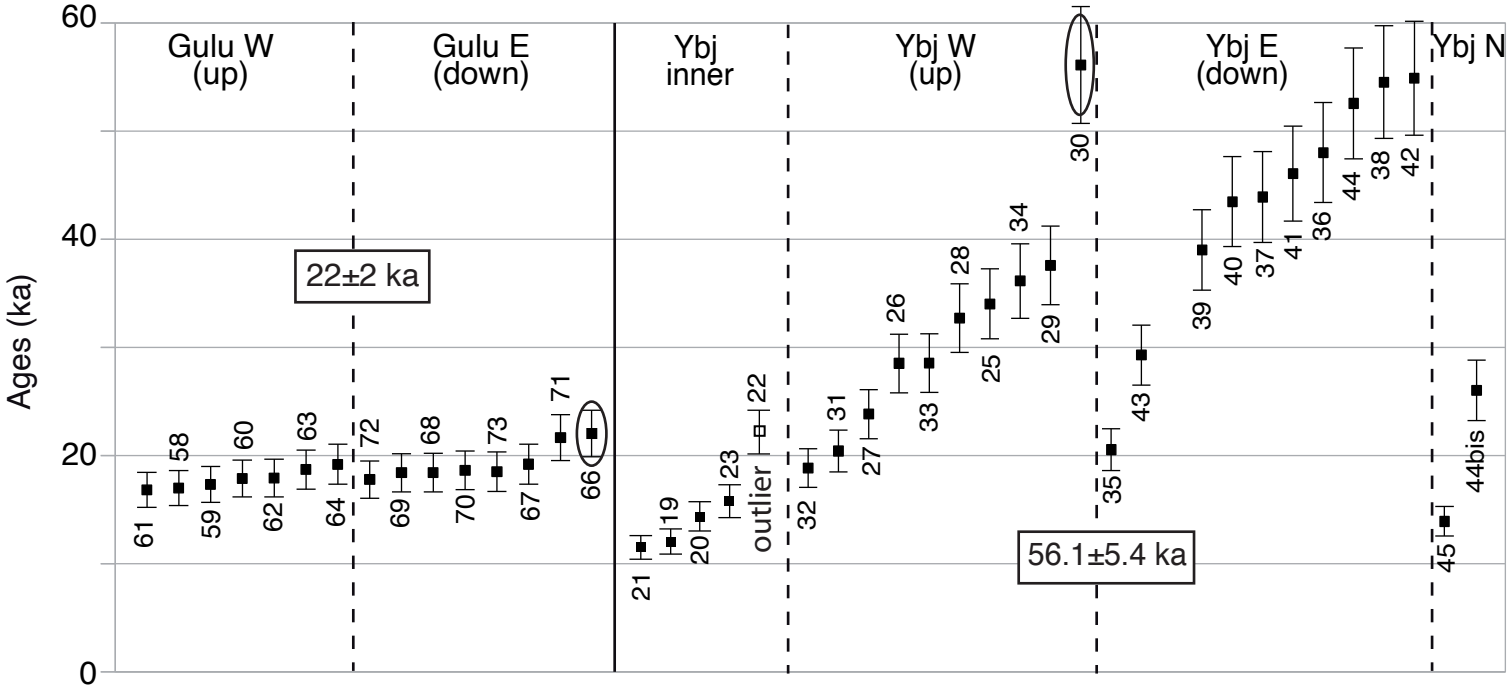
Ages (ka)
60
40
20
0
Gulu W (up)
Gulu E (down)
Ybj inner
Ybj W (up)
Ybj E (down)
Ybj N
22±2 ka
56.1±5.4 ka
61
58
59
60
62
63
64
72
69
68
70
73
67
71
66
21
19
20
23
outlier
22
32
31
27
26
33
28
25
34
29
30
35
43
39
40
37
41
36
44
38
42
45
44bis

Figure 8.

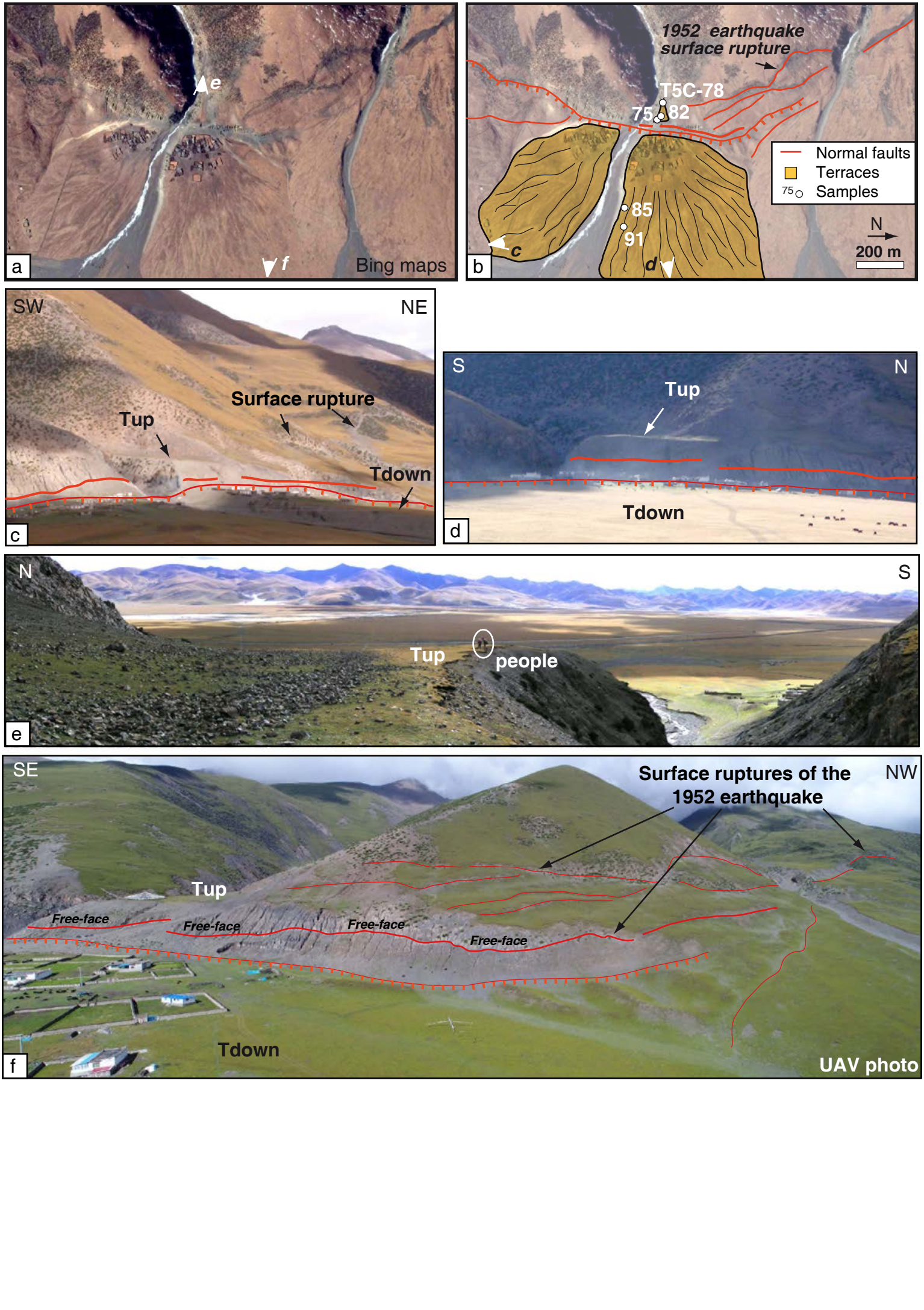
a
e
f
Bing maps
b
1952 earthquake
surface rupture
T5C-78
75
82
85
91
c
d
Normal faults
Terraces
75 Samples
N
200 m
SW
NE
Surface rupture
Tup
Tdown
c
S
N
Tup
Tdown
d
N
S
Tup
people
e
SE
NW
Surface ruptures of the
1952 earthquake
Tup
Free-face
Free-face
Free-face
Free-face
Tdown
f
UAV photo

Figure 9.

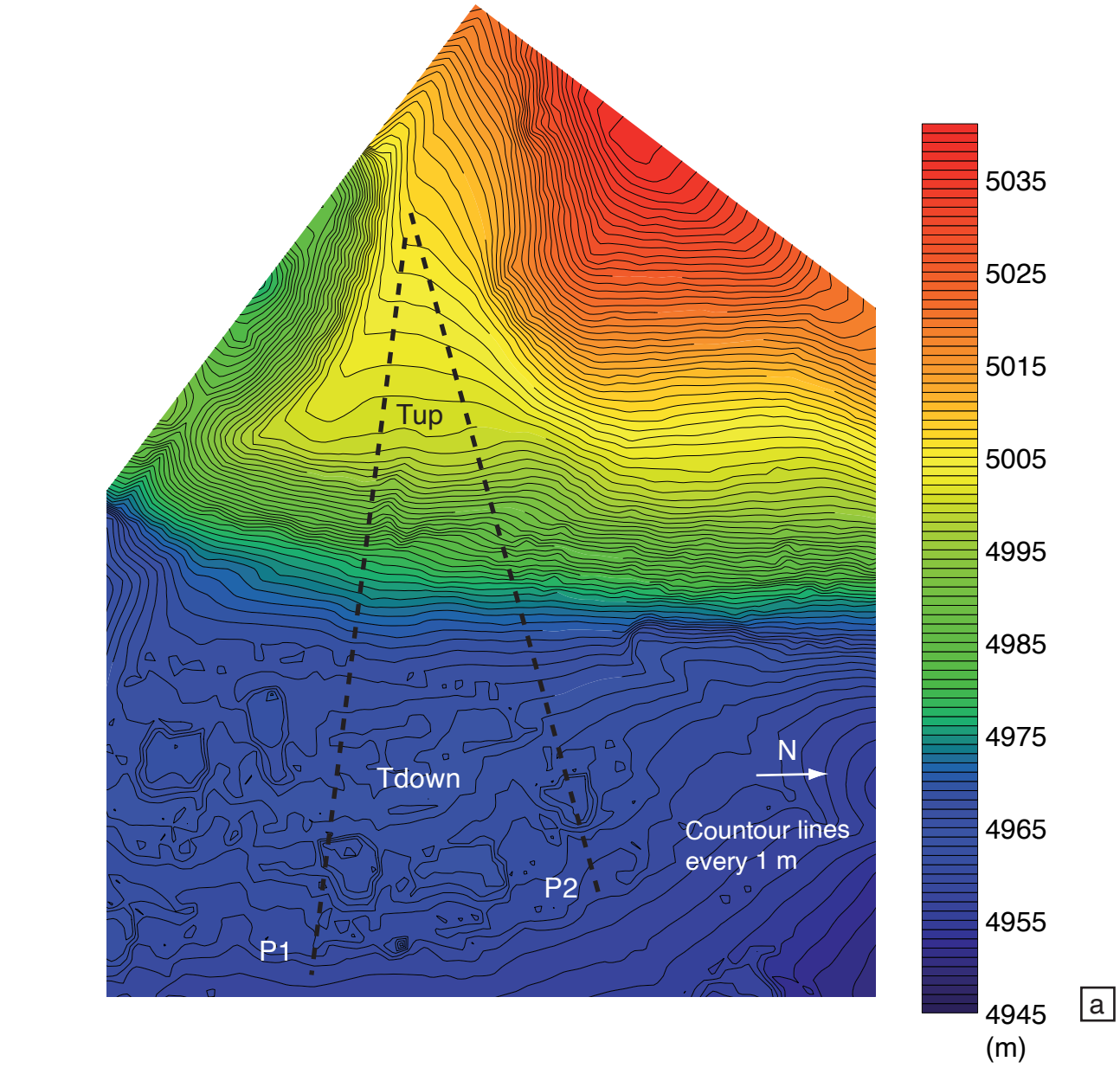
Tup
Tdown
P1
P2
N
Countour lines
every 1 m
5035
5025
5015
5005
4995
4985
4975
4965
4955
4945
(m)
a
Tup
25 ± 2 m
P1
27 m
23 m
P2
houses
Tdown
Elevation
20 m
50 m
Distance
b
60-70°
~5°
~5°
20 m
20 m
c

Figure 10.

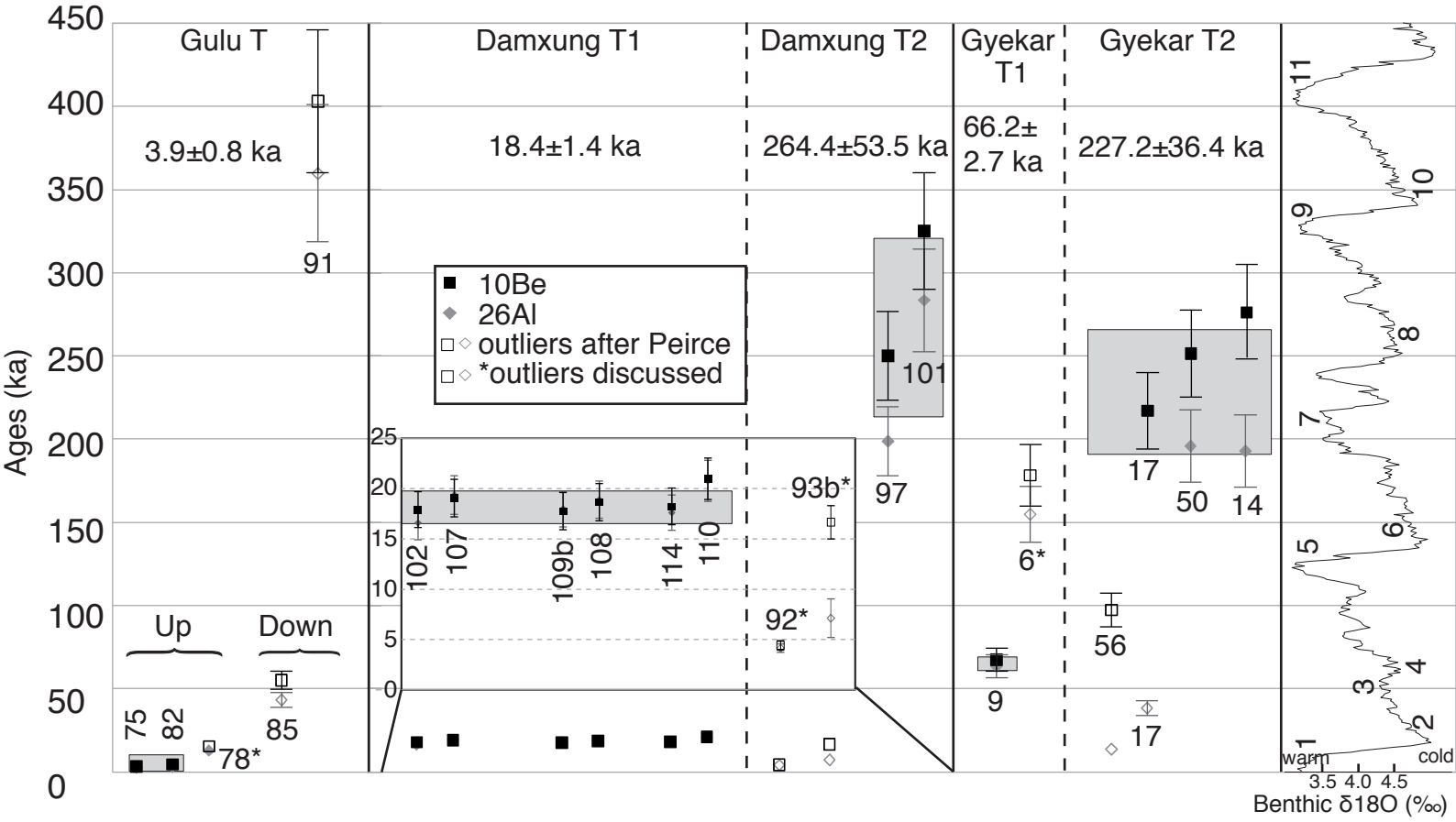
Gulu T
Damxung T1
Damxung T2
Gyekar T1
Gyekar T2
3.9±0.8 ka
18.4±1.4 ka
264.4±53.5 ka
66.2± 2.7 ka
227.2±36.4 ka
Ages (ka)
10Be
26Al
outliers after Peirce
*outliers discussed
Up
Down
75
82
78*
85
91
102
107
109b
108
114
110
93b*
92*
97
101
6*
9
56
17
17
50
14
warm
cold
3.5 4.0 4.5
Benthic δ18O (‰)

Figure 11.


a

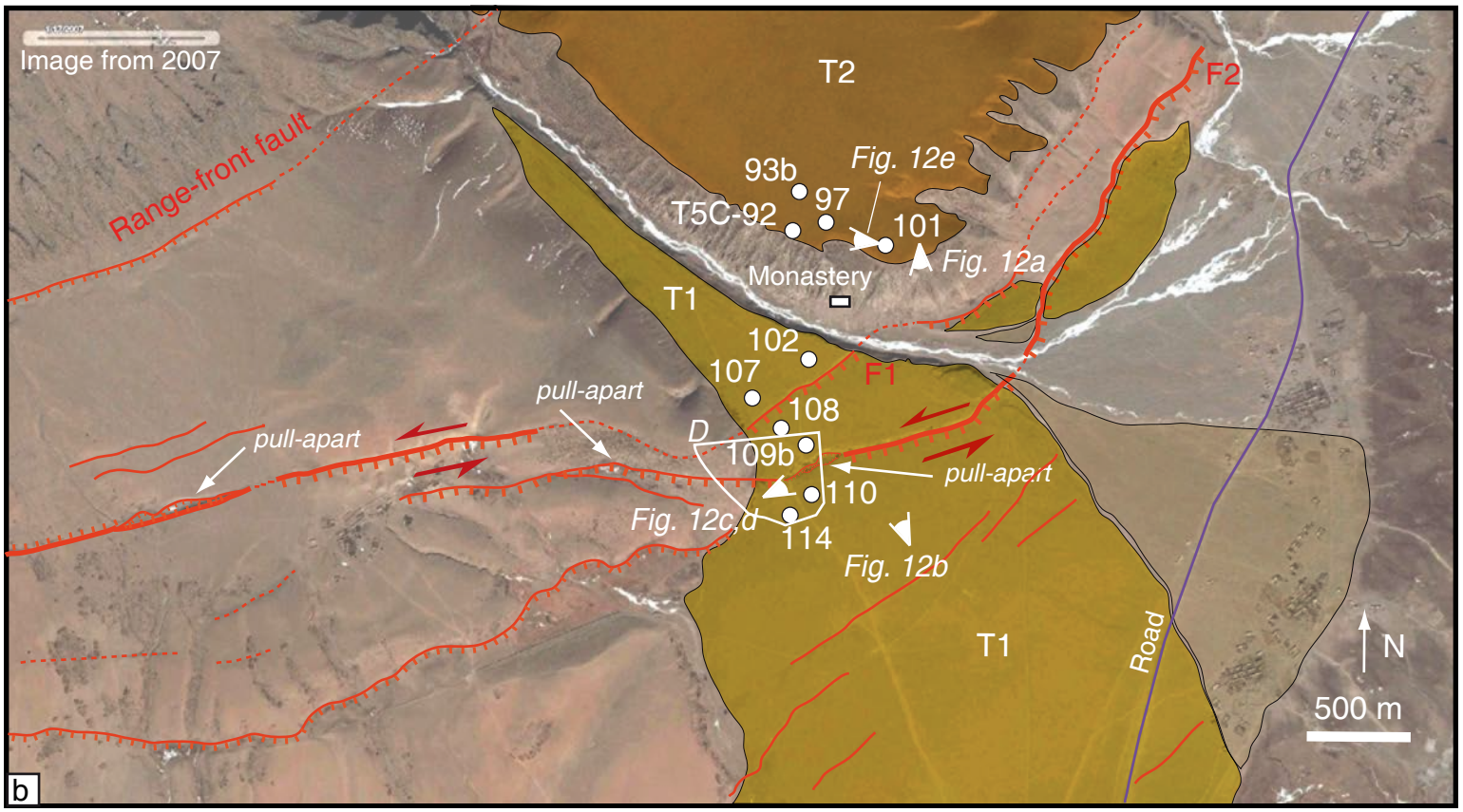
Image from 2007
T2
F2
Range-front fault
93b
Fig. 12e
97
T5C-92
101
Fig. 12a
Monastery
T1
102
107
F1
pull-apart
pull-apart
108
D
109b
pull-apart
110
Fig. 12c,d
114
Fig. 12b
T1
Road
N
500 m
b

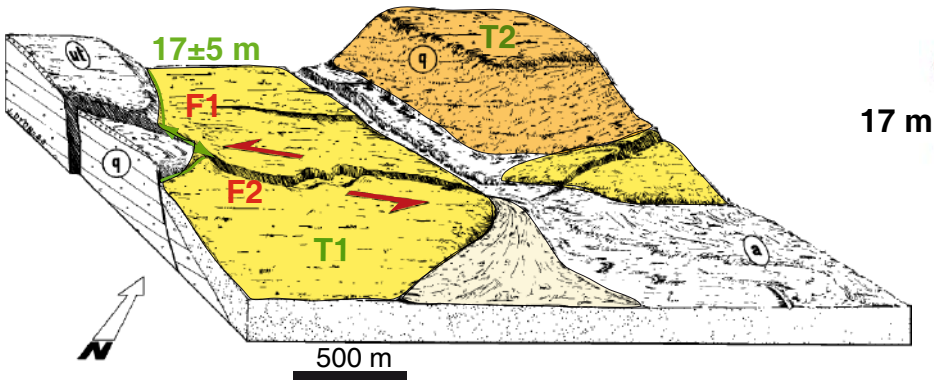
17±5 m
T2
F1
F2
T1
500 m
c

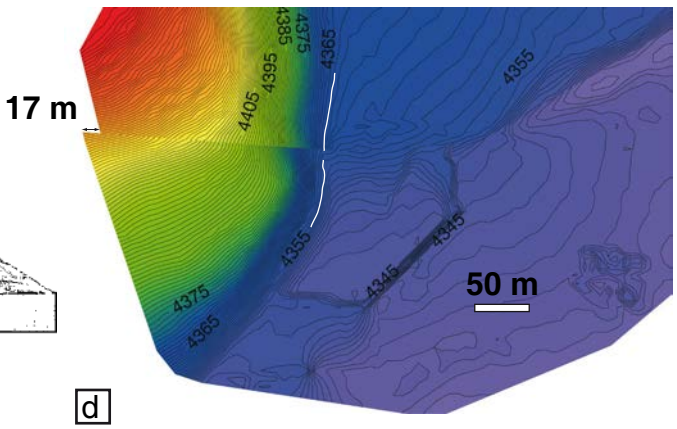
17 m
4385
4375
4365
4395
4405
4355
4345
50 m
d

Figure 12.

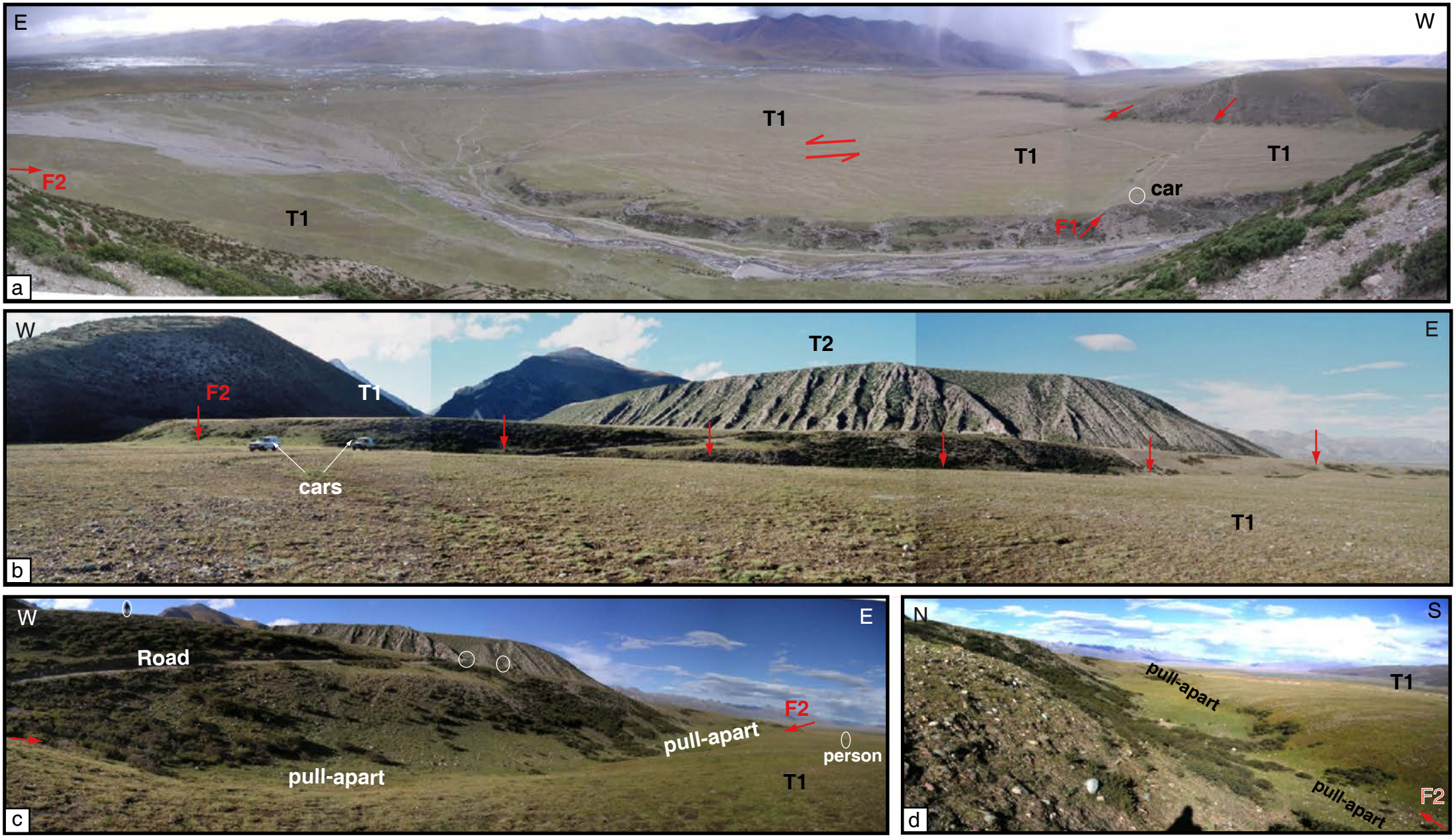
E
W
T1
T1
T1
F2
T1
car
F1
a
W
E
T2
F2
T1
cars
T1
b
W
E
Road
F2
pull-apart
person
pull-apart
T1
c
N
S
pull-apart
T1
pull-apart
F2
d

Figure 13.

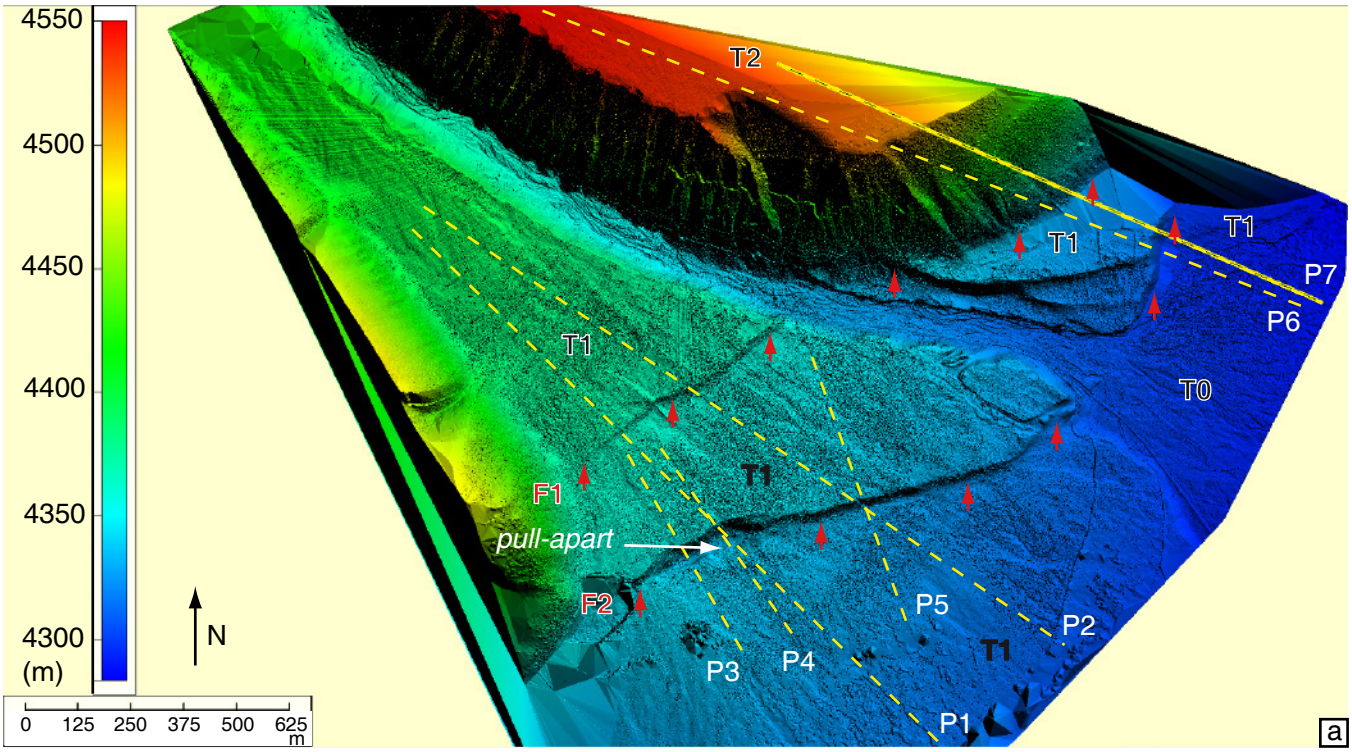
4550
4500
4450
4400
4350
4300
(m)
N
0 125 250 375 500 625 m
T2
T1
T1
T1
P7
P6
T0
T1
F1
T1
pull-apart
F2
P5
P2
T1
P3
P4
P1
a

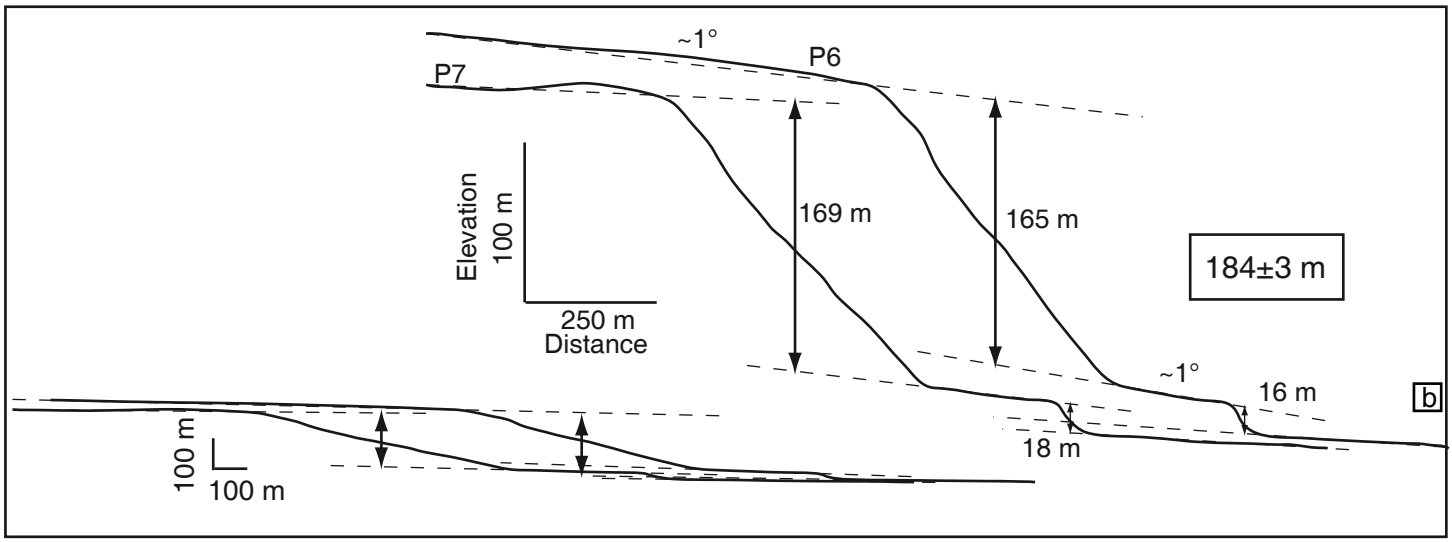
~1°
P6
P7
Elevation
100 m
250 m
Distance
169 m
165 m
184±3 m
~1°
16 m
18 m
100 m
100 m
b

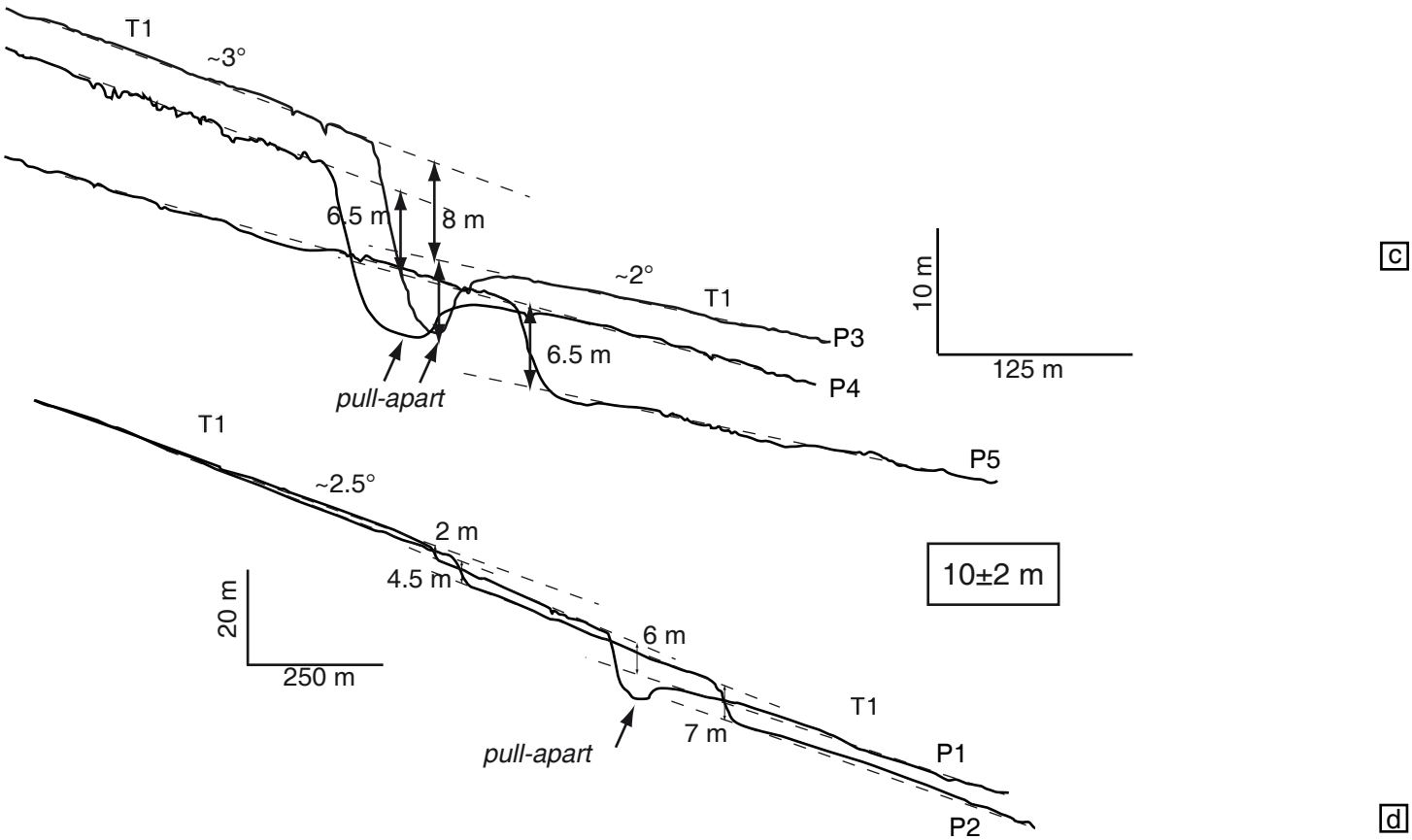
T1
~3°
6.5 m
8 m
~2°
T1
P3
6.5 m
P4
pull-apart
10 m
125 m
c
T1
P5
~2.5°
2 m
4.5 m
10±2 m
20 m
250 m
6 m
T1
7 m
pull-apart
P1
P2
d

Figure 14.

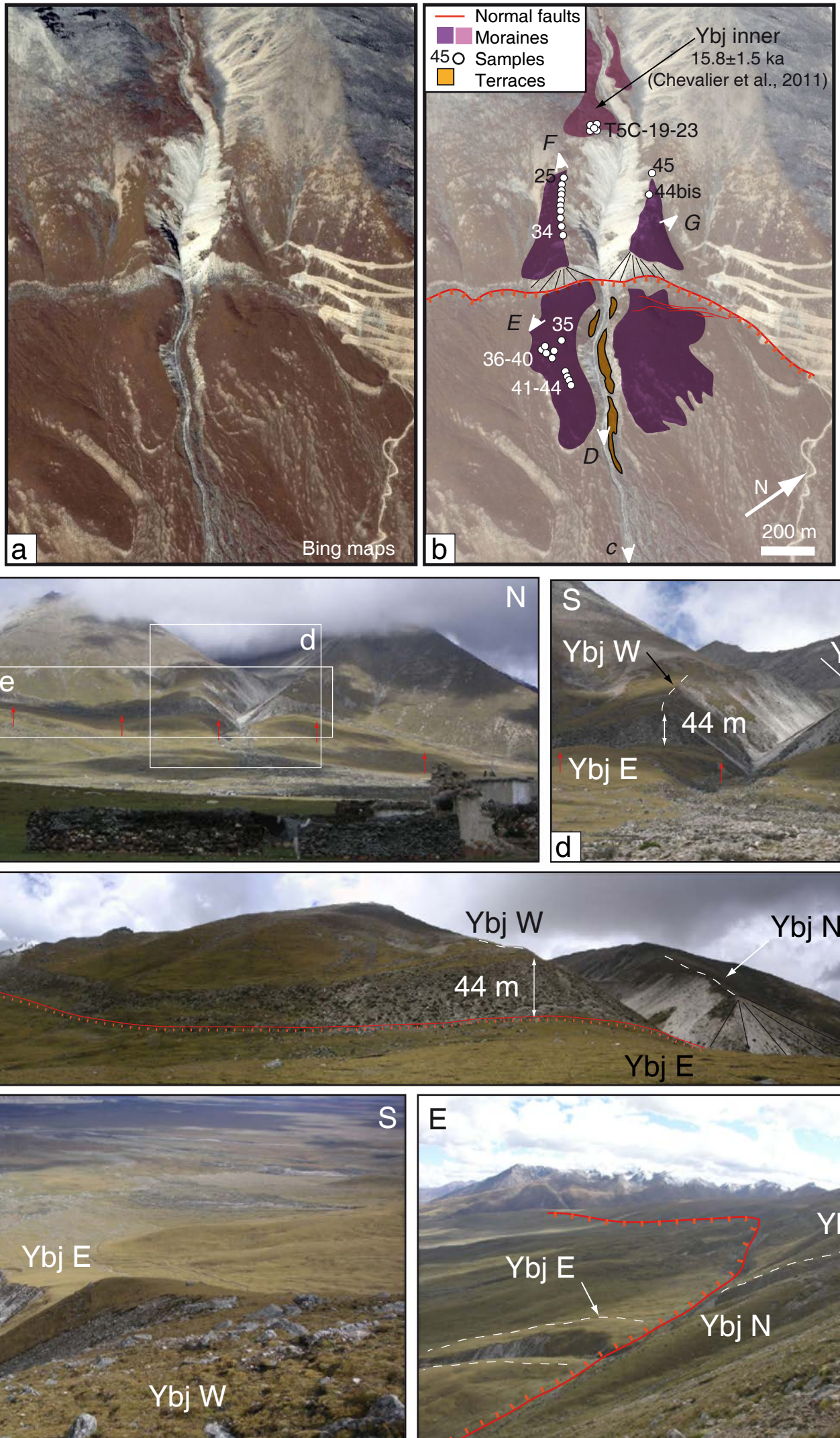
a
Bing maps
b
Normal faults
Moraines
45 Samples
Terraces
Ybj inner
15.8±1.5 ka
(Chevalier et al., 2011)
T5C-19-23
F
25
34
45
44bis
G
E
35
36-40
41-44
D
N
200 m
c
c
S
N
d
e
d
S
N
Ybj W
Ybj N
44 m
Ybj E
e
S
N
Ybj W
Ybj N
44 m
Ybj E
f
N
S
Ybj E
Ybj W
g
E
W
Ybj W
Ybj E
Ybj N

Figure 15.

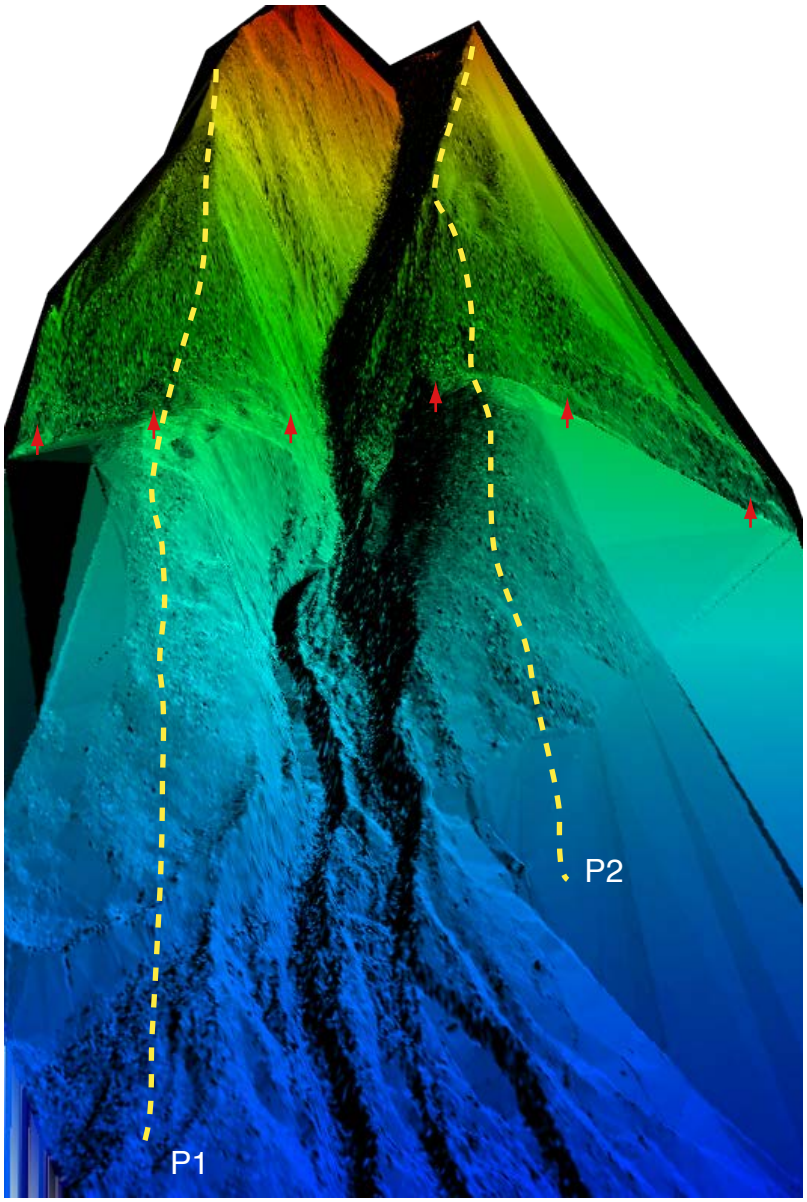
P2
P1

a

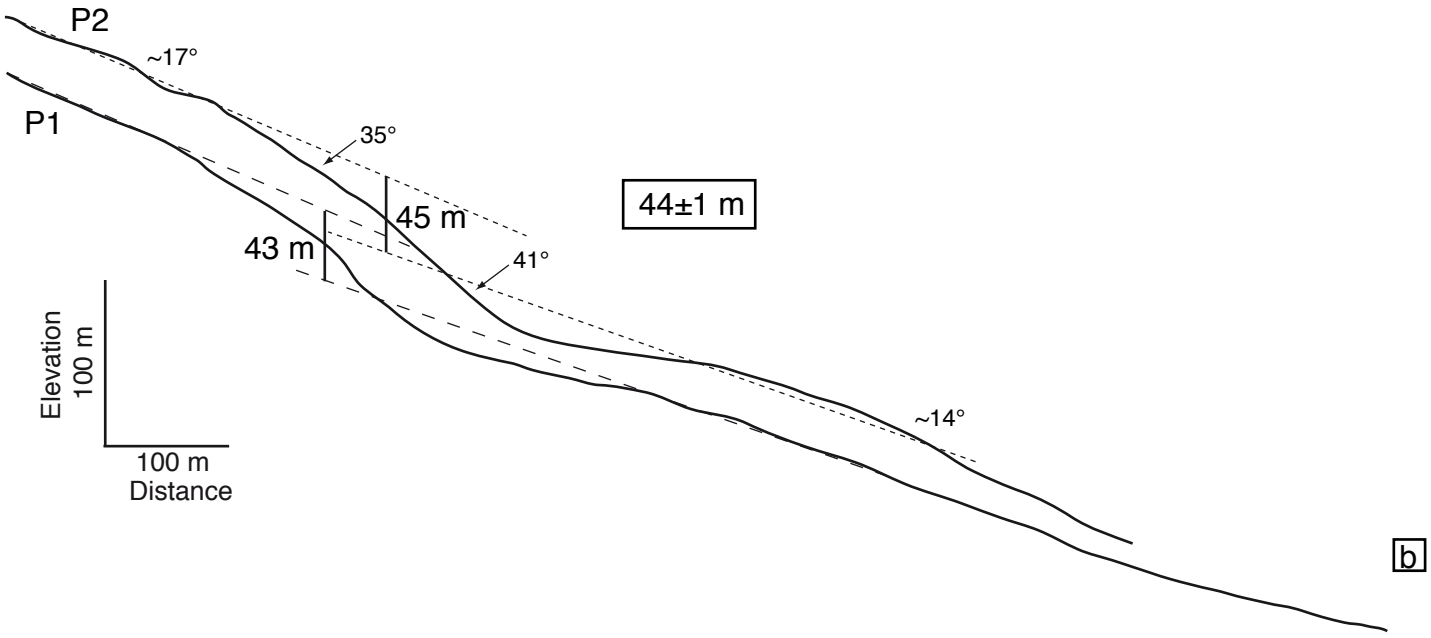
P2
~17°
P1
35°
45 m
44±1 m
43 m
41°
~14°
Elevation
100 m
100 m
Distance

b

Figure 16.

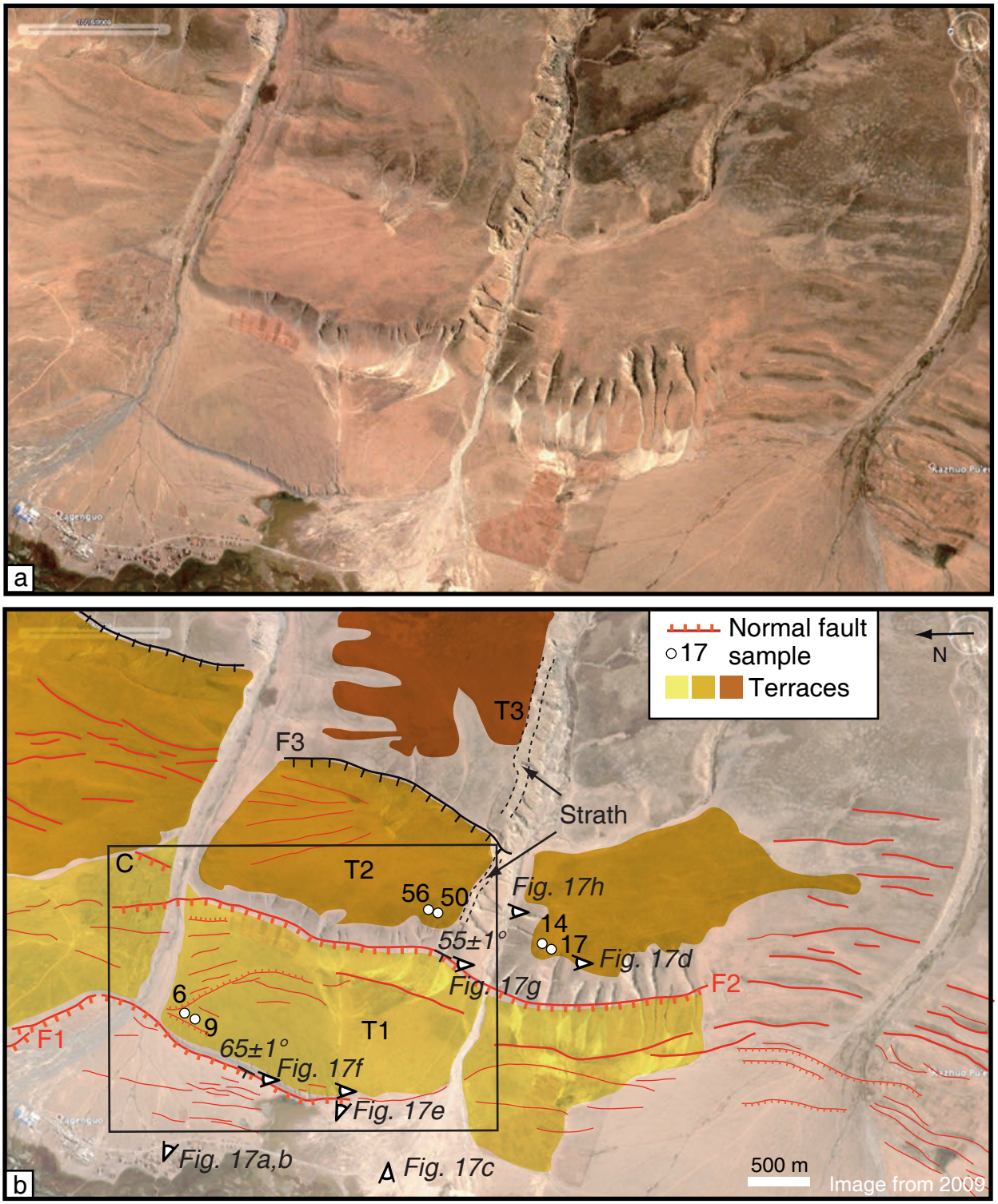
a
Normal fault
17 sample
Terraces
N
T3
F3
Strath
C
T2
56
50
Fig. 17h
14
17
Fig. 17d
55±1°
Fig. 17g
F2
6
9
T1
F1
65±1°
Fig. 17f
Fig. 17e
Fig. 17a,b
Fig. 17c
500 m
Image from 2009
b
T2
T1
no data
N
Countour lines
every 1 m
c
4510
4490
4470
4450
4430
4410
4390
4370
4350
(m)

Figure 17.

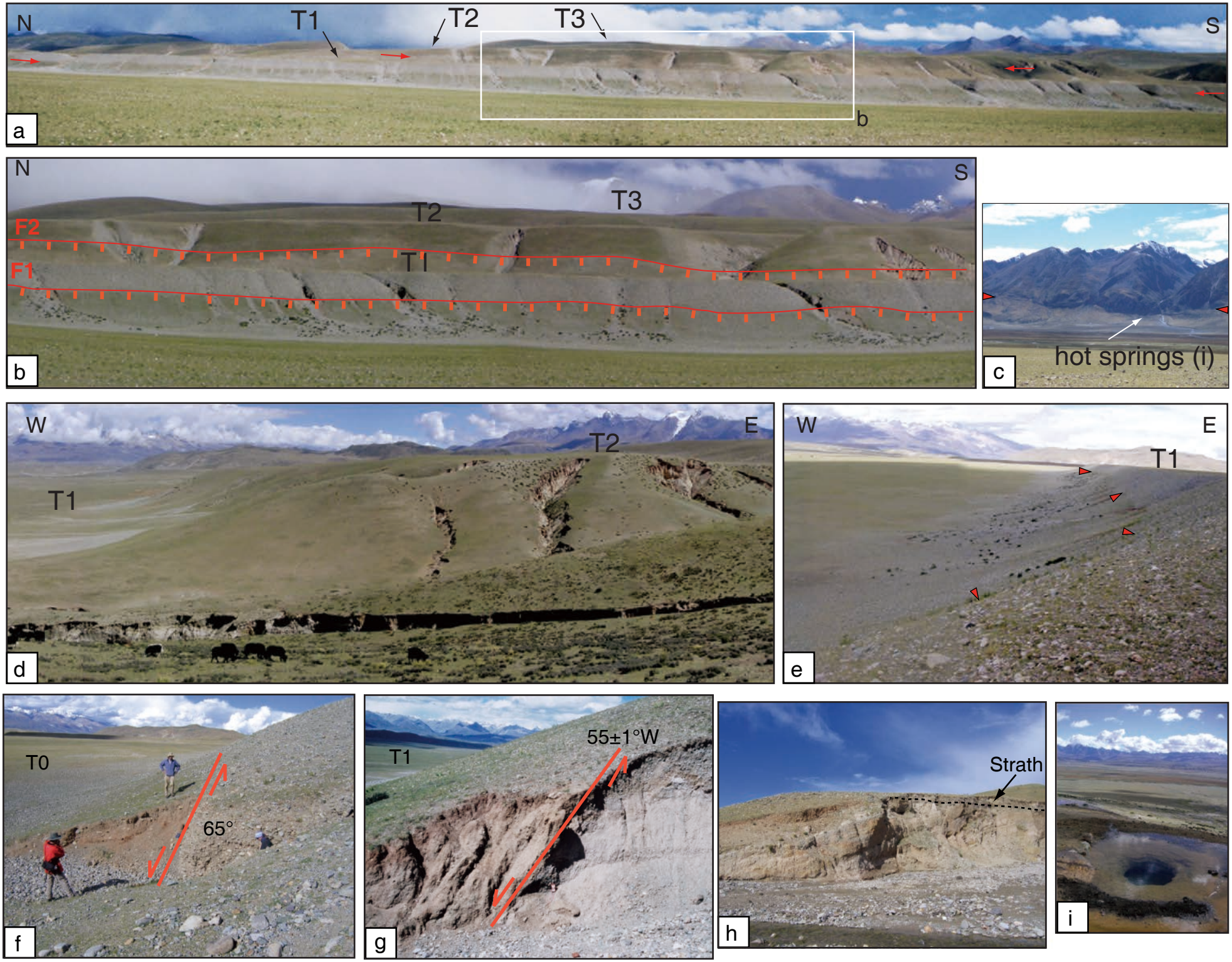
N
T1
T2
T3
S
a
b
N
S
T2
T3
F2
T1
F1
b
hot springs (i)
c
W
E
T2
T1
d
W
E
T1
e
T0
65°
f
T1
55±1°W
g
Strath
h
i

Figure 18.

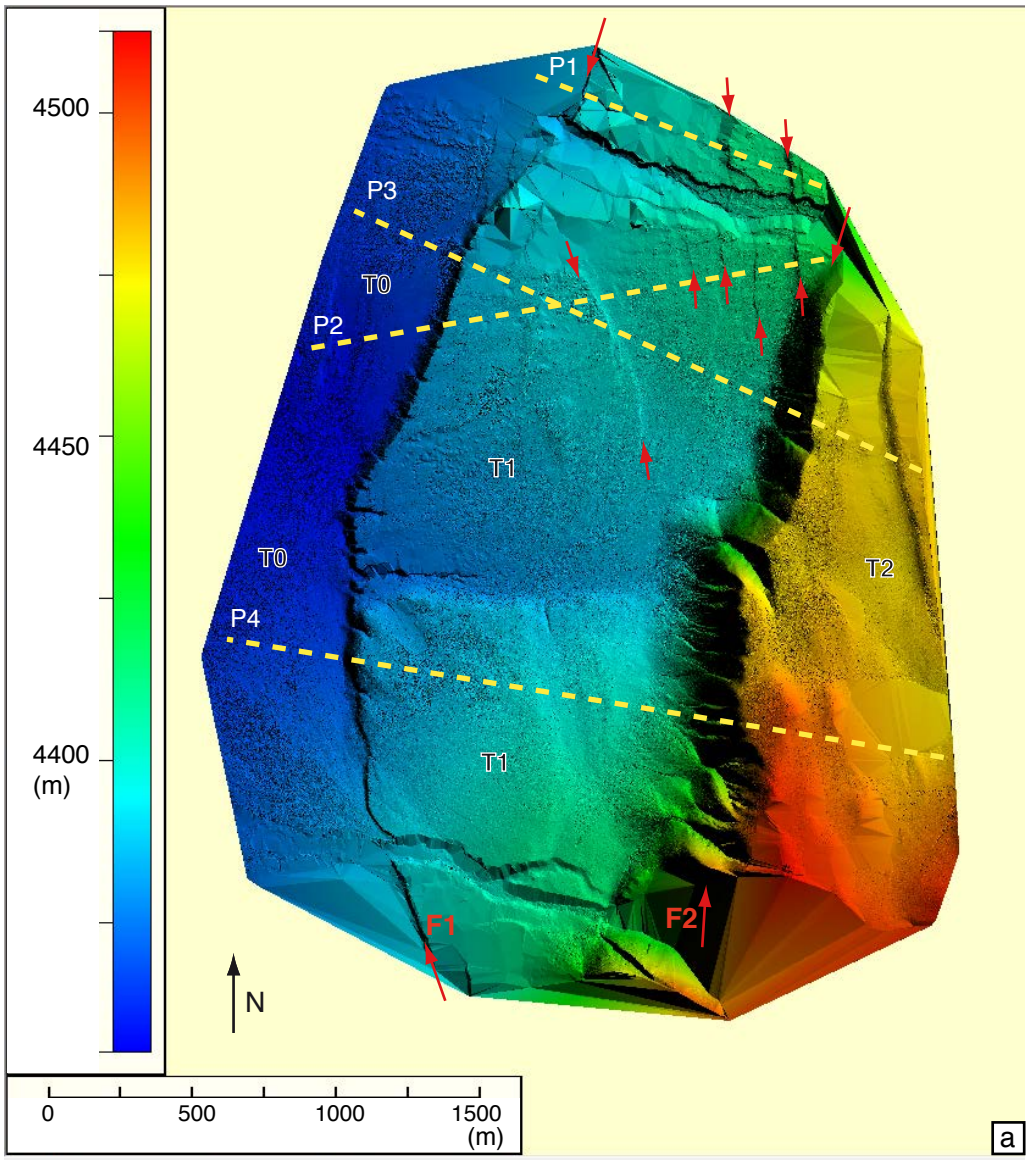
4500
4450
4400
(m)
P1
P3
T0
P2
T1
T0
T2
P4
T1
F1
F2
N
0
500
1000
1500
(m)
a

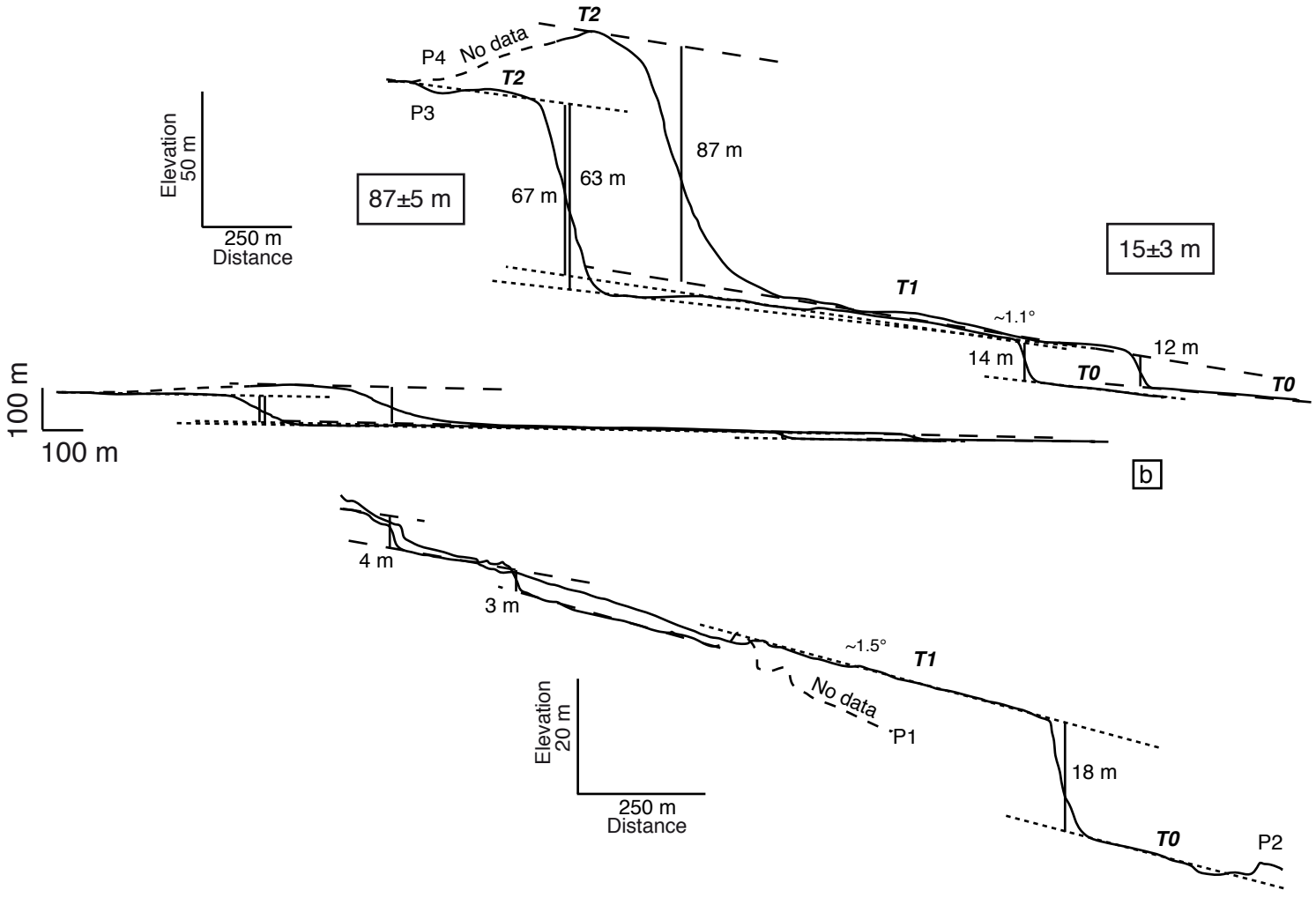
T2
P4
No data
T2
P3
Elevation
50 m
250 m
Distance
87±5 m
87 m
67 m
63 m
15±3 m
T1
~1.1°
14 m
12 m
T0
T0
100 m
100 m
b
4 m
3 m
~1.5°
T1
No data
P1
Elevation
20 m
250 m
Distance
18 m
T0
P2

Figure 19.

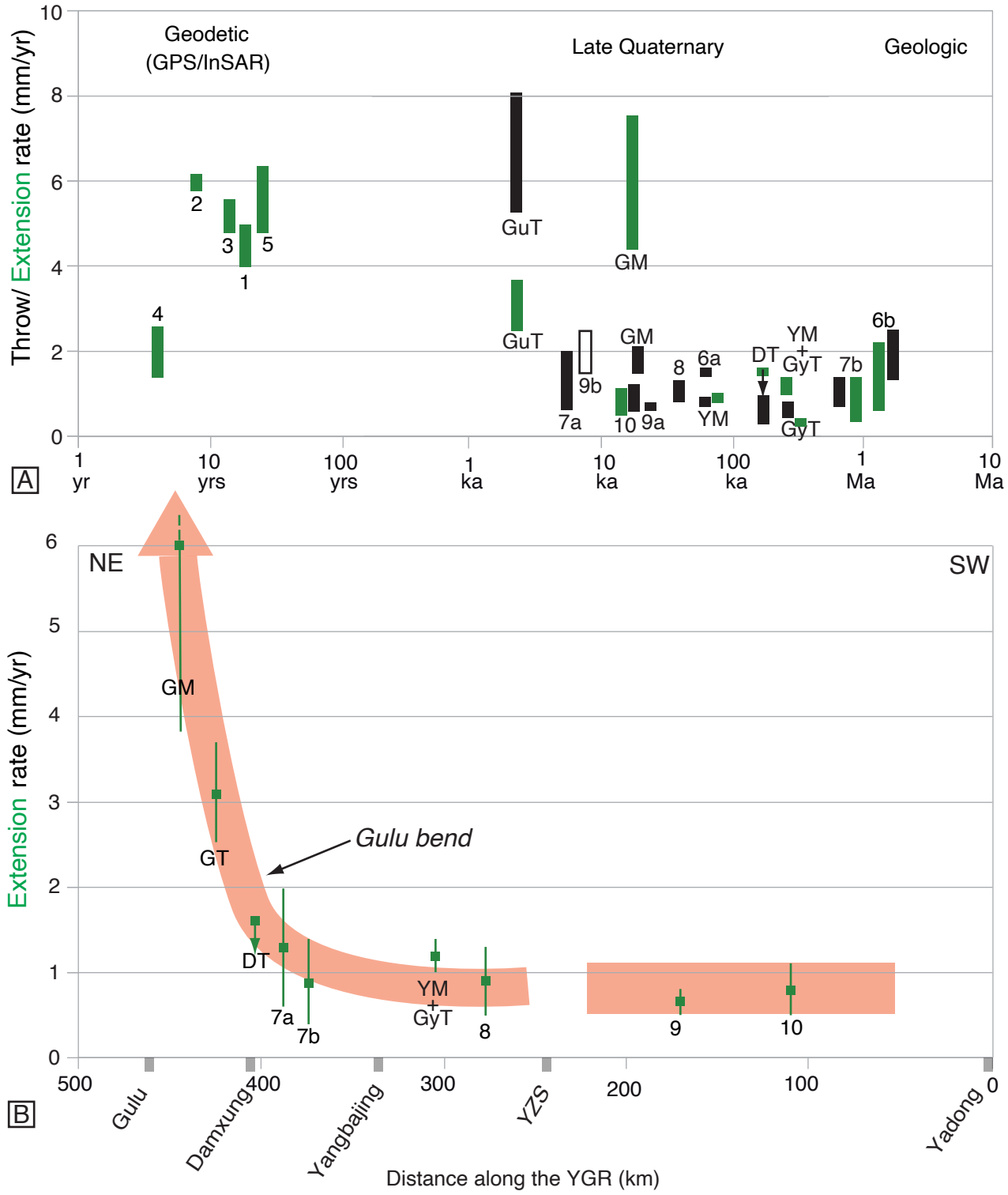
Geodetic
(GPS/InSAR)
Late Quaternary
Geologic
Throw/ Extension rate (mm/yr)
10
8
6
4
2
0
1
yr
10
yrs
100
yrs
1
ka
10
ka
100
ka
1
Ma
10
Ma
A
2
3
1
5
4
GuT
GuT
GM
GM
9b
7a
10
9a
8
6a
YM
DT
YM
+
GyT
GyT
7b
6b
NE
SW
Extension rate (mm/yr)
6
5
4
3
2
1
0
GM
GT
DT
7a
7b
Gulu bend
YM
+
GyT
8
9
10
500
400
300
200
100
0
B
Gulu
Damxung
Yangbajing
YZS
Yadong
Distance along the YGR (km)

Figure 20.

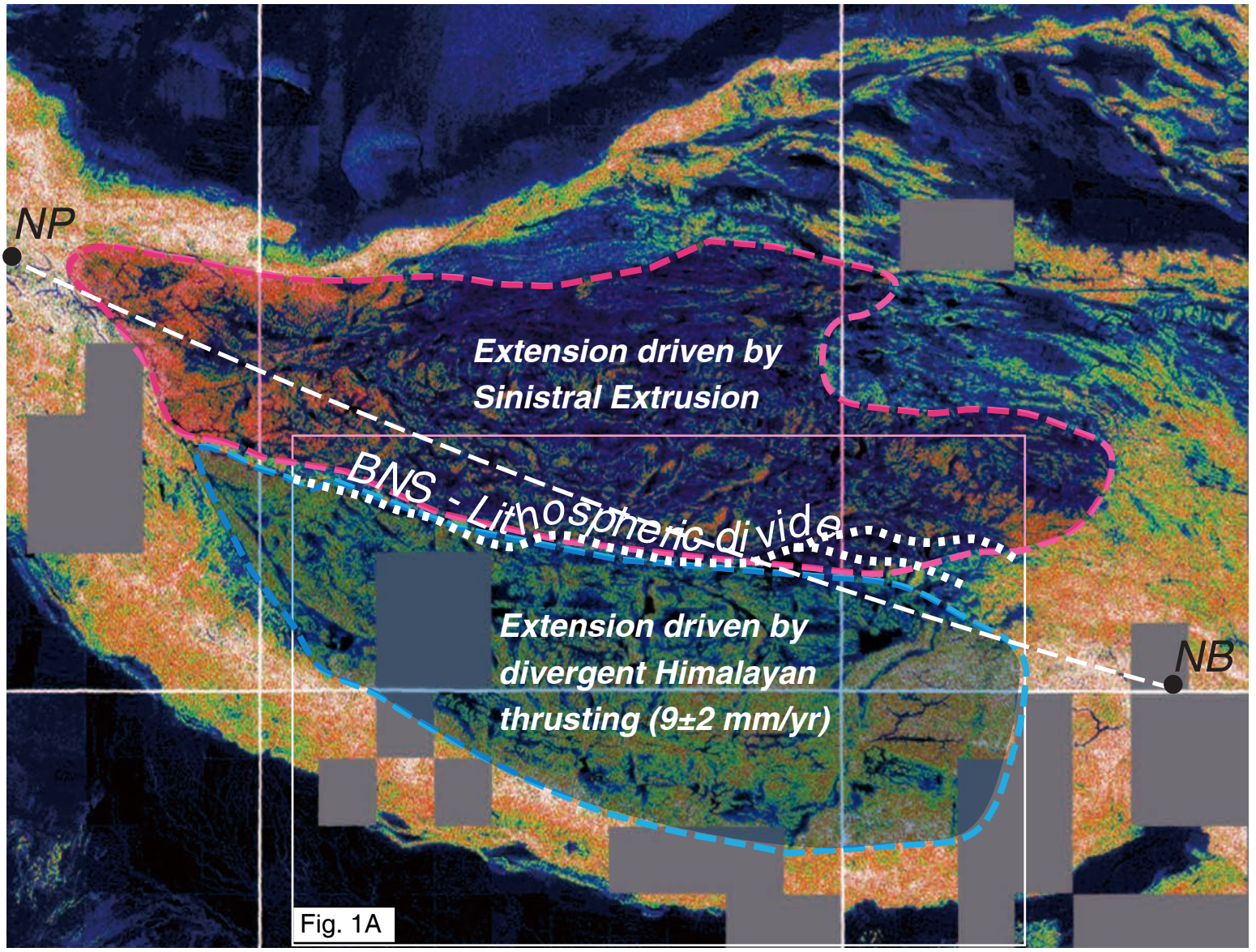
NP
Extension driven by
Sinistral Extrusion
BNS - Lithospheric divide
Extension driven by
divergent Himalayan
thrusting (9±2 mm/yr)
NB
Fig. 1A